INAUGURAL - DISSERTATION

zur
Erlangung der Doktorwürde
der
Naturwissenschaftlich-Mathematischen Gesamtfakultät
der
Ruprecht-Karls-Universität
Heidelberg

vorgelegt von
Diplom-Mathematiker Diplom-Physiker Dirk Hartmann
aus Brakel

Tag der mündlichen Prüfung: 6. November 2007

Multiscale Modelling, Analysis, and Simulation in Mechanobiology

Gutachter: Prof. Dr. Dr. h.c. mult. Willi Jäger

Prof. Dr. Marek Niezgódka

To Frauke, Clara, and Leander

Abstract

The main object of this thesis is the rigorous derivation of continuum models in mechanobiology via multiscale analysis. On the microscopic level, models in terms of energy functionals defined on networks / lattices are considered. Using concepts of Γ-convergence rigorous convergence results as well as explicit homogenisation formulae can be derived. Based on a characterisation via energy functionals, appropriate macroscopic stress-strain relationships (constitutive equations) are determined.

Mechanics of the membrane-bound cytoskeleton of red blood cells, and accordingly mechanics of red blood cells, are considered as one test case. The rigorous derivation of a macroscopic continuum model is based on a realistic discrete microscopic model. Simulations of optical tweezer experiments confirm the model qualitatively as well as quantitatively.

For these simulations an appropriate computational framework for single cell mechanics is developed using finite element methods. It accounts explicitly for membrane mechanics and its coupling with bulk mechanics. The approach is highly flexible and can be generalised to many other cell models, also including biochemical control.

As a test case considering the interactions between biological processes and mechanics, growing cell cultures are investigated. From a discrete cellular-automaton-like description macroscopic continuum models are derived. Furthermore, it is shown that the models can account for branching morphogenesis - a typical phenomenon observed in growing cell cultures, where growth is promoted by a diffusing substance.

Zusammenfassung

Das Thema der Doktorarbeit ist die rigorose Herleitung von kontinuierlichen Modellen in der Mechanobiologie durch Skalenübergänge. Auf mikroskopischer Ebene werden Modelle betrachtet, welche durch Energiefunktionale auf Netzwerken / Gittern gegeben sind. Die Konvergenz solcher mikroskopischen Energiefunktionale gegen kontinuierliche makroskopische Energiefunktionale kann im Sinne der Γ-Konvergenz gezeigt werden. Die kontinuierlichen Grenzfunktionale werden durch explizite Homogenisierungsformeln charakterisiert. Auf der Basis solcher expliziten Grenzfunktionale werden Stress-Verzerrungs-Relationen (konstitutive Gleichungen) hergeleitet.

Als ein Musterfall wird die Mechanik des membrangebundenen Zytoskeletts von roten Blutkörperchen bzw. die Mechanik der roten Blutkörperchen selbst betrachtet. Die rigorose Herleitung eines kontinuierlichen makroskopischen Modells basiert auf einem realistischen diskreten mikroskopischen Modell. Simulationen von Experimenten mit optischen Pinzetten bestätigen das hergeleitete Modell sowohl in qualitativer als auch in quantitativer Hinsicht.

Zu diesem Zweck wird ein entsprechendes numerisches Verfahren für Einzelzell-Mechanik mit Hilfe der Finite Elemente Methode entwickelt. Die Mechanik der Membran sowie deren Kopplung mit der Mechanik des Zellinneren wird bei diesem Ansatz explizit berücksichtigt. Die Simulationsumgebung ist sehr flexibel und kann für andere Zellmodelle erweitert werden, wobei eine gleichzeitige Berücksichtigung der Biochemie möglich ist.

Als ein Musterfall für die Interaktion zwischen biologischen Prozessen und Biomechanik werden wachsende Zellkulturen betrachtet. Auf der Basis eines diskreten Modells für einzelne Zellen werden kontinuierliche makroskopische Modelle hergeleitet. Weiterhin wird gezeigt, dass diese Modelle Verzweigungsstrukturen ausbilden können - ein typisches Phänomen in Zellkulturen, deren Wachstum durch eine diffundierende Substanz angeregt wird.

Contents

Chapter 1

Introduction

> *Cell and tissue, shell and bone, leaf and flower, are so many portions of matter, and it is in obedience to the laws of physics that their particles have been moved, moulded and conformed. They are no exceptions to the rule that* $\Theta\epsilon\grave{o}\varsigma\ \grave{a}\epsilon\grave{\iota}\ \gamma\epsilon\omega\mu\acute{\epsilon}\tau\rho\epsilon\iota$. *Their problems of form are in the first instance mathematical problems, their problems of growth are essentially physical problems, and the morphologist is, ipso facto, a student of physical science.*
> (D'Arcy Thompson, 1917)

Biological processes and their interactions with biomechanics belong to the most complicated systems studied in the natural sciences. The investigation of these issues has a long tradition dating back to the seminal book *On Growth and Form* by D'Arcy Thompson (1917). However, only recently major insights have been gained due to the fast development of experimental, mathematical, and computational methods. These advances have led to the new discipline mechanobiology (for a short review see Wang and Thampatty, 2006), merging mechanics and molecular biology.

The interactions between mechanics and biological processes play a central role on multiple levels, from the molecular all the way up to the tissue and organ level. Many studies have shown that mechanical load can affect diverse cellular functions, such as gene induction, protein synthesis, cell growth, cell death, and differentiation. Among major cellular components involved in the mechanotransduction mechanisms, i.e. in signal transductions converting mechanical stimuli into chemical signals, is the cytoskeleton (Wang and Thampatty, 2006), whose mechanical properties are investigated in this thesis. A variety of experimental techniques are available to probe mechanical properties of cells and their interactions with biological processes on different scales (Bao and Suresh, 2003), e.g. uni-axial stretching of cells bound to microplates shown in Fig. 1.1 (Beil et al., 2003).

From a mechanist's point of view, many biological soft tissues are well characterised by a continuum theory on a macroscopic level. Considering short time scales, the tissues are usually described by hyperelastic (or Green elastic) materials. These

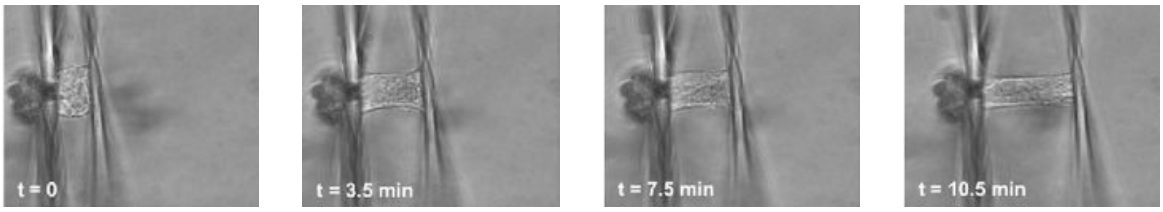

Fig. 1.1. Stretching of a Panc-1 cell chemically bound to the microplates in serum free medium. (courtesy to Joachim Spatz, University of Heidelberg)

are materials that respond elastically up to large strains and are typically given by stress-strain relationships that are derived from strain energy density functions. Such a description is only valid for short time scales. Investigating large time scales, viscoelastic effects (Forgacs et al., 1998) or even remodelling have to be taken into account. On a microscopic level, e.g. on the scale of the cytoskeleton of a cell, continuous descriptions are often not appropriate and discrete descriptions are preferable. At the same time, different physical concepts like entropic forces have to be considered. These are forces not determined by the underlying microscopic forces, e.g. atomic interactions on a lattice, but by the system's statistical tendency to increase its entropy. This complexity of biological materials often does not allow the use of standard continuum mechanics, but rather requires to *derive [new] basic equations [which] is even so much a mathematician's duty as to study their properties* (Trusdell, 1983).

The object of this thesis is the extension of multiscale techniques to biomechanical applications. These techniques allow the rigorous derivation of appropriate basic macroscopic models based on microscopic descriptions. In many examples from biomechanics, discrete models are an appropriate description on a microscale, e.g. for cells in a tissue or filaments in the cytoskeleton. Often microscopic descriptions in terms of energy functionals have been proposed, i.e. "functions" which relate a given state of a system to an energy. On the macroscopic level a continuum description is typically appropriate. Multiscale analysis, especially Γ-convergence, allows to close the gap between those two descriptions systematically: based on a microscopic description an explicit continuous macroscopic description can be rigorously derived in terms of energy functionals. From the latter, stress-strain relationships used in the framework of hyperelasticity can be calculated.

Typically continuum models are again discretised for computations raising the question why the derivation of these is necessary. Within a discrete description the discretisation of the system is naturally given. On the other hand, one is relatively free to choose a discretisation for continuum models. This allows relatively coarse discretisations speeding up simulations. The efficiency of computations for continuum models can be further increased by appropriate mesh refinement strategies. Another advantage of continuum models is that they are usually more accessible to mathematical analysis than discrete models.

In this thesis, we consider the mechanics of red blood cells and the mechanics of growing cell cultures illustrating the power of multiscale analysis in mechanobiology. The first test case is solely a mechanical problem, whereas the latter takes interactions between biological processes and mechanics into account. Using simulations (in the case of red blood cells) and analysis (in the case of growing cell cultures) the behaviour of the two examples is investigated. With respect to simulations the development of appropriate computational techniques for single cell mechanics is important, especially when having more intricate examples in mind. The setup of an appropriate computational framework for single cell mechanics within the finite element toolkit Gascoigne (Becker et al., 2007) is another pillar of this thesis.

The extension of mathematical multiscale techniques and the development of a highly flexible computational framework for single cell mechanics offers the possibility to tackle many unsolved questions in the field of mechanobiology in the near future. We believe that theses techniques will have a significant impact on modelling in mechanobiology, as underlined by the test cases considered in this thesis.

1.1 Outline of the thesis

The outline of the thesis (see also Fig. 1.2) is as follows: first, we present in Chapter 2 mathematical concepts of Γ-convergence and corresponding results connecting microscopic discrete descriptions with macroscopic continuous descriptions. In Chapter 3, we consider the mechanics of red blood cells as one test case. Here, the gap between a description on a subcellular scale and a description on a cellular scale is bridged. A major topic of this chapter is further the development of a highly flexible computational framework for single cell mechanics. As a test case considering the connection between a description on a cellular level and on a tissue level we investigate growing cell cultures in Chapter 4.

Readers not interested in mathematical details can skip Chapter 2 and start with the self-contained Chapters 3 or 4, discussing biological applications of multiscale analysis. For more details on the notation we refer to Appendix A. Readers who are unfamiliar with basic geometric analysis or the concept of entropic forces are referred to Appendix B, respectively Appendix C.

Chapter 2: Multiscale analysis

In this chapter, we outline the mathematical concepts of multiscale analysis. This chapter can be omitted without loss of continuity. We begin with a short outline of the discrete energy models which are considered in this thesis. In Section 2.2, we repeat the concept of Γ-convergence and its main features for the convenience of the reader. A theorem stating the convergence of discrete energy functionals to

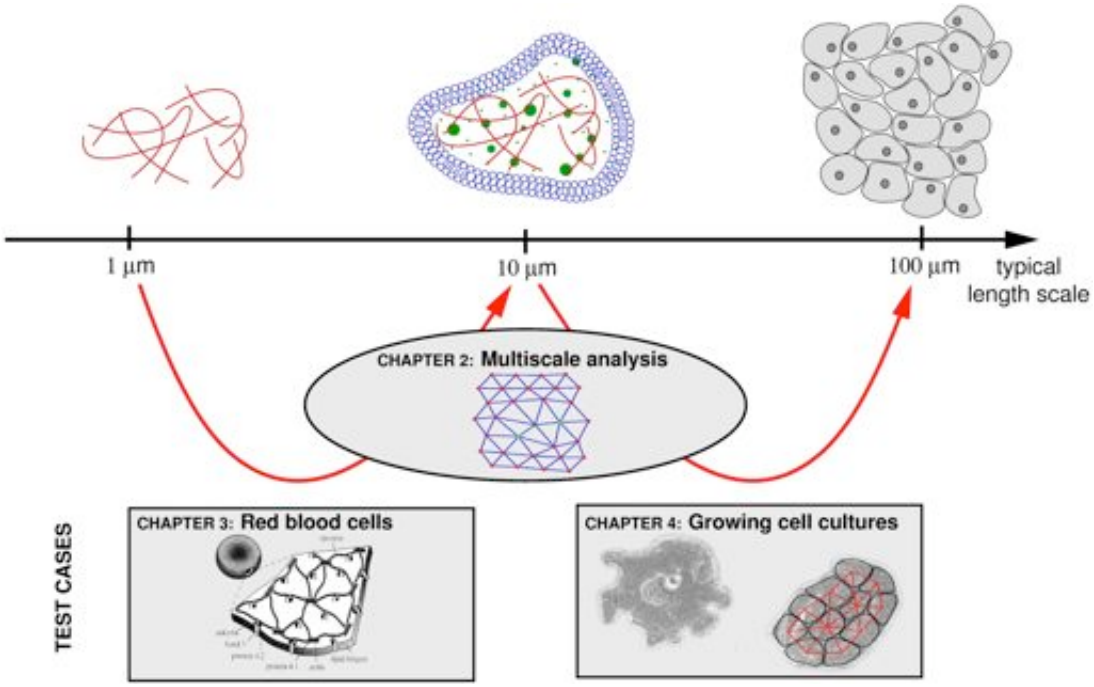

Fig. 1.2. Outline of the thesis: using multiscale analysis "gaps" between models on different spatial scales can be closed systematically.

continuous ones is presented in Section 2.3. The limit can be characterised by an auxiliary minimisation problem, which can be reduced to an explicit homogenisation formula. The approach presented in Section 2.3 is based on the ideas of Alicandro and Cicalese (2004), which are generalised to the more complex interactions considered in this thesis. In Section 2.4, connections to standard elasticity in the framework of hyperelasticity are discussed, and Section 2.5 deals with aspects of evolving networks.

Chapter 3: Red blood cells

This self-contained chapter considers mechanics of red blood cells, one of the most simple cells. Here, we restrict ourselves solely to mechanics and neglect any interactions with biological processes. Components involved in the mechanics of red blood cells are the cytosol, the lipid bilayer, as well as the membrane-bound cytoskeleton. Main biological facts are summarised in Section 3.1. In Section 3.2, we derive in terms of energy functionals a continuum description of the cytoskeleton, which is a discrete quasi-two-dimensional structure (Boey et al., 1998; Discher et al., 1998). Based on the continuum description of the cytoskeleton and the lipid bilayer via energy functionals, an appropriate description within the standard equations of continuum mechanics (balance of momentum and mass) is given using a variational approach. This is, to our knowledge, the first rigorous multiscale approach treating mechanics of red blood cells.

Red blood cells serve not only as a test case for the multiscale analysis, but also as a test case for the development of a highly flexible finite element framework for single cell mechanics. A main difficulty is the coupling of mechanics on hypersurfaces with bulk mechanics, as well as the treatment of the lipid bilayer. We do not rely on any special assumptions on the underlying equations, as required e.g. by boundary element methods typically being the method of choice (e.g. Pozrikidis, 2003a). Our approach is outlined in Section 3.3 and simulations of optical tweezer experiments with red blood cells are presented. The simulations agree quite well with experimental results, both qualitatively and quantitatively. This underlines the usefulness of multiscale analysis in biomechanics.

Chapter 4: Growing cell cultures

Here, we consider growing cell cultures as a test case for the derivation of macroscopic models based on discrete descriptions where interactions between biological processes and biomechanics play a role. In particular, we pay attention to branching morphogenesis, a typical phenomenon in developmental biology. The relevant biological background is reviewed in Section 4.1. Cell cultures can be described quite well by viscoelastic laws (Forgacs et al., 1998). Considering growing cell cultures, a difficulty is to choose the right deformation measure for such a description, since growth induces deformations which do not lead to stress. At the same time remodelling might take place, i.e. an evolution of the stress-strain relationships, complicating the derivation of appropriate mechanical laws.

Using the techniques of chapter 2, we present in Section 4.2 an appropriate model in terms of a solely elastic description. In the case of isotropic growth it coincides with the so-called notion of multiple natural configurations (Lubarda, 2004). Considering anisotropic growth, the ansatz yields some information on the evolution of the stress tensor in the elastic regime. The model is then generalised to a viscoelastic model as well as to the corresponding "viscous" model in the limit of fast stress relaxation. Because stress relaxation is typically faster than growth, the latter is an appropriate model for growing soft tissues on large time scales. In Section 4.3, we show its capability to reproduce branching morphogenesis via a linear stability analysis. The qualitative properties of the model agree well with a simpler, but less realistic model successfully applied as an explanation of branching morphogenesis (Hartmann and Miura, 2007, 2006).

The example of culture growth shows the explanatory power of the multiscale approach also in the case of interactions between mechanics and biological processes, which typically implies an evolution of the underlying discrete models / networks.

Chapter 2

Multiscale analysis

Biomechanical systems can be typically characterised by energy functionals. Often a discrete microscopic energy functional is an appropriate description. In this chapter, we investigate the existence and characterisation of corresponding continuous macroscopic energy functionals in the limit of small network length scales. The type of microscopic models considered in this thesis are introduced in Section 2.1.

Because we are generally interested in deformations with minimal energies, Γ-convergence (a variational convergence) is an appropriate framework (Braides, 2002), which is repeated in Section 2.2 for the convenience of the reader. Using the concepts of Alicandro and Cicalese (2004), Γ-convergence of the discrete energy functionals to continuous energy functionals is shown rigorously in Section 2.3. It is further proven that the continuous limit functionals can be characterised by auxiliary minimisation problems. Under the assumption of convexity, the homogenisation formulae can be reduced to "cell" formulae, which can be explicitly calculated.

With respect to mathematical analysis, we restrict ourselves to energy minimisation problems. Nevertheless, a connection to dynamics is possible. In this case the energy functionals serve as constitutive relations (Section 2.4).

2.1 Microscopic model

In this thesis, we would like to investigate appropriate macroscopic mechanical models of polymer networks (Chapter 3) and cell cultures (Chapter 4) as two examples of biomechanical systems (Fig. 2.1a-b). For simplicity, we restrict ourselves to the two-dimensional situation. Let us first outline the basic microscopic geometry and then introduce the type of energies which are considered in this chapter.

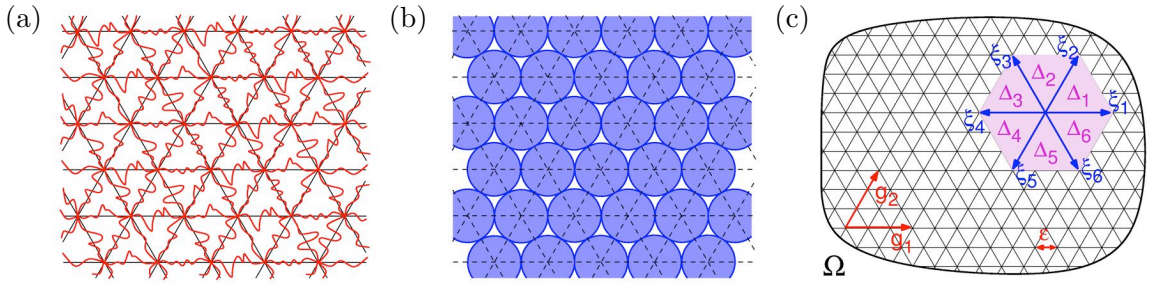

Fig. 2.1. (a) A polymer network as found in red blood cells (see Chapter 3); (b) Interacting cells in a culture (see Chapter 4); (c) Abstraction of the network considered in the two situations.

2.1.1 Microscopic geometry

All applications considered in this thesis have a hexagonal symmetry. Therefore, let us introduce the hexagonal lattice / network

$$\mathcal{G} = \{\boldsymbol{X} \in \mathbb{R}^2 : \boldsymbol{X} = \mu_1 \boldsymbol{g}_1 + \mu_2 \boldsymbol{g}_2 \text{ with } \mu_i \in \mathbb{Z}\}$$

with $\boldsymbol{g}_1 = (1, 0)$, $\boldsymbol{g}_2 = (1/2, \sqrt{3/4})$, such that a typical discrete reference configuration (see Fig. 2.1c) is given by

$$\varepsilon\mathcal{G} \cap \Omega$$

with $\Omega \subset \mathbb{R}^2$ bounded. Here, ε is the typical length scale of the network. The basic units of the hexagonal network are the links

$$\mathcal{G}^{\boldsymbol{\xi}} = \{\boldsymbol{\xi}_1 = \boldsymbol{g}_1, \boldsymbol{\xi}_2 = \boldsymbol{g}_2, \boldsymbol{\xi}_3 = \boldsymbol{g}_2 - \boldsymbol{g}_1, \boldsymbol{\xi}_4 = -\boldsymbol{\xi}_1, \boldsymbol{\xi}_5 = -\boldsymbol{\xi}_2, \boldsymbol{\xi}_6 = -\boldsymbol{\xi}_3\}$$

and triangles

$$\begin{aligned}\mathcal{G}^{\triangle} = \{&\triangle_1 = \lhd(\boldsymbol{\xi}_1, \boldsymbol{\xi}_2), \triangle_2 = \lhd(\boldsymbol{\xi}_2, \boldsymbol{\xi}_3), \triangle_3 = \lhd(\boldsymbol{\xi}_3, \boldsymbol{\xi}_4),\\ &\triangle_4 = \lhd(\boldsymbol{\xi}_4, \boldsymbol{\xi}_5), \triangle_5 = \lhd(\boldsymbol{\xi}_5, \boldsymbol{\xi}_6), \triangle_6 = \lhd(\boldsymbol{\xi}_6, \boldsymbol{\xi}_1) \text{ with } \boldsymbol{\xi}_i \in \mathcal{G}^{\boldsymbol{\xi}}\},\end{aligned}$$

where $\lhd(\boldsymbol{\xi}_i, \boldsymbol{\xi}_{i+1})$ is the triangle spanned by the vectors $\boldsymbol{\xi}_i, \boldsymbol{\xi}_{i+1} \in \mathcal{G}^{\boldsymbol{\xi}}$.

Let $\boldsymbol{X} \in \varepsilon\mathcal{G} \cap \Omega$ be the position of a network vertex in the reference configuration. Its motion / deformation is given by the function

$$\boldsymbol{x} = \boldsymbol{\chi} : \varepsilon\mathcal{G} \cap \Omega \ni \boldsymbol{X} \mapsto \boldsymbol{\chi}(\boldsymbol{X}) \in \mathbb{R}^2. \tag{2.1}$$

Since we are interested in mechanics, we will restrict us to deformations preserving the orientation. Additionally, let us introduce the finite difference quotient along any direction $\boldsymbol{\xi}$

$$D_{\varepsilon}^{\boldsymbol{\xi}}\boldsymbol{\chi}(\boldsymbol{X}) = \frac{\boldsymbol{\chi}(\boldsymbol{X} + \varepsilon\boldsymbol{\xi}) - \boldsymbol{\chi}(\boldsymbol{X})}{\varepsilon|\boldsymbol{\xi}|},$$

where we will typically consider $|\boldsymbol{\xi}| = 1$ (e.g. $\boldsymbol{\xi} \in \mathcal{G}^{\boldsymbol{\xi}}$), and the discrete "Jacobian"

$$\mathcal{A}_\varepsilon^\triangle \boldsymbol{\chi}(\boldsymbol{X}) = \frac{\det\left(D_\varepsilon^{\boldsymbol{\xi}_i}\boldsymbol{\chi}(\boldsymbol{X}) \otimes D_\varepsilon^{\boldsymbol{\xi}_{i+1}}\boldsymbol{\chi}(\boldsymbol{X})\right)}{\sqrt{3}/2}.$$

The discrete Jacobian is given as the deformed area of the unit equilateral triangle, spanned by the vectors $\boldsymbol{\xi_i}$ and $\boldsymbol{\xi}_{i+1}$, divided by its undeformed / initial area $\sqrt{3}/4$. In terms of the Jacobian, the orientation preserving condition of the deformations is nothing but its positivity.

2.1.2 Microscopic energies

Mechanical interactions on the network will be characterised by microscopic energy functionals. To be more precise: given an open set $\Omega \subset \mathbb{R}^2$ and $\varepsilon > 0$, we consider microscopic energies defined on functions $\boldsymbol{\chi}_\varepsilon : \varepsilon\mathcal{G} \cap \Omega \to \mathbb{R}^2$, c.f definition (2.1), of the form

$$\begin{aligned} F_\varepsilon(\boldsymbol{\chi}, \Omega) = \sum_{X \in \varepsilon\mathcal{G}\cap\Omega} \Bigg[\frac{1}{2} \sum_{\boldsymbol{\xi} \in R_\varepsilon^{\boldsymbol{\xi}}(\boldsymbol{X},\Omega)} \varepsilon^2 \frac{\sqrt{3}}{2} f_{\mathcal{L}}\left(D_\varepsilon^{\boldsymbol{\xi}}\boldsymbol{\chi}(\boldsymbol{X})\right) \\ + \frac{1}{3} \sum_{\triangle \in R_\varepsilon^\triangle(\boldsymbol{X},\Omega)} \varepsilon^2 \frac{\sqrt{3}}{2} f_{\mathcal{A}}\left(\mathcal{A}_\varepsilon^\triangle \boldsymbol{\chi}(\boldsymbol{X})\right) \Bigg] \end{aligned} \tag{2.2}$$

where

$$\begin{aligned} R_\varepsilon^{\boldsymbol{\xi}}(\boldsymbol{X}, \Omega) &= \{\xi \in \mathcal{G}^{\boldsymbol{\xi}} : [\boldsymbol{X}, \boldsymbol{X} + \varepsilon\boldsymbol{\xi}] \subset \Omega\}, \\ R_\varepsilon^\triangle(\boldsymbol{X}, \Omega) &= \{\triangle \in \mathcal{G}^\triangle : \boldsymbol{X} + \varepsilon\triangle \subset \Omega\}. \end{aligned}$$

In (2.2) the first term is due to pair interactions with nearest neighbours in the hexagonal lattice, where the factor $1/2$ is needed as each interaction is counted twice. The second term represents an energy depending on the enclosed faces / triangular plaquettes in the hexagonal network. Here, the factor $1/3$ accounts for the fact that each triangle is counted three times. The latter term in (2.2), considering "triple" interactions, plays an important role in biomechanical problems. It accounts e.g. for steric repulsion of single polymer filaments in cytoskeletal networks (see Chapter 3). Studying the asymptotic behaviour of lattice systems with "atomistic" interactions usually only pair interactions are considered (Alicandro and Cicalese, 2004). The scaling $\varepsilon^2\sqrt{3}/2$ in (2.2) is the obvious geometrical scaling. It is the only scaling, which yields a nontrivial limit. For further analysis, we adopt the following assumptions:

Assumption 2.1.

- *$f_{\mathcal{L}}$ is a positive super-linearly growing function with p-growth, i.e. $c(|z|^p - 1) \le f_{\mathcal{L}}(z) \le C(|z|^p + 1)$ for $1 \le p < \infty$.*
- *$f_{\mathcal{A}}$ is a positive and bounded function.*

Expression (2.2) considers pair interaction energies $f_{\mathcal{L}}$ independent of the direction of interaction $\boldsymbol{\xi} \in \mathcal{G}^{\boldsymbol{\xi}}$. As we will see in Chapter 4, energies might also depend on $\boldsymbol{\xi}$. For notational convenience, we restrict ourselves to (2.2). But all proofs in the following sections still hold considering a dependence on $\boldsymbol{\xi}$.

Above, we have further restricted ourselves to two-dimensional networks $\varepsilon\mathcal{G} \cap \Omega$ with a hexagonal symmetry. An extension to more general lattices or more dimensions is of course possible.

2.2 A short introduction to Γ-convergence

The theory of Γ-convergence is a very flexible tool for the description of the asymptotic behaviour of variational problems. Here, we give only a brief outline and for more details, we refer to the monographs of Dal Maso (1993) and Braides (2002).

Definition 2.2 (Γ-convergence)**.** *We say that a sequence of functionals* $(F_\varepsilon) : L^p(\Omega;\mathbb{R}^d) \to [0,\infty]$ *Γ-converges in* $L^p(\Omega;\mathbb{R}^d)$ *to a functional* $F : L^p(\Omega;\mathbb{R}^d) \to [0,\infty]$ *as* $\varepsilon \to 0$*, if for all sequences* (ε_j) *converging to* 0 *and for all* $\boldsymbol{u} \in L^p(\Omega;\mathbb{R}^d)$ *the following two conditions hold:*

(i) (lim inf inequality) *for every sequence* $(\boldsymbol{u}_j)$ *converging to* $\boldsymbol{u}$ *in* $L^p(\Omega;\mathbb{R}^d)$

$$F(\boldsymbol{u}) \leq \liminf_j F_{\varepsilon_j}(\boldsymbol{u}_j),$$

(ii) (lim sup inequality) *there exists a sequence* $(\boldsymbol{u}_j)$ *converging to* $\boldsymbol{u}$ *in* $L^p(\Omega;\mathbb{R}^d)$ *such that*

$$F(\boldsymbol{u}) \geq \limsup_j F_{\varepsilon_j}(\boldsymbol{u}_j).$$

The function F *is called the* Γ*-limit of* (F_ε)*, and we write* $F = \Gamma\text{-}\lim_{\varepsilon\to 0} F_\varepsilon$*.*

The concept of Γ-convergence has several nice properties: It is stable under continuous perturbations and it is given in local terms, i.e. one can speak about convergence in one point. But most importantly, it implies a convergence of minimisers and minimum values under suitable assumptions.

Theorem 2.3 (Convergence of minimisers)**.** *Let* $F = \Gamma\text{-}\lim_{\varepsilon\to 0} F_\varepsilon$ *and* F_ε mildly coercive *for all* ε*, i.e. there exists a compact set* $K \subset L^p(\Omega;\mathbb{R}^d)$ *such that* $\inf_{L^p(\Omega;\mathbb{R}^d)} F_\varepsilon = \inf_K F_\varepsilon$ *for all* ε*. Then there exists*

$$\min_{L^p(\Omega;\mathbb{R}^d)} F = \lim_{\varepsilon\to 0} \inf_{L^p(\Omega;\mathbb{R}^d)} F_\varepsilon.$$

Furthermore, if (ε_j) *and* $(\boldsymbol{u}_j)$ *are converging sequences such that* $\lim_j F_{\varepsilon_j}(\boldsymbol{u}_j) = \lim_j \inf_{L^p(\Omega;\mathbb{R}^d)} F_{\varepsilon_j}$*, then its limit is a minimum point for* F*.*

2.3 Γ-convergence result

Energies of the form (2.2) with $f_{\mathcal{L}}$ satisfying Assumption 2.1 and $f_{\mathcal{A}} \equiv 0$ are well studied in the framework of Γ-convergence, e.g. they are a special case of the energies considered by Alicandro and Cicalese (2004). Typical results include existence of the Γ-limit as well as homogenisation formulae, which provide an explicit characterisation of the macroscopic energy functional.

The main idea of Alicandro and Cicalese (2004) is to consider the discrete and continuous energy functionals as pairs function-set and to use corresponding Γ-convergence results.It is then shown that the more or less abstract Γ-convergence result can be made precise by appropriate homogenisation formulae. A constructive proof, calculating the lim inf and lim sup inequalities directly is relatively straight forward in one dimension (see e.g. Braides, 2001). In higher dimensions, the direct calculation of the lim inf inequality is, however, highly non-trivial, unless the problem can be reduced to several one-dimensional problems, e.g. in the direction of the coordinate axes. Due to the "area"-energies $f_{\mathcal{A}}$ such a reduction is not possible here. Let us therefore follow the approach of Alicandro and Cicalese (2004) to show the existence of the Γ-limit and the corresponding homogenisation formula in the case $f_{\mathcal{A}} \neq 0$.

To apply the theory of Γ-convergence, we identify the discrete maps $\boldsymbol{\chi} : \varepsilon\mathcal{G} \cap \Omega \to \mathbb{R}^2$ with maps $\boldsymbol{\chi} : \Omega \to \mathbb{R}^2$ constant on each cell of the lattice, such that the function space to which the functions $\boldsymbol{\chi}$ belong is fixed. Therefore, let us introduce the following function spaces

$$\begin{aligned}\mathcal{F}_\varepsilon(\Omega) \equiv \{\boldsymbol{u} : \Omega \to \mathbb{R}^2 : &\text{ for any } \boldsymbol{X} \in \varepsilon\mathcal{G},\ \boldsymbol{u} \text{ is constant on} \\ &\{\boldsymbol{Y} \in \mathbb{R}^2 : \boldsymbol{Y} = \boldsymbol{X} + \mu_1\boldsymbol{g}_1 + \mu_2\boldsymbol{g}_2,\ 0 \leq \mu_i < \varepsilon\}\},\\ \mathcal{F}_{\varepsilon,\boldsymbol{\phi}}(\Omega) \equiv \{\boldsymbol{u} \in \mathcal{F}_\varepsilon(\Omega) : &\boldsymbol{u}(\boldsymbol{X}) = \boldsymbol{\phi}(\boldsymbol{X}) \text{ if } \operatorname{dist}(\boldsymbol{X}, \partial\Omega) < 1\}.\end{aligned}$$

Of course other embeddings, e.g. assuming piecewise linear functions, can be considered equivalently.

Theorem 2.4. *Let $\Omega \subset \mathbb{R}^2$ be bounded; let $f_{\mathcal{L}}$ and $f_{\mathcal{A}}$ satisfy Assumption 2.1. Then for every sequence (ε_j) of positive real numbers converging to 0, there exists a subsequence (ε_{j_k}) and a continuous quasi-convex function $\Psi : \mathbb{R}^{2\times 2} \to [0,\infty)$ satisfying*

$$c(|\boldsymbol{M}|^p - 1) \leq \Psi(\boldsymbol{M}) \leq C(|\boldsymbol{M}|^p + 1)$$

with $0 < c < C$, such that $(F_{\varepsilon_{j_k}}(\cdot,\cdot))$ given in (2.2) Γ-converges with respect to the $L^p(\Omega;\mathbb{R}^2)$-topology to the functional $F : L^p(\Omega;\mathbb{R}^2) \times \{A \subset \Omega\text{: } A \text{ open}\} \to [0,\infty]$ defined as

$$F(\boldsymbol{\chi}, A) = \begin{cases} \int_A \Psi(\nabla\boldsymbol{\chi})d\mu & \text{if } \boldsymbol{\chi} \in W^{1,p}(A;\mathbb{R}^2) \\ \infty & \text{otherwise.} \end{cases} \tag{2.3}$$

As already mentioned, Alicandro and Cicalese (2004, Theorem 3.3) consider the energies (2.2) with $f_{\mathcal{A}} \equiv 0$ and their Γ-limits as functionals defined on pairs function-set. They show that the upper and lower Γ-limits are inner-regular increasing set functions. This allows the use of a corresponding compactness and integral representation result (Braides and Defranceschi, 1998). Considering the case $f_{\mathcal{A}} \neq 0$ the arguments of Alicandro and Cicalese (2004) can be repeated. The "difficult" part are the pair interactions $f_{\mathcal{L}}$. Because the energy $f_{\mathcal{A}}$ is bounded, the proof of Theorem 2.4 goes along the lines of the original proof.

Theorem 2.4 considers an unconstrained Γ-limit. However, often one is interested in problems with prescribed boundary conditions. Corresponding convergence results with restrictions to $\boldsymbol{\chi} \in \mathcal{F}_{\varepsilon,\boldsymbol{\phi}}$, and accordingly $\boldsymbol{\chi} - \boldsymbol{\phi} \in W_0^{1,p}(\Omega;\mathbb{R}^2)$, can be proven (Alicandro and Cicalese, 2004, Theorem 3.10). A similar result holds for periodic boundary conditions (Alicandro and Cicalese, 2004, Theorem 3.12).

The embedding of $W^{1,p}(\Omega;\mathbb{R}^2)$ to $L^p(\Omega;\mathbb{R}^2)$ is compact (Alt, 2002a). Hence, Theorem 2.4 implies also the convergence of minimisers to a minimiser of the limit functional (Alicandro and Cicalese, 2004, Theorem 3.3):

Corollary 2.5. *Let $\Omega \subset \mathbb{R}^2$ be bounded; let $f_{\mathcal{L}}$ and $f_{\mathcal{A}}$ satisfy Assumption 2.1. Additionally, let (ε_{j_k}) be the converging subsequence of Theorem 2.4. Then, for all open $A \subset \Omega$ we have*

$$\lim_k \inf\{F_{\varepsilon_{j_k}}(\boldsymbol{\chi}, A) : \boldsymbol{\chi} \in \mathcal{F}_{\varepsilon_{j_k}}(A)\} = \min\{F(\boldsymbol{\chi}, A) : \boldsymbol{\chi} \in W^{1,p}(A;\mathbb{R}^2)\}$$

with $F_{\varepsilon_{j_k}}(\boldsymbol{\chi}_{\varepsilon_{j_k}}, A)$ as in (2.2) and $F(\boldsymbol{\chi}, A)$ given by (2.3). Moreover, if $(\boldsymbol{\chi}_k)$ is a converging sequence such that

$$\lim_k F_{\varepsilon_{j_k}}(\boldsymbol{\chi}_k, A) = \lim_k \inf\{F_{\varepsilon_{j_k}}(\boldsymbol{\chi}, A) : \boldsymbol{\chi} \in \mathcal{F}_{\varepsilon_{j_k}}(A)\},$$

then its limit is a minimiser for $\min\{F(\boldsymbol{\chi}, A) : \boldsymbol{\chi} \in W^{1,p}(A;\mathbb{R}^2)\}$.

The corollary holds also in the case of Dirichlet (Alicandro and Cicalese, 2004, Corollary 3.11) or periodic boundary conditions (Alicandro and Cicalese, 2004, Corollary 3.13).

2.3.1 Homogenisation

Let us first define the "rectangle"

$$Q_N = \{\boldsymbol{X} : \boldsymbol{X} = \mu_1 \boldsymbol{g}_1 + \mu_2 \boldsymbol{g}_2 \text{ with } 0 \leq \mu_i < N,\ i = 1, 2\ \}.$$

In analogy to the approach of Alicandro and Cicalese (2004), the following homogenisation result holds:

Theorem 2.6. *Let $\Omega \subset \mathbb{R}^2$ be bounded; let $f_{\mathcal{L}}$ and $f_{\mathcal{A}}$ satisfy Assumption 2.1. Then for every sequence (ε_j) of positive real numbers converging to 0, the sequence (F_{ε_j}) given in (2.2) Γ-converges with respect to the $L^p(\Omega;\mathbb{R}^2)$-topology to $F : L^p(\Omega;\mathbb{R}^2) \times \{A \subset \Omega : \ A \text{ open } \} \to [0,\infty]$ defined as*

$$F(\boldsymbol{\chi}, A) = \begin{cases} \int_A \Psi_{hom}(\nabla \boldsymbol{\chi}) d\mu & \text{if } \boldsymbol{\chi} \in W^{1,p}(A;\mathbb{R}^2) \\ \infty & \text{otherwise,} \end{cases} \tag{2.4}$$

where the integrand $\Psi : \mathbb{R}^{2\times 2} \to [0,\infty)$ satisfies the homogenisation formula

$$\Psi_{hom}(\boldsymbol{M}) = \lim_{N\to\infty} \frac{1}{N^2} \min\Bigg\{ \sum_{\boldsymbol{X}\in\mathcal{G}\cap Q_N} \Bigg[\frac{1}{2} \sum_{\boldsymbol{\xi}\in R_1^{\boldsymbol{\xi}}(\boldsymbol{X},Q_N)} f_{\mathcal{L}}\left(D_1^{\boldsymbol{\xi}}\boldsymbol{\chi}(\boldsymbol{X})\right) + \frac{1}{3} \sum_{\triangle\in R_1^{\triangle}(\boldsymbol{X},Q_N)} f_{\mathcal{A}}\left(\mathcal{A}_1^{\triangle}\boldsymbol{\chi}(\boldsymbol{X})\right) \Bigg] : \boldsymbol{\chi} \in \mathcal{F}_{1,\boldsymbol{M}\cdot\boldsymbol{X}}(Q_N) \Bigg\}. \tag{2.5}$$

An analogous result holds also in the case of Dirichlet or periodic boundary conditions with the same characterisation of Ψ_{hom}.

Proof. By the definition of Γ-convergence, the Γ-limit $F(\boldsymbol{\chi})$ is a lower semicontinuous function (Braides, 2002, Proposition 1.28). Hence, Ψ_{hom} is a quasi-convex function (Dacorogna, 1989, Chapter 4, Theorem 2.1), i.e. for all $A \subset \Omega$, $\boldsymbol{M} \in \mathbb{R}^{2\times 2}$, and $\boldsymbol{\chi} - \boldsymbol{M}\cdot\boldsymbol{X} \in W_0^{1,p}(A;\mathbb{R}^2)$ we have by definition of quasi-convexity

$$\Psi_{\text{hom}}(\boldsymbol{M}) \le \frac{1}{|A|} \int_A \Psi(\nabla\boldsymbol{\chi}) d\mu.$$

Due to the p-growth property of F (Theorem 2.4), and accordingly of Ψ_{hom}, we obtain (Dacorogna, 1989, Chapter 4, Theorem 2.9)

$$\begin{aligned} \Psi_{\text{hom}}(\boldsymbol{M}) &= \frac{1}{|A|} \min\left\{ \int_A \Psi(\nabla\boldsymbol{\chi}) d\mu : \boldsymbol{\chi} - \boldsymbol{M}\cdot\boldsymbol{X} \in W_0^{1,p}(A;\mathbb{R}^2) \right\} \\ &= \frac{1}{|A|} \min\left\{ F(\boldsymbol{\chi}, A) : \boldsymbol{\chi} - \boldsymbol{M}\cdot\boldsymbol{X} \in W_0^{1,p}(A;\mathbb{R}^2) \right\} \end{aligned}$$

for any open $A \subset \Omega$ and $\boldsymbol{M} \in \mathbb{R}^{2\times 2}$. Using Corollary 2.5 in the case of Dirichlet boundary conditions (Alicandro and Cicalese, 2004, Corollary 3.11), yields

$$\Psi_{\text{hom}}(\boldsymbol{M}) = \frac{1}{|A|} \liminf_N \left\{ F_{\varepsilon_N}(\boldsymbol{\chi}, A) : \boldsymbol{\chi} \in \mathcal{F}_{\varepsilon_N, \boldsymbol{M}\cdot\boldsymbol{X}} \right\}.$$

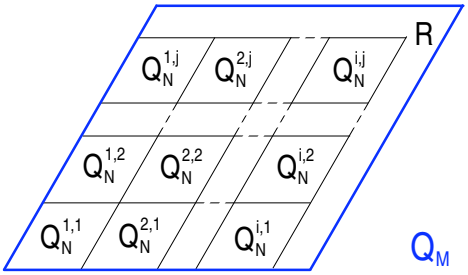

Fig. 2.2. Tessellation of the "rectangle" Q_M with "rectangles" Q_N.

Without loss of generality, let us consider $\varepsilon_N = \frac{1}{N}$ and $A = Q_1$, i.e. $|A| = \sqrt{3}/2$. After rescaling

$$\tilde{\boldsymbol{X}} = \frac{1}{\varepsilon_N}\boldsymbol{X}, \quad \tilde{\boldsymbol{\chi}}(\tilde{\boldsymbol{X}}) = \frac{1}{\varepsilon_N}\boldsymbol{\chi}(\varepsilon_N\tilde{\boldsymbol{X}}),$$

we recover

$$\Psi_{\hom}(\boldsymbol{M}) = \lim_{N\to\infty} \Psi_N(\boldsymbol{M}) \tag{2.6}$$

with

$$\Psi_N(\boldsymbol{M}) = \frac{1}{N^2}\min\Bigg\{\sum_{\mathcal{G}\cap Q_N}\Bigg[\frac{1}{2}\sum_{R_1^{\boldsymbol{\xi}}(\boldsymbol{X},Q_N)} f_{\mathcal{L}}\left(D_1^{\boldsymbol{\xi}}\boldsymbol{\chi}(\boldsymbol{X})\right) + \frac{1}{3}\sum_{R_1^{\triangle}(\boldsymbol{X},Q_N)} f_{\mathcal{A}}\left(\mathcal{A}_1^{\triangle}\boldsymbol{\chi}(\boldsymbol{X})\right)\Bigg] : \boldsymbol{\chi}\in\mathcal{F}_{1,\boldsymbol{M}\cdot\boldsymbol{X}}(Q_N)\Bigg\}.$$

Formula (2.5) is obtained and Theorem 2.6 is proven, once we show that the limit (2.6) exists (see next proposition). □

Proposition 2.7. *For all $\boldsymbol{M}\in\mathbb{R}^{2\times 2}$ the limit $\Psi(\boldsymbol{M}) = \lim_N \Psi_N(\boldsymbol{M})$ exists.*

Proof. For given $\boldsymbol{M}\in\mathbb{R}^{2\times 2}$ and $M,\ N\in\mathbb{N}$ let us consider a tessellation of Q_M with translates Q_N, numbered $Q_N^{i,j}$ as shown in Fig. 2.2. In addition, we choose $\boldsymbol{\chi}_M\in\mathcal{F}_{1,\boldsymbol{M}\cdot\boldsymbol{X}}(Q_N)$ such that

$$\boldsymbol{\chi}_M = \begin{cases} \boldsymbol{\chi}_N(\boldsymbol{X} - iN\boldsymbol{g}_1 - jN\boldsymbol{g}_2) + \boldsymbol{M}\cdot(iN\boldsymbol{g}_1 + jN\boldsymbol{g}_2) & \text{if } \boldsymbol{X}\in Q_N^{i,j} \\ \boldsymbol{M}\cdot\boldsymbol{X} & \text{otherwise,}\end{cases}$$

where $\boldsymbol{\chi}_N\in\mathcal{F}_{1,\boldsymbol{M}\cdot\boldsymbol{X}}(Q_N)$ is a minimiser for Ψ_N. Thus, we obtain

$$\Psi_M(\boldsymbol{M}) \le \frac{1}{M^2}\sum_{\mathcal{G}\cap Q_M}\Bigg[\frac{1}{2}\sum_{R_1^{\boldsymbol{\xi}}(X,Q_M)} f_{\mathcal{L}}\left(D_1^{\boldsymbol{\xi}}\boldsymbol{\chi}(\boldsymbol{X})\right) + \frac{1}{3}\sum_{R_1^{\triangle}(X,Q_M)} f_{\mathcal{A}}\left(\mathcal{A}_1^{\triangle}\boldsymbol{\chi}(\boldsymbol{X})\right)\Bigg].$$

The right hand side can be split up into problems on the domains $Q_N^{i,j}$ plus some correction accounting for interactions across the boundaries of the tessellation $Q_N^{i,j}$

and for interactions in the rest $R = Q_M \setminus \cup Q_N^{i,j}$. Since in these regions the deformation equals $\boldsymbol{M} \cdot \boldsymbol{X}$ by construction, we can estimate

$$\begin{aligned}\Psi_M(\boldsymbol{M}) &\leq \frac{1}{N^2} \sum_{\mathcal{G} \cap Q_N} \left[\frac{1}{2} \sum_{R_1^{\boldsymbol{\xi}}(X, Q_N)} f_{\mathcal{L}} \left(D_1^{\boldsymbol{\xi}} \boldsymbol{\chi}(\boldsymbol{X}) \right) + \frac{1}{3} \sum_{R_1^{\triangle}(X, Q_N)} f_{\mathcal{A}} \left(\mathcal{A}_1^{\triangle} \boldsymbol{\chi}(\boldsymbol{X}) \right) \right] \\ &\qquad + C\left(\frac{1}{N} + \frac{N}{M}\right)(1 + |\boldsymbol{M}|^p) \\ &\leq \Psi_N(\boldsymbol{M}) + C\left(\frac{1}{N} + \frac{N}{M}\right)(1 + |\boldsymbol{M}|^p).\end{aligned}$$

Taking first the lim sup in M and then the lim inf in N the proposition is proven. □

With respect to the derivation of a cell problem formula (Section 2.3.2), the following equivalent characterisation of Ψ_{hom} will be useful (Alicandro and Cicalese, 2004, Remark 4.4):

Remark 2.8. *The function Ψ_{hom} of Theorem 2.6 also satisfies*

$$\begin{aligned}\Psi_{hom}(\boldsymbol{M}) = \lim_{N \to \infty} \frac{1}{N^2} \min \Bigg\{ \sum_{\boldsymbol{X} \in \varepsilon \mathcal{G} \cap Q_h} \Bigg[\frac{1}{2} \sum_{\boldsymbol{\xi} \in R_1^{\boldsymbol{\xi}}(\boldsymbol{X}, Q_N)} f_{\mathcal{L}} \left(D_1^{\boldsymbol{\xi}} \boldsymbol{\chi}(\boldsymbol{X}) \right) \\ + \frac{1}{3} \sum_{\triangle \in R_1^{\triangle}(\boldsymbol{X}, Q_N)} f_{\mathcal{A}} \left(\mathcal{A}_1^{\triangle} \boldsymbol{\chi}(\boldsymbol{X}) \right) \Bigg] : \\ \boldsymbol{\chi} = \boldsymbol{M} \cdot \boldsymbol{X} + \boldsymbol{u} \text{ with } (N-2)\text{-periodic } \boldsymbol{u} \in \mathcal{F}_1(Q_N) \Bigg\}.\end{aligned} \tag{2.7}$$

Above, $(N-2)$-periodic functions $\boldsymbol{u}$, i.e. $\boldsymbol{u}(\boldsymbol{X} + (N-2)\boldsymbol{g}_1) = \boldsymbol{u}(\boldsymbol{X})$ as well as $\boldsymbol{u}(\boldsymbol{X} + (N-2)\boldsymbol{g}_2) = \boldsymbol{u}(\boldsymbol{X})$, are considered to ensure that the discrete derivative of the perturbation on the boundary is zero.

2.3.2 A cell problem

The homogenisation formula (2.5), and accordingly (2.7), is given as a minimisation problem over a growing rectangle Q_N ($N \to \infty$). Under the assumption of convexity for the functions $f_{\mathcal{L}}$ and $f_{\mathcal{A}}$, the homogenisation formula can be reduced to a cell problem:

Theorem 2.9. *Let $\Omega \subset \mathbb{R}^2$ be bounded. Additionally, let $f_{\mathcal{L}}$ and $f_{\mathcal{A}}$ be convex functions, which satisfy Assumption 2.1. Then the conclusion of Theorem 2.6 holds, with $\Psi_{hom}(\boldsymbol{M})$ given by*

$$\Psi_{hom}(\boldsymbol{M}) = \frac{1}{2} \sum_{\boldsymbol{\xi} \in \mathcal{G}^{\boldsymbol{\xi}}} f_{\mathcal{L}} \left(\boldsymbol{M} \cdot \boldsymbol{\xi} \right) + \frac{1}{3} \sum_{\triangle \in \mathcal{G}^{\triangle}} f_{\mathcal{A}} \left(\det \boldsymbol{M} \right). \tag{2.8}$$

Proof. For simplicity, we split the proof into two parts: (a) the case $f_{\mathcal{A}} \equiv 0$ and (b) $f_{\mathcal{L}} \equiv 0$. For all N, we show that in both cases $\boldsymbol{\chi} = \boldsymbol{M} \cdot \boldsymbol{X}$ is a minimiser of (2.5), or rather (2.7). Since $f_{\mathcal{L}}$ and $f_{\mathcal{A}}$ are non-negative, the minimum in the general case $f_{\mathcal{L}} \neq 0$ and $f_{\mathcal{A}} \neq 0$ is also realised by $\boldsymbol{\chi} = \boldsymbol{M} \cdot \boldsymbol{X}$, i.e. formula (2.8) holds.

Case (a): $f_{\mathcal{A}} \equiv 0$

Set $f_{\mathcal{A}} \equiv 0$ and let us show that $\boldsymbol{\chi}_{\min} = \boldsymbol{M} \cdot \boldsymbol{X} + \boldsymbol{u}_{\min}$, with $\boldsymbol{u}_{\min}$ constant, is a solution of the minimisation problem (2.7) independent of N. That is, among all $(N-2)$-periodic functions $\boldsymbol{u} \in \mathcal{F}_1(Q_N)$ the energy

$$F_1(\boldsymbol{M} \cdot \boldsymbol{X} + \boldsymbol{u}, Q_N) = \sum_{\varepsilon\mathcal{G} \cap Q_N} \frac{1}{2} \sum_{R_1^{\boldsymbol{\xi}}(\boldsymbol{X}, Q_N)} f_{\mathcal{L}} \left(D_1^{\boldsymbol{\xi}} \left(\boldsymbol{M} \cdot \boldsymbol{X} + \boldsymbol{u}(\boldsymbol{X}) \right) \right) \tag{2.9}$$

is minimised by $\boldsymbol{u}_{\min}$ constant. Let us choose an arbitrary minimiser $\tilde{\boldsymbol{u}}_{\min} \in \mathcal{F}_1(Q_N)$ of F_1 given by (2.9). By definition, the minimiser is at least $N-2$ periodic. Hence, the function $\tilde{\boldsymbol{u}}(\boldsymbol{X}) \in \mathcal{F}_1(Q_N)$ defined by

$$\tilde{\boldsymbol{u}}(\boldsymbol{X}) = \frac{1}{(N-2)^2} \sum_{i,j \in [0, N-2]} \tilde{\boldsymbol{u}}_{\min}(\boldsymbol{X} + i\boldsymbol{g}_1 + j\boldsymbol{g}_2)$$

is one periodic and thus constant by construction of $\mathcal{F}_1(Q_N)$. By convexity of $f_{\mathcal{L}}$ and hence convexity of F_1 given by (2.9), the function $\tilde{\boldsymbol{u}}$ satisfies the inequality

$$F_1(\boldsymbol{M} \cdot \boldsymbol{X} + \tilde{\boldsymbol{u}}, Q_N) \leq \frac{1}{(N-2)^2} \sum_{i,j \in [0, N-2]} F_1 \left(\boldsymbol{M} \cdot \boldsymbol{X} + \tilde{\boldsymbol{u}}_{\min} \left(\boldsymbol{X} + i\boldsymbol{g}_1 + j\boldsymbol{g}_2 \right), Q_N \right).$$

Since F_1 depends only on the gradient of $\boldsymbol{\chi}$, it is invariant under a shift, e.g. under the shift $\boldsymbol{X} + i\boldsymbol{g}_1 + j\boldsymbol{g}_2$. Hence, we can conclude

$$F_1(\boldsymbol{M} \cdot \boldsymbol{X} + \tilde{\boldsymbol{u}}, Q_N) \leq \frac{1}{(N-2)^2} \sum_{i,j \in [0, N-2]} F_1 \left(\boldsymbol{M} \cdot \boldsymbol{X} + \tilde{\boldsymbol{u}}_{\min} \left(\boldsymbol{X} \right), Q_N \right). \tag{2.10}$$

Therefore also $\tilde{\boldsymbol{u}}(\boldsymbol{X})$ is a minimiser of F_1, and accordingly $\boldsymbol{\chi}_{\min}(\boldsymbol{X}) = \boldsymbol{M} \cdot \boldsymbol{X} + \tilde{\boldsymbol{u}}(\boldsymbol{X})$. Since $\tilde{\boldsymbol{u}}(\boldsymbol{X})$ is an arbitrary constant and $F_1(\boldsymbol{\chi}, Q_N)$ depends only on the discrete gradient of $\boldsymbol{\chi}$, we can choose $\boldsymbol{\chi}_{\min}(\boldsymbol{X}) = \boldsymbol{M} \cdot \boldsymbol{X}$. If $f_{\mathcal{L}}$ is strictly convex, inequality (2.10) is strict, which implies uniqueness of the minimiser (up to a constant).

Case (b): $f_{\mathcal{L}} \equiv 0$

Choose $f_{\mathcal{L}} \equiv 0$ and let us prove that $\boldsymbol{\chi}_{\min} = \boldsymbol{M} \cdot \boldsymbol{X}$ is also a solution of the minimisation problem (2.5) for all N. That is, it minimises

$$F_1(\boldsymbol{\chi}, Q_N) = \sum_{\mathcal{G} \cap Q_N} \frac{1}{3} \sum_{R_1^{\triangle}(\boldsymbol{X}, Q_N)} f_{\mathcal{A}} \left(\mathcal{A}_1^{\triangle} \boldsymbol{\chi}(\boldsymbol{X}) \right) \tag{2.11}$$

among all $\boldsymbol{\chi} \in \mathcal{F}_{1, \boldsymbol{M} \cdot \boldsymbol{X}}(Q_N)$.

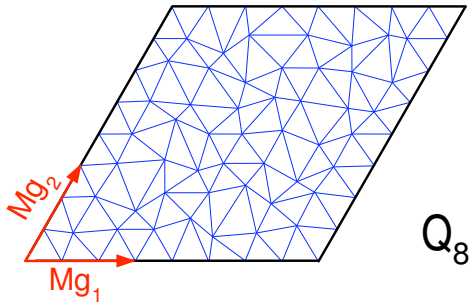

Fig. 2.3. Deformation of a given network

Let us fix N. For all deformations $\boldsymbol{\chi} \in \mathcal{F}_{1,\boldsymbol{M}\cdot\boldsymbol{X}}(Q_N)$ the total area of Q_N after the deformation equals $N^2\sqrt{3}/2 \det \boldsymbol{M}$, since it depends only on the value of $\boldsymbol{\chi}$ on ∂Q_N (see also Fig. 2.3) and $|Q_N| = N^2\sqrt{3}/2$. Hence, it follows

$$N^2 \frac{\sqrt{3}}{2} \det \boldsymbol{M} = \sum_{\mathcal{G}\cap Q_N} \sum_{R_1^{\triangle}(\boldsymbol{X},Q_N)} \frac{\sqrt{3}}{4} \mathcal{A}_1^{\triangle} \boldsymbol{\chi}(\boldsymbol{X}) \tag{2.12}$$

for all $\boldsymbol{\chi} \in \mathcal{F}_{1,\boldsymbol{M}\cdot\boldsymbol{X}}(Q_N)$. The energy $F_1(\boldsymbol{\chi}, Q_N)$ given by (2.11) can be minimised only by a variation of the triangular plaquette areas $\mathcal{A}_1^{\triangle}(\boldsymbol{M}\cdot\boldsymbol{X})$ under the constraint that the sum (total area) is constant. Using $\mathcal{A}_1^{\triangle}(\boldsymbol{M}\cdot\boldsymbol{X}) = \det \boldsymbol{M}$ and (2.12), we obtain for arbitrary $\boldsymbol{\chi} \in \mathcal{F}_{1,\boldsymbol{M}\cdot\boldsymbol{X}}(Q_N)$

$$\begin{aligned}\sum_{\mathcal{G}\cap Q_N} \sum_{R_1^{\triangle}(\boldsymbol{X},Q_N)} f_{\mathcal{A}}(\mathcal{A}_1^{\triangle}\boldsymbol{M}\cdot\boldsymbol{X}) &= 2N^2 f_{\mathcal{A}}(\det \boldsymbol{M}) \\ &= 2N^2 f_{\mathcal{A}}\Big(\frac{1}{2N^2} \sum_{\mathcal{G}\cap Q_N} \sum_{R_1^{\triangle}(\boldsymbol{X},Q_N)} \mathcal{A}_1^{\triangle}\boldsymbol{\chi}(\boldsymbol{X})\Big).\end{aligned}$$

By convexity of $f_{\mathcal{A}}$, have

$$\sum_{\mathcal{G}\cap Q_N} \sum_{R_1^{\triangle}(\boldsymbol{X},Q_N)} f_{\mathcal{A}}(\mathcal{A}_1^{\triangle}\boldsymbol{M}\cdot\boldsymbol{X}) \leq \sum_{\mathcal{G}\cap Q_N} \sum_{R_1^{\triangle}(\boldsymbol{X},Q_N)} f_{\mathcal{A}}(\mathcal{A}_1^{\triangle}\boldsymbol{\chi}(\boldsymbol{X})) \tag{2.13}$$

for any $\boldsymbol{\chi} \in \mathcal{F}_{1,\boldsymbol{M}\cdot\boldsymbol{X}}(Q_N)$. The energy of the deformation $\boldsymbol{\chi} = \boldsymbol{M}\cdot\boldsymbol{X}$ is smaller than or equal to the energy of any other deformation $\boldsymbol{\chi}$, which shows $\boldsymbol{\chi}_{\min} = \boldsymbol{M}\cdot\boldsymbol{X}$ and thus completes the proof. Considering strictly convex $f_{\mathcal{A}}$ the inequality (2.13) is strict yielding uniqueness of the minimiser. □

The homogenisation formula (2.8) of Theorem 2.9 can be evaluated explicitly and allows us to determine directly the limit functional (2.5) stated in Theorem 2.6. In Chapter 3, this formula enables us to calculate the corresponding macroscopic energy for red blood cells and in Chapter 4 it is used to calculate the energy corresponding to deformations of growing cell cultures.

2.4 Energies as constitutive relations

So far, we have considered only energy minimisation problems, i.e. the deformation due to mechanics is given by the minimal energy configuration. Rather than such a static approach, one is sometimes also interested in dynamics, which are determined by the balance of momentum. Therefore, corresponding stress tensors $\boldsymbol{\sigma}$ need to be determined. An extension to dynamics is possible using a thermodynamic approach.

Assumption 2.10. *Energy supplied to the system is stored only as mechanical energy, i.e. the free energy density Ψ is a function of the deformation tensor $\boldsymbol{F}$ alone. Furthermore, for any isothermal motion the mechanical work done on the material is equal to the rate of change of free energy.*

This assumption implies perfect reversibility under isothermal conditions, as well as history and rate independence. If Assumption 2.10 holds, the stress tensor $\boldsymbol{\sigma}$ can be calculated as shown below. The energy density Ψ serves as a constitutive relation, which is a standard characterisation for so-called hyperelastic materials.

Proposition 2.11. *Under Assumption 2.10 the energy plays the role of a constitutive relation, i.e. we can characterise the relationship between stress and strain using the free energy density Ψ:*

$$\sigma_{ij} = \frac{\rho_0}{J} \sum_k \frac{\partial \Psi}{\partial F_{ik}} F^T_{kj}, \tag{2.14}$$

where $\boldsymbol{F}$ is the deformation tensor, $J = \det \boldsymbol{F}$ its Jacobian, and $\rho_0 = \rho J$ the material density in the reference configuration.

Proof. Let us calculate first the temporal change of the free energy

$$\begin{aligned} \frac{d}{dt} \int_\Omega \rho \Psi d\mu &= \frac{d}{dt} \int_{\Omega_0} \rho_0 \Psi d\mu_0 \\ &= \int_{\Omega_0} \rho_0 \boldsymbol{\Psi'} : \frac{d}{dt} \boldsymbol{F} d\mu_0 \\ &= \int_{\Omega_0} \rho_0 (\boldsymbol{\Psi'} \cdot \boldsymbol{F}^T) : \boldsymbol{L} d\mu_0, \end{aligned} \tag{2.15}$$

where $\frac{d}{dt}\boldsymbol{F} = \boldsymbol{L} \cdot \boldsymbol{F}$ and $\boldsymbol{L} = \nabla \boldsymbol{v}$ is the stretch rate tensor ($\boldsymbol{v}$ is the material speed). Using $power = \int force \cdot velocity \; d\mu$, we recover in terms of Assumption 2.10

$$\frac{d}{dt} \int_{\Omega_0} \rho_0 \Psi d\mu_0 = \int_{\Omega_0} \boldsymbol{\sigma} : \boldsymbol{D} J d\mu_0 = \int_{\Omega_0} \boldsymbol{\sigma} : \boldsymbol{L} J d\mu_0, \tag{2.16}$$

where $\boldsymbol{D} = \frac{1}{2}(\boldsymbol{L} + \boldsymbol{L}^T)$ is the symmetric stretch rate tensor. The last equality in (2.16) relies on the symmetry of the stress tensor $\boldsymbol{\sigma}$.

Comparing expression (2.15) with expression (2.16), the characterisation (2.14) of the stress tensor is recovered. □

Equation (2.15) can be easily illustrated using the balance of linear momentum, i.e. $\frac{\partial}{\partial t}(\rho \boldsymbol{v}) + \nabla \cdot (\rho \boldsymbol{v} \otimes \boldsymbol{v}) = \nabla \cdot \boldsymbol{\sigma}$, and accordingly using balance of mass $\rho \frac{d}{dt}\boldsymbol{v} = \nabla \cdot \boldsymbol{\sigma}$. Testing the balance of linear momentum with the material speed $\boldsymbol{v}$, integrating with respect to Ω_0, assuming no momentum flux across the boundaries ($\boldsymbol{\sigma} \cdot \boldsymbol{n} = \boldsymbol{0}$), and using the symmetry of $\boldsymbol{\sigma}$, one has

$$\frac{d}{dt}\int_{\Omega_0} \frac{1}{2}\rho_0 \boldsymbol{v}^2 d\mu_0 = -\int_{\Omega_0} \boldsymbol{\sigma} : \boldsymbol{D} J d\mu_0. \tag{2.17}$$

The right hand side of (2.17) equals the change of the kinetic energy. If we assume that no energy is lost, the change in the kinetic energy must equal minus the change in the free energy, i.e. $\frac{d}{dt}\int_{\Omega_0} \rho_0 \boldsymbol{v}^2 d\mu_0 = -\frac{d}{dt}\int_{\Omega_0} \rho_0 \Psi d\mu_0$, and hence (2.15) is recovered.

The characterisation of the stress tensor $\boldsymbol{\sigma}$ using a thermodynamic framework, i.e. Proposition 2.11, agrees with the following characterisation:

Corollary 2.12. *Forces are determined by the steepest decent of the L^2- gradient of the free energy:*

$$\int_{\Omega} (\nabla \cdot \boldsymbol{\sigma}) \cdot \boldsymbol{\phi} d\mu = -\frac{d}{d\varepsilon}\int_{\Omega_0} \rho_0 \Psi(\nabla_0 \boldsymbol{x} + \varepsilon \nabla_0 \boldsymbol{\phi}) d\mu_0 \Big|_{\varepsilon=0} \tag{2.18}$$

with $\boldsymbol{\phi} \in C^\infty(\Omega_0; \mathbb{R}^n)$.

Expression (2.18) can be related directly to the thermodynamic approach of Proposition 2.11 by considering small variations $\boldsymbol{x} + \delta\boldsymbol{x} = \boldsymbol{x} + \boldsymbol{v}\delta t$.

2.4.1 Principle of virtual work

The characterisation of the stress tensor is not only useful in a dynamic framework. Following the classical method of the calculus of variations, the principle of virtual work can be used to determine energy minimising configurations:

Let us consider a deformation $\boldsymbol{\chi}$ such that the solid is in an equilibrium state, i.e. the free energy $\int_{\Omega_0} \rho_0 \Psi d\mu_0$ is (locally) minimal. The principle of virtual work states that if the solid is subject to infinitesimal deformations in any direction (so-called virtual displacements), the (virtual) work of all external forces is zero. Hence, the energy of the solid does not change. And conversely, if the total (virtual) work of all external forces acting on a solid is zero then the body is in equilibrium. That is, if the variation of the energy (2.18) vanishes, the body is in equilibrium and accordingly a local energy minimum is attained.

The consideration of infinitesimal deformations corresponds to the derivation of the weak form of the Euler-Lagrange equations via Corollary 2.12. The so-called classical method in the calculus of variations.

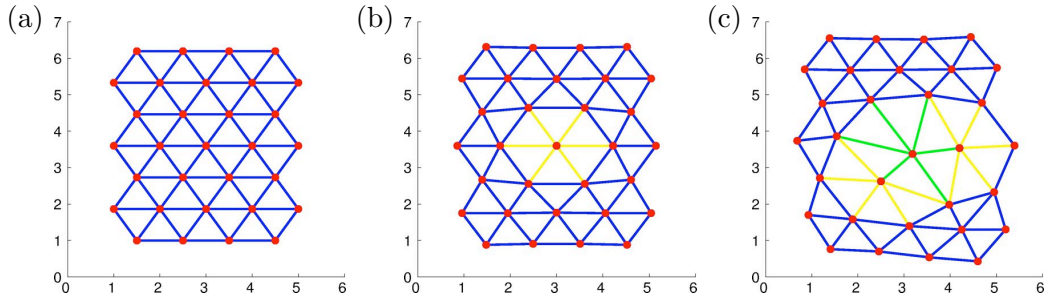

Fig. 2.4. Minimal energy configurations of a network modelling a growing cell culture: Each vertex corresponds to a cell and edges correspond to mechanical interactions. The energy corresponding to the deformation of a link with length $\mathcal{L}^i$ is given by $E^i(\mathcal{L}^i) = (\mathcal{L}^i_0 - \mathcal{L}^i)^2$, where $\mathcal{L}^i_0$ is the rest length of the link. Growth, encoded by colours, implies an increasing distance/rest length to the neighbouring cells.

2.5 Evolving networks

So far, we have considered only static networks which do not evolve in time. In many biomechanical applications, this might not be the case, e.g. the properties of single links could alter or even the network topology could change. An example of such an evolving network are growing cell cultures considered in Chapter 4 (see also Fig. 2.4). Considering growing cell cultures, the network topology is fixed, but the properties of single links change depending on growth. One difficulty considering evolving networks and non-static mechanics at the same time is a possible emergence of dissipation due to an evolution of the network (Di Carlo and Quiligotti, 2002).

Therefore, we investigate in this thesis only examples where the dynamics of network evolution are significantly slower than mechanics. We can therefore adopt the following assumption, which is often considered in the theory of plasticity and also for growing cell cultures (Lubarda, 2004):

Assumption 2.13. *The time scale of mechanics, i.e. the time scale on which an equilibrium is attained, is much faster than the time scale of network modifications.*

Lifting the assumption of quasi-steady mechanics, special care has to be taken about thermodynamically admissible evolution laws for the network / system. Such laws are discussed e.g. by Di Carlo and Quiligotti (2002) and Ambrosi and Guana (2005) in the case of growing materials.

2.6 Summary and discussion

In this chapter, we have investigated the connection between discrete mechanical systems on a microscale and the continuous macroscopic counterparts. The examples considered in this thesis are only of a static, alternatively quasi-static, type. Therefore, we have restricted our analysis to energy functionals and energy minimising deformations.

Using the quite advanced theory of Γ-convergence, we have set forth how a discrete description of simple periodic networks converges to a continuum description when the typical length scale of the network converges to zero. The concept of Γ-convergence is a variational theory and implies a convergence of the energies as well as their minimisers. Here, we have extended the approach of Alicandro and Cicalese (2004). Recently a more direct approach considering the passage from a discrete to a continuum theory has been proposed by Schmidt (2005). This ansatz should principally be also applicable for the energies considered here and should be considered in the future.

Further, the continuous energy functionals have been characterised by an auxiliary minimisation problem. The latter could be reduced to a cell problem formula assuming convexity of the discrete interactions. That the discrete energy functionals and their minimisers can be explicitly characterised by continuous descriptions via cell problems in the limit of a vanishing network length scale is far from being obvious, as shown by Friesecke and Theil (2002).

So far, we have not derived rigorous error estimates. With respect to applications error estimates are useful and should be investigated in the future. In addition, extensions with respect to more general energies might be possible (Schmidt, 2005). As we will see in the case of red blood cells (Chapter 3), such a generalisation should be addressed in the future. It is further possible to consider networks with long range interactions in the framework of Γ-convergence (Schmidt, 2005; Alicandro and Cicalese, 2004). If such general interactions are, however, relevant in biomechanics is not clear.

The restriction to periodic and symmetric networks has been made for mathematical reasons. Although many networks considered in biomechanics are quite regular, e.g. the spectrin network of red blood cells, a perfect symmetry is rarely the case. Non-symmetric or "thermodynamical" networks might however exhibit a different behaviour (Discher et al., 1997). Therefore, the investigation of non-symmetric networks is a topic of high importance which has to be investigated from a rigorous mathematical point of view in the future. The restriction to hexagonal symmetries could be lifted by assuming a periodicity being a multiple of a typical link length in the network. In this case, still a "cell problem" could be derived. However, the "cell problem" would typically not lead to an explicit formula and would have to be evaluated by computational means. In the framework of Γ-convergence also random networks could be considered as shown by Braides and Piatnitsky (2004). But in the random case it does not seem possible to derive an explicit homogenisation formula.

In Section 2.4, we have shown how the theory could be generalised to dynamical systems, i.e. working with balance of forces rather than energy minimisation. A direct approach considering the dynamic behaviour of spring networks has been proposed by Berezhnyy and Berlyand (2006). Considering only systems without dissipation allows the authors to transform the problem with a Laplace transformation to a minimisation problem. The approach of Berezhnyy and Berlyand (2006) as well as our approach relied on energy conservation, i.e. dissipation is not considered. With respect to "realistic" biological applications viscous effects cannot always be neglected. A rough sketch of a theory considering also viscous effects has been outlined by Alt (2002b). A rigorous treatment is, however, still an open problem.

The extension of the theory outlined in this chapter to networks which evolve in time is rather delicate, since evolution might induce dissipation (Di Carlo and Quiligotti, 2002). In this thesis, we have therefore only considered examples, in which dynamics of the mechanics are much faster than network evolution. This allowed us to consider steady mechanics on a network, which might be evolving. A possible extension to the rather general situation, where one cannot clearly distinguish between the time scales, has been addressed by Di Carlo and Quiligotti (2002) and Ambrosi and Guana (2005) in a continuum theory based on a thermodynamical framework.

As we will see in the following chapters, the concept of Γ-convergence is a very powerful tool for the derivation of macroscopic continuum models from a discrete description.

Chapter 3

Red blood cells

As a first test case of the multiscale analysis introduced in Chapter 2, we treat the mechanics of red blood cells (RBC). The investigation of RBCs has a long history in biomechanics. Since they are one of the most simple cells, they often serve as test cases. Our starting point for the analysis is the discrete model of Discher et al. (1998), refined by Li et al. (2005), describing the mechanical properties of RBCs. From this discrete model we rigorously derive its continuous counterpart in terms of an energy functional (Section 3.2). Based on this characterisation of mechanics via energy functionals corresponding stress tensors are determined.

Furthermore, the RBC serves as a test case for the development of a numerical scheme for the simulation of single cells mechanics. As a specific example, we choose an optical tweezer experiment (Hénon et al., 1999). A main issue here is the explicit consideration of the shell, i.e. coupling mechanics of a hypersurface (the membrane) with mechanics of a bulk medium (the cytosol). The model is implemented using the software library Gascoigne (Becker et al., 2007) and simulations are presented in Section 3.3.

3.1 Biological background

Red blood cells (RBC) have a relatively simple structure and therefore often serve as model systems for the development of theoretical and experimental models in biophysics. On the basis of such a simple model, more complex analysis can be developed for other cells.

Via its roughly 300 million hemoglobin molecules in the cytosol, the RBC transports oxygen from the lungs to the tissues and then transports CO_2 back. In this process, the RBC must pass through small capillaries whose inner diameters (down to 3μm) are smaller than the cell diameter (around 8μm). This requires enormous deformations of the cell with large strains (Fung, 1980). In addition, mechanics of RBCs are known to be strongly linked to diseases, such as malaria. These two issues

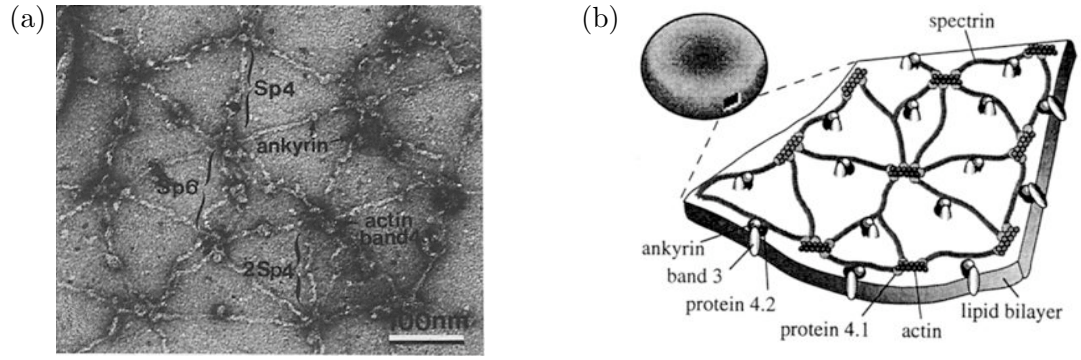

Fig. 3.1. (a) Spread membrane skeleton examined by negative-staining electron microscopy. It clearly shows the RBC's hexagonal lattice of junctional complexes. (reprinted from Liu et al., 1987, ©1987 Rockefeller University Press) (b) Schematic presentation of the organisation of the spectrin network. (reprinted from Hansen et al., 1997, ©1997 Biophysical Society)

underline, why an understanding of the mechanics of RBCs is of high interest in the life sciences (Dao et al., 2003).

Under physiological conditions, a normal human RBC assumes a biconcave discoid shape approximately 8μm in diameter. The average unstressed biconcave shape can be parametrised by

$$z = R\sqrt{1-(x^2+y^2)/R^2}[c_0 + c_1(x^2+y^2)/R^2 + c_2(x^2+y^2)^2/R^4], \qquad (3.1)$$

with $R = 3.91\mu$m, $c_0 = 0.1035805$, $c_1 = 1.001270$, and $c_2 = -0.561381$ as shown by Evans and Skalak (1980). However, a variety of agents can modify this shape systematically and reversibly (Lim et al., 2002).

RBCs are non-nucleated cells with relatively simple subcellular structures. The nucleus and other organelles that are present in RBCs during their development are expelled before and shortly after the cells are released into the circulatory system, leaving the mature cells with no internal structural components other than the membrane-associated spectrin cytoskeleton as shown in Fig. 3.1 (Boal, 2002). Basic building blocks of the spectrin network are 200nm long spectrin tetramers (edges) which crosslink the junctional complexes of actin (vertices). According to Liu et al. (1987) there are over 80% degree-6 vertices in spectrin networks extracted from healthy human RBCs, which suggest a relative regular hexagonal structure of the spectrin network (c.f. Fig. 3.1). However, recent experiments indicate that the network might be more disordered with a significant lower average vertex degree (for a discussion see Li et al., 2005). The average length of a spectrin link is 80 nm (Liu et al., 1987). Hence, the end-to-end distance of spectrin tetramers is significantly smaller than their contour length, which strongly underlines that the mechanics are due to entropic effects (see Appendix C).

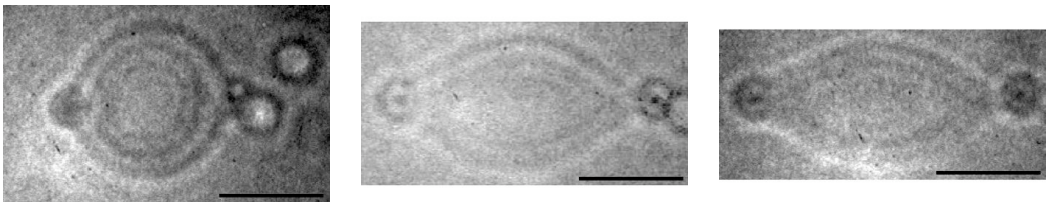

$F = 0$ pN $F = 25$ pN $F = 56$ pN

Fig. 3.2. Discotic RBC with two silica beads in diametrical position. The deformation increases with increasing force F applied on both sides. The scale-bar denotes 5μm. (reprinted from Hénon et al., 1999, ©1999 Biophysical Society)

Due to thermal fluctuations, the spectrin network is constantly rearranging. This process is strongly affected by ATP. It is usually present in the RBC and the concentration can be self-regulated by the cell (Gov and Safran, 2005). ATP can effect junctional actin complexes by inducing spectrin-actin dissociations (Gov and Safran, 2005) via the phosphorylation of the protein-41. Creation and motion of such defects allows the network to rearrange constantly. The reassociation times $\tau_{\mathrm{re}} \approx 10^{-7}$s are relatively short, which implies a small probability that spectrin filaments reassociate at nodes different from the ones they were dissociated. Otherwise they would need to surmount an energy barrier originating from steric repulsion from neighbouring filaments. On large time scales, it is postulated that the spectrin vertices of the RBC behave like a liquid as their dynamics allow a relaxation of the in-plane shear elastic energy (Li et al., 2005). However, if the deformations of RBCs are fast (much faster than the remodelling rate of the cytoskeleton), they can manifest large shear.

In particular, we concentrate in the following on optical tweezer experiments, which are quite popular (Hénon et al., 1999; Bao and Suresh, 2003; Mills et al., 2004). Using focused laser beams, optical tweezers allow to exert forces in the range of pico Newtons to dielectric microbeads and thus to control also their positions (see e.g. Neuman and Block, 2004). When the laser ray enters and exits the dielectric bead it is refracted due to different dielectric indices of the microbead and the outside medium. As a result, the ray exits in a direction different from which it originated. Since light has a momentum associated with it, this change in direction indicates that its momentum has changed. By Newton's laws the momentum of the microbead has changed correspondingly, i.e. a force has been excerted.

In a typical optical tweezer experiment one tries to pull a RBC clamped between two microbeads (Fig. 3.2, see also Fig. 3.4). Usually, the deformation rate is faster than the relaxation rate of stresses, such that relaxation can be neglected (Li et al., 2005). The experiments allow to estimate the involved mechanical moduli, because forces and deformations can be determined quite well.

	Discrete microscopic models	Continuous macroscopic models
Static models	Hansen et al. (1997) Discher et al. (1997) Boey et al. (1998) Discher et al. (1998) Li et al. (2005)	Evans and Skalak (1980) Kuzman et al. (2004) Lim et al. (2002) Mukhopadhyay et al. (2002)
Dynamic models	Noguchi and Gompper (2005)	Fung (1980) Drury and Dembo (1999, 2001) Pozrikidis (2001, 2003b,c, 2005)

Table 3.1. Different models for red blood cells found in the literature.

3.2 Modelling

Steady state deformations of RBCs are mainly determined by the membrane and the quasi-two-dimensional membrane skeleton. Models for RBC membranes, found in the literature, can be divided into two classes: macroscopic continuum models and microscopic molecular based models, i.e. discrete models. They can be further divided into solely static models, i.e. models based on energy minimisation, or dynamic models, mainly RBCs embedded in a fluid flow. References to some of the different models are summarised in Table 3.1.

We start our analysis from the popular discrete model of Discher et al. (1998), which is based on an energetic description. The model and its generalisation by Li et al. (2005) are outlined in Section 3.2.1. Continuum models based on an energetic description are reviewed in Section 3.2.2. In Section 3.2.3, we show how a static macroscopic model can be rigorously derived from a microscopic description using the results of Chapter 2. We then derive in Section 3.2.5 the corresponding stress tensors, which are the basis for a dynamic model.

Further, we compare our continuum model with models proposed in the literature, which are revised in Section 3.2.6. Finally, in Section 3.2.7 we propose a model describing optical tweezer experiments, which are one of the standard experiments to investigate the mechanical properties of RBCs and cells in general.

3.2.1 Static microscopic models

Many microscopic models go back to the work of Boey et al. (1998) and Discher et al. (1998). Based on the observations of Liu et al. (1987), Discher, Boal, and Boey propose to model the mechanics of RBCs using a quasi-two-dimensional network with hexagonal symmetry (including 12 topological defects, which are needed to cover

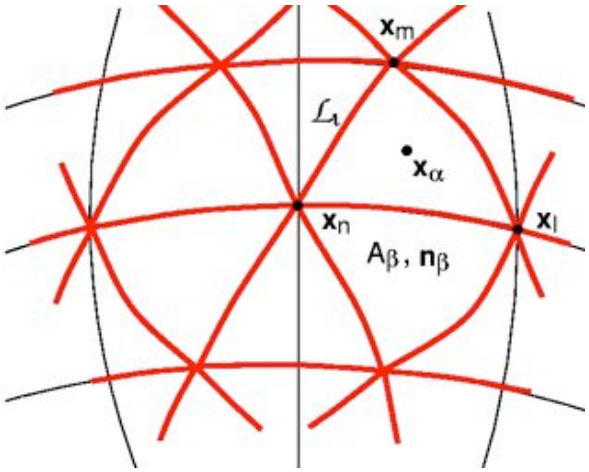

Fig. 3.3. Illustration of the network with its intrinsic quantities used in the discrete models of Discher et al. (1998) and Li et al. (2005).

a sphere with a hexagonal net). Because experiments show that the assumption of a spectrin network with a strict hexagonal symmetry might be oversimplified, the approach has been extended to more general topologies by Li et al. (2005).

The degrees of freedom of the model are the actin vertex coordinates $\{\boldsymbol{x}_n\}_{n\in 1\ldots N}$ (see Fig. 3.3). All intrinsic quantities of the model can be expressed in terms of these:

$$\begin{aligned}
\mathcal{L}_i &= |\boldsymbol{x}_m - \boldsymbol{x}_n|, \\
\mathcal{A}_\alpha &= |(\boldsymbol{x}_m - \boldsymbol{x}_l) \times (\boldsymbol{x}_n - \boldsymbol{x}_l)|/2, \\
\boldsymbol{x}_\alpha &= (\boldsymbol{x}_l + \boldsymbol{x}_m + \boldsymbol{x}_n)/3, \\
\theta_{\alpha\beta} &= \pm \arccos(\boldsymbol{n}_\alpha \cdot \boldsymbol{n}_\beta),
\end{aligned}$$

where $\mathcal{L}_i$ is the length of a spectrin link $i \in 1\ldots S$, connecting the vertex pair (m, n), $\mathcal{A}_\alpha$ is the area of the triangle $\alpha \in 1\ldots\Pi$, formed by the vertex triplets (l, m, n), and $\boldsymbol{x}_\alpha$ it's centre of mass. It is assumed that the unit normal $\boldsymbol{n}_\alpha$ points outwards the cell interior. $\theta_{\alpha\beta}$ is the spontaneous curvature angle between two adjacent triangles. Two triangles α and β are considered to be adjacent if they share a common spectrin link. The total area of the cell is given by $\mathcal{A}_{\text{total}} = \sum_\alpha \mathcal{A}_\alpha$ and the total volume by $\Omega_{\text{total}} = \frac{1}{3}\sum_\alpha (\boldsymbol{x}_\alpha \cdot \boldsymbol{n}_\alpha)\mathcal{A}_\alpha$, since the continuum divergence theorem $|\Omega| = \frac{1}{3}\int_{\partial\Omega}(\boldsymbol{x}\cdot\boldsymbol{n})d\mu$ holds.

Li et al. (2005) have invoked the physical hypothesis, that the spectrin network undergoes constant remodelling to always relax the in-plane shear elastic energy to zero at any macroscopic shape, at some slow characteristic time scale. This implies that the spectrin network has no "strict" hexagonal symmetry as proposed by Discher et al. (1998). The topologies used by Li et al. (2005) have been generated by quite elaborated Monte Carlo schemes. For each simulation of an optical tweezer experiment the topology of the network is frozen, which is reasonable since the time scale of network remodelling should be larger than the time scale of optical tweezer experiments,

which is in the order of seconds. The actual shape of the RBC is determined according to the following model.

Model 3.1 (Discher et al., 1998; Li et al., 2005)**.** *The shape of the RBC minimises the free energy:*

$$F_{\mathcal{L}_0}(\{\boldsymbol{x}_n\}) = F_{\mathcal{L}_0,\textit{in-plane}} + F_{\mathcal{L}_0,\textit{bending}} + F_{\textit{surface constraint}} + F_{\textit{volume constraint}},$$

where the different terms are explained below.

The subscript $\mathcal{L}_0$, used above, indicates the typical length scale of the discrete network. Later on, it will be replaced by ε to coincide with the notation used in Chapter 2. The non-physical energies

$$F_{\text{volume constraint}} = \frac{k_{\text{volume}} k_B T (|\Omega_{\text{cell}}| - \mathcal{V}_{\text{desired}})^2}{2\mathcal{L}_0^3 \mathcal{V}_{\text{desired}}} \tag{3.2}$$

and

$$F_{\text{surface constraint}} = \frac{k_{\text{surface}} k_B T (|\partial\Omega_{\text{cell}}| - \mathcal{A}_{\text{desired}})^2}{2\mathcal{L}_0^2 \mathcal{A}_{\text{desired}}} \tag{3.3}$$

account phenomenologically for the incompressibility of the cytosol and of the lipid bilayer.

Due to the fluid character of the lipid bilayer it cannot sustain shear stress, nevertheless it possesses a bending stiffness and a large compressional stiffness (It is often assumed to be incompressible). Here, it is assumed that these two stiffnesses can be included into the cytoskeleton since it is anchored to the lipid bilayer via anchor proteins. I.e. the effects of the lipid bilayer are assumed to be represented as coarse-grained local free energies, such that only the degrees of freedom of the cytoskeleton need to be considered. The compressional stiffness is already included in $F_{\text{surface constraint}}$ and the bending stiffness is modelled by the free energy

$$F_{\mathcal{L}_0,\text{bending}} = \sum_{\text{adjacent } \alpha,\, \beta \text{ pair}} k_{\text{bend}}[1 - \cos(\theta_{\alpha\beta} - \theta_0)],$$

in which k_{bend} is the average bending modulus of the lipid membrane and θ_0 is the spontaneous curvature. The "discrete" functional can be related to the continuous bending functional of Canham and Helfrich (Canham, 1970; Helfrich, 1973)

$$F_{\text{bending}} = \frac{\kappa}{2} \int_\Gamma (H - H_0)^2 d\mu + \kappa_g \int_\Gamma K d\mu, \tag{3.4}$$

with cell membrane Γ, bending elasticity moduli κ, κ_g, mean curvature $H = C_1 + C_2$, Gauss curvature $K = C_1 C_2$, principal curvatures C_1, C_2, and the constant H_0, which represents the spontaneous curvature.

The in-plane free energy of the bilayer membrane and the cytoskeleton, which is the dominant term in the context of large deformations (e.g. in optical tweezer experiments), is given by

$$F_{\mathcal{L}_0,\text{in-plane}} = \sum_{i \in \text{ links}} V^{\star}_{\text{WLC}}(\mathcal{L}_i) + \sum_{\alpha \in \text{ plaquettes}} \frac{C^{\star}}{\mathcal{A}^{q}_{\alpha}}, \tag{3.5}$$

where $\mathcal{L}_i$ is the length of the spectrin link i and $\mathcal{A}_\alpha$ is the area of the triangular plaquette α. $C^\star > 0$ and $q > 0$ are constants. The first term in (3.5) is the entropic energy stored in the spectrin links (see also Appendix C). It is assumed that the energy is given by the *worm-like chain* model introduced by Marko and Siggia (1995), which is widely used and tested for DNA. The energy is given by

$$V^{\star}_{\text{WLC}}(\mathcal{L}) = -\int_0^{\mathcal{L}} f_{\text{WLC}}(\xi)d\xi = \frac{k_B T \mathcal{L}^2(2\mathcal{L} - 3\mathcal{L}_{\max})}{4p(\mathcal{L} - \mathcal{L}_{\max})\mathcal{L}_{\max}},$$

where $f_{\text{WLC}}(\cdot)$ is the force versus chain length relationship given by Marko and Siggia (1995), $\mathcal{L}_{\max}$ is the maximum or contour length of the chain, $\mathcal{L}$ the instantaneous length of the chain, and p the persistence length. Considering only $V^{\star}_{\text{WLC}}$ in (3.5), the minimum of $F_{\mathcal{L}_0,\text{in-plane}}$ corresponds to a collapsed network. However, due to repulsive forces of steric interactions (i.e. entropic forces) the network does not collapse. The end-to-end distance of the spectrin filaments is much smaller than their contour length. Hence, the spectrin fibres are polymer coils with a non-negligible width leading to repulsion (see Appendix C). Therefore, the second sum is introduced into the model. It is of a phenomenological origin and accounts for steric interactions (Discher et al., 1998). In addition, it accounts for the elastic energy stored in the lipid membrane and other protein materials (Li et al., 2005). Because these terms depend only on the plaquette areas $\{\mathcal{A}_\alpha\}$ there is no shear stress contribution. Often the case $q = 1$ is adopted (Discher et al., 1998; Li et al., 2005).

The bending stiffness energy $F_{\mathcal{L}_0,\text{bending}}$ corresponds to the Canham-Helfrich energy given in (3.4) and is therefore well understood. Parameters can be obtained relatively easily from experiments (Mohandas and Evans, 1994). However, the exact nonlinear behaviour of $F_{\mathcal{L}_0,\text{in-plane}}$ is not obvious and is based more or less on a heuristic approach. With respect to exact quantitative simulations, detailed measurements on the discrete level should be undertaken in the future. A further important issue for the simulation, e.g. of optical tweezer experiments, is the choice of appropriate reference shapes. Li et al. (2005) suggest to use an energy minimum shape with respect to the energy $F_{\mathcal{L}_0,\text{bending}} + F_{\text{surface constraint}} + F_{\text{volume constraint}}$, i.e. neglecting the in-plane energy, since stresses in the membrane skeleton relax over long time scales. For more details on an appropriate choice of the reference shape see the original paper.

The major advantage of discrete models is their simplicity, which allows straight forward numerical schemes. A typical application is the determination of minimal energy configurations, i.e. steady states. Using Monte Carlo simulations the calculated shapes typically agree well with the experimentally observed shapes (Lim et al., 2002). A drawback of the approach outlined above is the introduction of the more or less non-physical energies (3.2) and (3.3), which account for the incompressibility of the volume and membrane.

In view of the derivation of a corresponding continuous macroscopic energy functional, let us rewrite (3.5) in the following way:

$$F_{\mathcal{L}_0,\text{in-plane}} = \sum_{i \in \text{ links}} \mathcal{L}_0^2 \frac{\sqrt{3}}{2} V_{\text{WLC}}\left(\frac{\mathcal{L}}{\mathcal{L}_0}\right) + \sum_{\alpha \in \text{ plaquettes}} \mathcal{L}_0^2 \frac{\sqrt{3}}{2} \frac{C}{(\mathcal{A}_\alpha/\mathcal{A}_0)^q},$$

with $\mathcal{A}_0 = \sqrt{3}/4\mathcal{L}_0^2$,

$$V_{\text{WLC}}\left(\frac{\mathcal{L}}{\mathcal{L}_0}\right) = \frac{k_B T}{2\sqrt{3} p \mathcal{L}_{\max}} \frac{(\mathcal{L}/\mathcal{L}_0)^2(2\mathcal{L}/\mathcal{L}_0 - 3\mathcal{L}_{\max}/\mathcal{L}_0)}{(\mathcal{L}/\mathcal{L}_0 - \mathcal{L}_{\max}/\mathcal{L}_0)}$$

and

$$C = \frac{2C^\star \mathcal{A}_0^q}{\sqrt{3}\mathcal{L}_0^2}.$$

Alternatively, using $\varepsilon = \mathcal{L}_0$ we recover

$$F_{\varepsilon,\text{in-plane}} = \sum_{i \in \text{ links}} \varepsilon^2 \frac{\sqrt{3}}{2} V_{\text{WLC}}\left(\frac{\mathcal{L}}{\varepsilon}\right) + \sum_{\alpha \in \text{ plaquettes}} \varepsilon^2 \frac{\sqrt{3}}{2} \frac{C}{(\frac{\mathcal{A}_\alpha}{\varepsilon^2\sqrt{3}/4})^q}, \tag{3.6}$$

which corresponds to the microscopic energies (2.2) considered in Chapter 2.

3.2.2 Static macroscopic models

Microscopic models are computationally very expensive since each fibre of the cytoskeleton must be computed. Therefore, often macroscopic continuum models are preferred.

As already stated, the bending energy of the lipid bilayer is well characterised by the Canham-Helfrich energy (Canham, 1970; Helfrich, 1973)

$$F_{\text{bending}} = \frac{\kappa}{2} \int_\Gamma (H - H_0)^2 d\mu + \kappa_g \int_\Gamma K d\mu, \tag{3.7}$$

where κ, κ_g are the moduli of bending elasticity, H is the mean curvature, K the Gauss curvature, C_1, C_2 are the principal curvatures, and the constant H_0 represents

the spontaneous curvature (see Appendix B). An extension of the Canham-Helfrich energy is the so called area difference elasticity model Boal (2002), which is a non-local model. Therefore often the Canham-Helfrich model is preferred. The network energy $F_{\text{in-plane}}$ is usually "guessed", examples of isotropic energies are:

$$\begin{aligned}
F_{\text{in-plane}}^{\text{Mukhop. et al. (2002)}} &= \frac{K}{2}\int_{\Gamma_0}(\lambda_1\lambda_2-1)^2 d\mu_0 + \frac{\mu}{2}\int_{\Gamma_0}(\frac{\lambda_1}{\lambda_2}+\frac{\lambda_2}{\lambda_1}-2)^2 d\mu_0,\\
F_{\text{in-plane}}^{\text{Kuzman et al. (2004)}} &= \frac{K}{2}\int_{\Gamma_0}(\lambda_1-\lambda_2)^2 d\mu_0 + \frac{\mu}{2}\int_{\Gamma_0}(\lambda_1+\lambda_2-2)^2 d\mu_0,\\
F_{\text{in-plane}}^{\text{Lim et al. (2002)}} &= \frac{K}{2}\int_{\Gamma_0}((\lambda_1\lambda_2-1)^2 + a_3(\lambda_1\lambda_2-1)^3 + a_4(\lambda_1\lambda_2-1)^4) d\mu_0\\
&\quad +\mu\int_{\Gamma_0}(\frac{(\lambda_1-\lambda_2)^2}{2\lambda_1\lambda_2} + b_1(\lambda_1\lambda_2-1)\frac{(\lambda_1-\lambda_2)^2}{2\lambda_1\lambda_2} + b_2\frac{(\lambda_1-\lambda_2)^4}{(2\lambda_1\lambda_2)^2}) d\mu_0,
\end{aligned}$$

where λ_1 and λ_2 are the local principal extension ratios. Furthermore, K is the stretching modulus and μ the shear modulus. The energies depend on both, the relaxed shape and on the way it is actually distributed. In order to calculate the energy we need to specify nominal relaxed shapes, which has been discussed in Section 3.2.1.

Discretising the macroscopic continuum models using a triangularisation of the RBC's membrane, discrete formulations similar to the microscopic model outlined in Section 3.2.1 are recovered. Using the principle of energy minimisation, these approaches have been successfully applied e.g. in the explanation of the different shapes observed in the experiments (Lim et al., 2002).

3.2.3 Derivation of a Macroscopic Model for $F_{\text{in-plane}}$

In the following, we derive a continuous energy functional from the microscopic model outlined in Section 3.2.1, i.e. the discrete energy of a single RBC is given by Model 3.1. However, the only "true" discrete energy is the in-plane energy $F_{\varepsilon,\text{in-plane}}$, which represents the energy contribution of the discrete spectrin cytoskeleton / membrane skeleton. We do not consider the energies $F_{\text{surface constraint}}$ and $F_{\text{volume constraint}}$ because they have no direct physical meaning, and the discretisation $F_{\varepsilon,\text{bending}}$ of the Canham-Helfrich energy, which has a natural continuous counterpart.

For the derivation of the macroscopic energies, it is necessary to introduce some regularisations of the membrane skeleton energy (3.6), since it does not fulfil Assumption 2.1 required by Theorem 2.6. For mathematical reasons, we therefore consider only approximations of the energy (3.6). Further, we restrict ourselves to periodic networks with hexagonal symmetry, which might not be the case (c.f. Section 3.1). Li et al. (2005) consider rather networks dominated by degree-6 junctions, which should be relatively "close" to networks with a solely hexagonal structure.

Assumption 3.2.

- *In-plane deformations are characterised by the discrete energy*

$$F_{\varepsilon,\text{in-plane}} = \sum_{i \in \text{ links}} \varepsilon^2 \frac{\sqrt{3}}{2} \tilde{V}_{WLC}(\mathcal{L}_i/\varepsilon) + \sum_{\alpha \in \text{ plaquettes}} \varepsilon^2 \frac{\sqrt{3}}{2} \frac{C}{(\mathcal{A}_\alpha/(\varepsilon^2\sqrt{3}/4))^q + \eta}. \quad (3.8)$$

  Here, the constant η is a regularisation term and $\tilde{V}_{WLC}(\mathcal{L}_i/\varepsilon)$ is an expansion of $V_{WLC}(\mathcal{L}_i/\varepsilon)$ of order p around 1. That is, we consider energies approximating (3.6) *given by Discher et al. (1998).*

- *We restrict ourselves to the two-dimensional tangent space of the membrane, since $F_{\varepsilon,\text{in-plane}}$ is independent of deformations perpendicular to the membrane. Let $\tilde{\boldsymbol{F}}^\Gamma \in \mathbb{R}^{2\times 2}$ with $\det \tilde{\boldsymbol{F}}^\Gamma > 0$ (orientation is preserved) be the corresponding surface deformation tensor in the continuous case.*
- *The network has a hexagonal symmetry.*

Theorem 3.3. *Let Assumption 3.2 be true. Then the discrete energy $F_{\varepsilon,\text{in-plane}}$ Γ-converges in the limit $\varepsilon \to 0$ to a continuous energy functional $F_{\text{in-plane}} = \int_\Gamma \Psi d\mu$. The energy density Ψ is given by the following homogenisation formula :*

$$\Psi = \frac{1}{2} \sum_{i=1\ldots 6} \tilde{V}_{WLC}(\tilde{\mathcal{L}}_i) + 2\frac{C}{(\tilde{\mathcal{A}}^q + \eta)}, \quad (3.9)$$

with the constant $\eta > 0$, the lengths $\tilde{\mathcal{L}}_i = |\tilde{\boldsymbol{F}}^\Gamma \cdot \boldsymbol{\xi}_i|$ of the deformed links in the "unit cell" and the areas $\tilde{\mathcal{A}} = |\det \tilde{\boldsymbol{F}}^\Gamma|$ of the triangles in the "unit cell". The displacement of the deformation is given by the two-dimensional surface deformation tensor $\tilde{\boldsymbol{F}}^\Gamma$ in the tangent space and the vectors $\boldsymbol{\xi}_i \in \mathcal{G}^{\boldsymbol{\xi}}$ with $|\boldsymbol{\xi}_i| = 1$ corresponding to the spectrin edges in the undeformed "unit cell".

For notational convenience, we consider two-dimensional deformations in the tangent space (c.f Appendix B). The corresponding deformation tensor $\tilde{\boldsymbol{F}}^\Gamma \in \mathbb{R}^{2\times 2}$ can be related to the three-dimensional surface deformation tensor $\boldsymbol{F}^\Gamma \in \mathbb{R}^{3\times 3}$. The latter is given by $\boldsymbol{F}^\Gamma \equiv \boldsymbol{F} \cdot \boldsymbol{P}_0 = \boldsymbol{P} \cdot \boldsymbol{F} \cdot \boldsymbol{P}_0$, where $\boldsymbol{P}_0 = \boldsymbol{I} - \boldsymbol{n}_0 \otimes \boldsymbol{n}_0$ is the surface projection operator with respect to the reference configuration (indicated by the subscript 0) and $\boldsymbol{P} = \boldsymbol{I} - \boldsymbol{n} \otimes \boldsymbol{n}$ the one with respect to the current configuration ($\boldsymbol{n}_0$ and $\boldsymbol{n}$ are outer unit normals of the surface).

Proof. Using $\mathcal{L}_i = \varepsilon |D_\varepsilon^{\boldsymbol{\xi}_i} \boldsymbol{\chi}|$ and $\mathcal{A}_\alpha = \varepsilon^2\sqrt{3}/4 \mathcal{A}_\varepsilon^\triangle \boldsymbol{\chi}$, the discrete energies $F_\varepsilon = F_{\varepsilon,\text{in-plane}}$ given in Assumption 3.2 are of the type (2.2). Because $\tilde{V}_{\text{WLC}}$ is a super-linear growing function and $\frac{C}{((\cdot)^q+\eta)}$ is a bounded function, Assumption 3.2 is consistent with the one of Theorem 2.6 in Chapter 2. Hence, the discrete energies $F_\varepsilon = F_{\varepsilon,\text{in-plane}}$ Γ-converge to the continuous functional $F(\boldsymbol{\chi}) = \int_\Omega \Psi(\nabla \boldsymbol{\chi}) d\mu$, where Ψ can be characterised by a minimisation problem on a growing domain, i.e. by homogenisation formula (2.5).

Since $\tilde{V}_{\mathrm{WLC}}$, $|\cdot|$, and $\frac{C}{((\cdot)^q+\eta)}$ are convex functions, we can apply Theorem 2.9. Therefore, Ψ is given by the following cell problem

$$\Psi(\boldsymbol{M}) = \frac{1}{2}\sum_{\boldsymbol{\xi}\in\mathcal{G}^\xi} f_{\mathcal{L}}\left(\boldsymbol{M}\cdot\boldsymbol{\xi}\right) + 2f_{\mathcal{A}}\left(\det\left(\boldsymbol{M}\right)\right),$$

which completes the proof. □

The energy $F_{\text{in-plane}}$ given in (3.9) is generally not isotropic with respect to surface deformations (see below). However, the proposed macroscopic energies, reviewed in Section 3.2.2, depend only on invariants of the surface deformation tensor and hence are isotropic. Since the symmetry of the network is only roughly hexagonal, an isotropic dependence seems to be more realistic. But our ansatz requires the assumption of hexagonal symmetry for the sake of a homogenisation formula, therfore we will need to account heuristically for the imperfect symmetry by some type of averaging. A rigorous approach is an open problem.

For the derivation of Theorem 3.3, we work with expansions instead with V_{WLC} itself. This is only due to technical reasons and might be lifted as outlined in Discussion 2.6. So far, a rigorous treatment of the interchange of expansions and Γ-convergence is an open problem. Similarly, the regularisation term η in Assumption 3.2 has been introduced for mathematical reasons. A rigorous extension of the proof to the limit $\eta \to 0$ is an open mathematical problem, which should be investigated in the future. For the rest of this chapter let us assume $\eta = 0$.

3.2.4 Characterisation of $F_{\text{in-plane}}$ using invariants of $\tilde{\boldsymbol{F}}^\Gamma$

Throughout the literature different invariants are used in the context of hyperelastic materials. Usually, the invariants are expressed in terms of principal stretches λ_1 and λ_2. λ_1^2 and λ_2^2 are the eigenvalues of the tensor $(\tilde{\boldsymbol{F}}^\Gamma)^T\cdot\tilde{\boldsymbol{F}}^\Gamma$, alternatively of the tensor $\tilde{\boldsymbol{F}}^\Gamma\cdot(\tilde{\boldsymbol{F}}^\Gamma)^T$. We work with the following invariants, similar to the ones proposed by Skalak et al. (1973):

$$\begin{aligned} I_1 &= J^\Gamma - 1 \\ &= \lambda_1\lambda_2 - 1 \end{aligned} \qquad \text{and} \qquad \begin{aligned} I_2 &= \operatorname{tr}\left(\tilde{\boldsymbol{F}}^\Gamma\cdot(\tilde{\boldsymbol{F}}^\Gamma)^T\right) - 2 \\ &= \lambda_1^2+\lambda_2^2-2, \end{aligned} \tag{3.10}$$

which appear naturally in the derivation. Here, $J^\Gamma = \det\tilde{\boldsymbol{F}}^\Gamma > 0$ (We consider only deformations preserving the orientation.) is the surface Jacobian. These invariants are normalised such that they are zero if no stretches are present, i.e. $\lambda_i = 1$. For a comparison of the invariants with the ones found in the literature see Table 3.2.

Let us try to relate the invariants (3.10) to the corresponding three-dimensional surface deformation tensor $\boldsymbol{F}^\Gamma \equiv \boldsymbol{F}\cdot\boldsymbol{P}_0 \in \mathbb{R}^{3\times3}$ with $\det\boldsymbol{F} > 0$ (orientation is preserved). The eigenvalues of the symmetric tensor ${\boldsymbol{F}^\Gamma}^T\cdot\boldsymbol{F}^\Gamma$ are λ_1^2, λ_2^2, and zero, where the former eigenvalues are the eigenvalues of $(\tilde{\boldsymbol{F}}^\Gamma)^T\cdot\tilde{\boldsymbol{F}}^\Gamma$. We therefore have

Skalak et al. (1973)	$I_1^\star = (I_2+1)^2 - 1$	$I_2^\star = I_1$
Evans and Skalak (1980)	$\alpha = \sqrt{I_2+1}$	$\beta = \dfrac{I_1+2}{2\sqrt{I_2+1}} - 1$
Barthés-Biesel and Rallison (1981)	$\Lambda_1^S = \dfrac{1}{2}\ln I_2 + 1$	$\Lambda_2^S = \dfrac{1}{2} I_1$
McDonald (1996)	$I_1^V = \dfrac{1}{I_2+1} + I_1 + 2$	$I_2^V = I_1 + I_2 + 3$

Table 3.2. Invariants of $\tilde{\boldsymbol{F}}^\Gamma$ used in the literature

$I_2 = \mathrm{tr}\,(\boldsymbol{F}^\Gamma \cdot \boldsymbol{F}^{\Gamma T}) - 2$, but $I_1 \neq \det \boldsymbol{F} = 0$. Let $\boldsymbol{t}_1$ and $\boldsymbol{t}_2$ be two orthogonal vectors in the tangent space of the surface. Then, the "Jacobian" J^Γ of the surface deformation is given by $J^\Gamma = \sqrt{\det \boldsymbol{g}}$ with the metric tensor

$$(\boldsymbol{g})_{ij} = (\boldsymbol{F}^\Gamma \cdot \boldsymbol{t}_i)^T \cdot (\boldsymbol{F}^\Gamma \cdot \boldsymbol{t}_j) \quad \text{with } i,j \in \{1,2\} \tag{3.11}$$

(c.f. Appendix B), rather than by $\det \boldsymbol{F}^\Gamma$. We have

$$I_1 \;= J^\Gamma - 1 = \sqrt{\det \boldsymbol{g}} - 1 \qquad \text{and} \qquad I_2 \;= \mathrm{tr}\,(\boldsymbol{F}^\Gamma \cdot (\boldsymbol{F}^\Gamma)^T) - 2. \tag{3.12}$$

For notational convenience, we work however in the following with the $\tilde{\boldsymbol{F}}^\Gamma$, rather than $\boldsymbol{F}^\Gamma$.

The derivation of formula (3.9) is restricted to expansions of V_{WLC} for mathematical reasons (Assumption 3.2). Let us consider Taylor expansions in terms of $\tilde{\mathcal{L}}_i^2$ around 1, i.e. around the length in the reference configuration. A further Taylor expansion of formula (3.9) with respect to $\mathcal{A}_i$ around 1, i.e. around the areas in the reference configuration, yields

$$\begin{aligned}\Psi = \frac{1}{2}\sum_{i=1\ldots6}\Bigg[&\tilde{V}(1) + \frac{\tilde{V}'(1)}{2}\left(\mathcal{L}_i^2 - 1\right) + \frac{-\tilde{V}'(1) + \tilde{V}''(1)}{4}\left(\mathcal{L}_i^2 - 1\right)^2 \\ &+ \frac{3\tilde{V}'(1) - 3\tilde{V}''(1) + \tilde{V}'''(1)}{8}\left(\mathcal{L}_i^2 - 1\right)^3\Bigg] \\ &+2C - 2qC\left(\mathcal{A} - 1\right) + q(q+1)C\left(\mathcal{A} - 1\right)^2 \\ &- \frac{q(q+1)(q+2)C}{3}\left(\mathcal{A} - 1\right)^3 + \text{h.o.t.},\end{aligned} \tag{3.13}$$

where primes denote derivatives and $\tilde{V} = \tilde{V}_{\mathrm{WLC}}$ for notational convenience.

Now let us determine $(\mathcal{L}_i^2 - 1)^k$ and $(\mathcal{A}_i - 1)^k$ in terms of the invariants I_1 and I_2. By definition of the invariants (3.10), we have for the "area" terms in the Taylor expansion (3.13)

$$\mathcal{A} - 1 = I_1. \tag{3.14}$$

The tensor $(\tilde{\boldsymbol{F}}^{\Gamma})^T \cdot \tilde{\boldsymbol{F}}^{\Gamma}$ is symmetric and positive definite, it can be diagonalised, i.e.

$$(\tilde{\boldsymbol{F}}^{\Gamma})^T \cdot \tilde{\boldsymbol{F}}^{\Gamma} = \boldsymbol{\Phi}^T \cdot \boldsymbol{\Lambda} \cdot \boldsymbol{\Phi}$$

with $\boldsymbol{\Lambda} = \mathrm{diag}(1{+}1/2(I_2{+}\sqrt{I_2^2+4I_2-4I_1^2-8I_1}), 1{+}1/2(I_2{-}\sqrt{I_2^2+4I_2-4I_1^2-8I_1}))$ and a rotation $\boldsymbol{\Phi}$ around an angle ϕ, where I_1 and I_2 are the invariants given in (3.10). Using $\mathcal{L}_i(\lambda_1,\lambda_2,\phi) = |\tilde{\boldsymbol{F}}^{\Gamma} \cdot \boldsymbol{\xi}_i| = \sqrt{\boldsymbol{\xi}_i^T \cdot (\tilde{\boldsymbol{F}}^{\Gamma})^T \cdot \tilde{\boldsymbol{F}}^{\Gamma} \cdot \boldsymbol{\xi}_i}$ we obtain

$$\mathcal{L}_i^2(\lambda_1,\lambda_2,\phi) - 1^2 = (\boldsymbol{\Phi}\cdot\boldsymbol{\xi}_i)^T \cdot (\boldsymbol{\Lambda}-\boldsymbol{I}) \cdot (\boldsymbol{\Phi}\cdot\boldsymbol{\xi}_i),$$

which implies for the "length" terms in the Taylor expansion (3.13):

$$\begin{aligned}
\sum_{i=1\ldots6} \left(\mathcal{L}_i^2 - 1\right) &= 3I_2, \\
\sum_{i=1\ldots6} \left(\mathcal{L}_i^2 - 1\right)^2 &= \frac{3}{4}(4I_2 - 8I_1 + 3I_2^2 - 4I_1^2), \\
\sum_{i=1\ldots6} \left(\mathcal{L}_i^2 - 1\right)^3 &= \frac{3}{8}I_2(12I_2 + 5I_2^2 - 12I_1^2 - 24I_1) \\
&\quad + \frac{3}{16}(I_2^2 + 4I_2 - 4I_1^2 - 8I_1)^{3/2}\cos(6\phi).
\end{aligned}$$

The hexagonal structure of the network is reflected in the terms $(\mathcal{L}_i^2-1)^j$ with $j>2$. These depend not only on the invariants, but also on $\cos(6\phi)$, or rather on ϕ. As mentioned above, an energy incorporating explicitly the hexagonal symmetry might not be appropriate and some averaging is necessary. Here, we propose the arithmetic average over the angle ϕ:

$$\Psi^\star(I_1,I_2) = \int_0^{2\pi} \Psi(I_1,I_2,\phi)d\phi. \tag{3.15}$$

This might be interpreted as a geometry which has not a strictly hexagonal symmetry, but consists locally of slightly rotated reference cells.

The averaging (3.15) allows us to drop the dependence on the angle ϕ in (3.13) and therefore yields

$$\begin{aligned}
\Psi^\star = \;& 3\tilde{V}(1) + \frac{3\tilde{V}'(1)}{4}I_2 + \frac{3(-\tilde{V}'(1)+\tilde{V}''(1))}{32}(4I_2 - 8I_1 + 3I_2^2 - 4I_1^2) \\
&+ \frac{3(3\tilde{V}'(1) - 3\tilde{V}''(1) + \tilde{V}'''(1))}{128}I_2(12I_2 + 5I_2^2 - 12I_1^2 - 24I_1) \\
&+ 2C - 2qCI_1 + q(q+1)CI_1^2 - \frac{q(q+1)(q+2)C}{3}I_1^3 + \text{h.o.t.}.
\end{aligned} \tag{3.16}$$

Since the averaging (3.15) is quite heuristic, some better approaches might exist and alternatives should be investigated (see Discussion 2.6).

In principal, the isotropic averaged energy $\Psi^\star$ can be compared with the different energies proposed in the literature, i.e. we can calculate the coefficients of the proposed energies from microscopic models rather than "guessing" them. However, the

comparison is rather difficult as a wide variety of invariants is used in the literature, c.f. Table 3.2.

For the rest of this chapter, we adopt the following assumptions:

Assumption 3.4.

- *The membrane skeleton is initially not stressed.*
- *We restrict ourselves to Taylor expansions of* (3.9) *up to order* $(\mathcal{L}_i^2 - 1)^2$*, and accordingly* $(\mathcal{A} - 1)^2$*.*
- *Without restriction of generality, we consider normalised energies such that* $E = 0$ *if* $I_1 = I_2 = 0$*.*

The assumption of an initially unstressed membrane skeleton might not hold true. Prestress is an important concept in biology (Ingber, 2003) and also might play a role in RBCs (Boey et al., 1998). However, this assumptions enables us to determine the constant C, as we will see below. The restriction to Taylor expansions of (3.9) of order $(\mathcal{L}_i^2 - 1)^2$ and accordingly $(\mathcal{A} - 1)^2$ implies that the hexagonal structure of the membrane skeleton is not reflected in the energy Ψ since we drop terms including the angle ϕ. Therefore, it is not necessary to average energies as in (3.16) and we have $\Psi = \Psi^\star$. Considering higher terms might not be appropriate due to the relatively rude microscopic model. The restriction to normalised energies in Assumption 3.4 is only for notational convenience.

For the moment, let us consider a deformation consisting only of compression, or alternatively dilatation, to determine the constant C using the assumption of an initially unstressed network. In the case of compression alone we have $I_2 = 2I_1$. Considering only linear terms in I_1 and I_2 of (3.16), we obtain

$$\Psi = \frac{3\tilde{V}'(1)}{4} I_2 - 2qCI_1 + h.o.t.. \tag{3.17}$$

Because we have assumed that the network is initially unstressed, the energy (3.17) should be at a minimum and hence all linear terms should vanish. We therefore have

$$C = \frac{3\tilde{V}'(1)}{4q}. \tag{3.18}$$

The same result is obtained, if we work with the direct characterisation (3.13) rather than with the invariants I_1 and I_2. Using Assumption 3.4 and expression (3.18), we can rewrite (3.16) in the following way

$$\begin{aligned} \Psi = {} & \frac{3}{16}(3\tilde{V}'(1) + \tilde{V}''(1))(I_2 - 2I_1) + \frac{9}{64}(-\tilde{V}'(1) + \tilde{V}''(1))I_2^2 \\ & + \frac{3}{16}((4q+5)\tilde{V}'(1) - \tilde{V}''(1))I_1^2. \end{aligned} \tag{3.19}$$

Let us first consider the case $q \neq 1$. Simple algebraic manipulations of expression (3.19) yield:

$$\Psi = \frac{\mu}{2}(I_2 - 2I_1) - \frac{3(K - \mu(q+1))}{8(q-1)} I_2^2 + \frac{3K - (5+q)\mu}{2(q-1)} I_1^2$$

with

$$\mu = \frac{3(3\tilde{V}'(1) + \tilde{V}''(1))}{8},$$
$$K = \frac{3((1+2q)\tilde{V}'(1) + \tilde{V}''(1))}{4}.$$

The suggestive notation used here implies indeed that K is the modulus of rigidity and μ the modulus of hydrostatic compression. This can be verified by calculating the corresponding stress tensor of the energy density Ψ (c.f. Section 3.2.5) and considering infinitesimal deformations, i.e. its linearisation. In the case $q = 1$, we obtain

$$\Psi = \frac{\mu}{2}(I_2 + 2I_1^2 - 2I_1) + \beta(I_2^2 - 4I_1^2)$$

with

$$\mu = \frac{K}{2} = \frac{3(3\tilde{V}'(1) + \tilde{V}''(1))}{8},$$
$$\beta = \frac{9(-\tilde{V}'(1) + \tilde{V}''(1))}{64},$$

which agree with the expressions above. The case $q = 1$ implies $\mu = \frac{K}{2}$, which agrees quite well with the experimental results found by Lenormand et al. (2001), see also Table 3.6. The constant β has no direct interpretation in a linear theory.

For the rest of this chapter, we restrict ourselves to the case $q = 1$.

Corollary 3.5. *Adopting Assumption 3.4 and choosing $q = 1$, Theorem 3.3 implies the following characterisation for the membrane skeleton in terms of invariants of the deformation tensor:*

$$\Psi = \frac{\mu}{2}(I_2 + 2I_1^2 - 2I_1) + \beta(I_2^2 - 4I_1^2) \tag{3.20}$$

with μ and β as given above. The constant μ is the modulus of hydrostatic compression and the constant β determines the nonlinear behaviour (It does not influence the linear part of the mechanics.).

Li et al. (2005) propose the following parameters for the worm-like chain model V_{WLC} (see Section 3.2.1):

$$\mathcal{L}_0 = 75.0\mathrm{nm}, \qquad \mathcal{L}_{\max} = 237.6\mathrm{nm},$$
$$p = 7.5\mathrm{nm}, \qquad T = 300K.$$

Together with the Boltzmann constant $k_B = 1.38 \cdot 10^{-23} \frac{J}{K}$, we obtain from (3.2.4)

$$\mu = \frac{K}{2} = 8.30 \cdot 10^{-6} \frac{N}{m},$$
$$\beta = 0.25 \cdot 10^{-6} \frac{N}{m},$$

which agrees well with the results of Li et al. (2005), who are using a similar approach.

3.2.5 Variational derivation of a model for red blood cells

The models considered above are all based on an energetic description. It is a static approach and actual shapes of RBCs are determined by energy minimisation. In the following, we derive corresponding forces / stress tensors using variational methods as explained in Section 2.4. From these we can easily determine minimal energy configurations using the principle of virtual work (see Section 2.4.1). At the same time the derivation of the forces allows us to describe the RBC in the framework of momentum balance. Given an appropriate stress tensor $\boldsymbol{\sigma}_{\text{cytosol}}$ for the cytosol, the mechanics of the RBC are completely determined within a dynamic theory.

Assumption 3.6.

- *The membrane of the RBC is considered as a two-dimensional hypersurface in* $\mathbb{R}^3$.
- *The bending energy of the membrane is given by the Canham-Helfrich energy* (3.7).
- *The in-plane energy of the membrane-bound spectrin skeleton is given by the homogenised energy* (3.9) *with* $\eta = 0$, *i.e. energy* (3.20).

In microscopic descriptions of the RBCs (Section 3.2.1), the energies corresponding to bending and in-plane deformations are not coupled. Therefore, also the corresponding forces are not coupled. The momentum balance on the cell membrane, which is a two-dimensional hypersurface, reads:

$$(\boldsymbol{\sigma}_{\text{cytosol}} - \boldsymbol{\sigma}_{\text{out}}) \cdot \boldsymbol{n} = \boldsymbol{N} + \boldsymbol{T},$$

where $\boldsymbol{\sigma}_{\text{cytosol}}$ is the stress tensor of the cytosol, $\boldsymbol{\sigma}_{\text{out}}$ the stress tensor of the ambient medium, $\boldsymbol{n}$ the outward unit normal vector, $\boldsymbol{N}$ the force due to resistance to bending, and $\boldsymbol{T}$ the force due to in-plane stresses. The membrane forces $\boldsymbol{N}$ and $\boldsymbol{T}$ are determined by the steepest decent of the L^2- gradient of the membrane energy (Section 2.4).

Resistance to bending

Since the energies are decoupled, we can neglect the in-plane energy, i.e. in-plane stresses, for the moment. Normal forces $\boldsymbol{N}$ are uniquely due to the resistance of the membrane to bending. Let the bending energy of the membrane be given by the Canham-Helfrich energy (Canham, 1970; Helfrich, 1973)

$$F_{\text{bending}} = \frac{\kappa}{2}\int_\Gamma (H - H_0)^2 d\mu + \kappa_g \int_\Gamma K d\mu, \tag{3.21}$$

where Γ is the membrane, κ, κ_g are the moduli of bending elasticity, $H = C_1 + C_2$ is the mean curvature, $K = C_1 C_2$ is the Gauss curvature, C_i are the principal curvatures, and the constant H_0 is the spontaneous curvature. The Gauss-Bonnet theorem (Willmore, 1993) states that the integral over the Gauss curvature depends only on the topology and not on the shape of Γ. Because we allow only variations over a fixed topology, the integral $\int_\Gamma K d\mu$ is constant and can therefore be neglected.

Under the assumption that the normal force $\boldsymbol{N}$ is determined by the steepest decent of the L^2-gradient of F_{bending}, we have

$$\begin{aligned}\int_\Gamma \boldsymbol{N}\cdot(\boldsymbol{n}\phi)d\mu &= -\left\langle F'_{\text{bending}}, \phi\right\rangle \\ &= -\frac{d}{d\varepsilon}\frac{\kappa}{2}\int_{\Gamma_\varepsilon}(H_\varepsilon - H_0)^2 d\mu_\varepsilon\Big|_{\varepsilon=0},\end{aligned} \tag{3.22}$$

with $H_\varepsilon = H(\boldsymbol{X}_\varepsilon)$, $d\mu_\varepsilon = d\mu(\boldsymbol{X}_\varepsilon)$, and $\boldsymbol{X}_\varepsilon = \boldsymbol{X} + \varepsilon\boldsymbol{n}\phi$. Here, $\boldsymbol{n}$ is the outer unit normal of the surface Γ and $\phi \in C^\infty(\Gamma;\mathbb{R})$ is an arbitrary test function. It is sufficient to consider only variations $\varepsilon\boldsymbol{n}\phi$, since a variation in the normal direction completely describes the evolution of the interface. Following Willmore (1993, Chapter 7.4, Attention, Willmore uses a different definition of mean curvature, i.e. $H_{\text{Willmore}} = -H/2$), the variation of the mean curvature is given by

$$\begin{aligned}\frac{d}{d\varepsilon}H_\varepsilon\Big|_{\varepsilon=0} &= -\Delta^\Gamma\phi - \phi|\nabla^\Gamma\boldsymbol{n}|^2 \\ &= -\Delta^\Gamma\phi - \phi(H^2 - 2K)\end{aligned}$$

and the variation of the integration measure is given by

$$\frac{d}{d\varepsilon}d\mu_\varepsilon\Big|_{\varepsilon=0} = \phi H d\mu.$$

Here, ∇^Γ is the surface gradient and Δ^Γ is the Laplace-Beltrami operator (surface Laplace). We have $\nabla^\Gamma = \boldsymbol{P}\cdot\nabla$, where $\boldsymbol{P} = \boldsymbol{I} - \boldsymbol{n}\otimes\boldsymbol{n}$ is the projection operator to the surface (see Appendix B). Hence, we recover from expression (3.22)

$$\begin{aligned}\int_\Gamma \boldsymbol{N}\cdot(\boldsymbol{n}\phi)d\mu &= \frac{\kappa}{2}\int_\Gamma [2(H - H_0)(\Delta^\Gamma\phi + \phi(H^2 - 2K)) - (H - H_0)^2\phi H]d\mu \\ &= \kappa\int_\Gamma [\Delta^\Gamma H + (H - H_0)(H^2 - 2K) - \frac{1}{2}(H - H_0)^2 H]\phi d\mu,\end{aligned}$$

where we have used the product rule and Green's theorem for surfaces (see Appendix B). Thus, we can determine the equivalent strong formulation of $\boldsymbol{N}$:

$$\boldsymbol{N} = \kappa(\Delta^\Gamma H + (H - H_0)(H^2 - 2K) - \frac{1}{2}(H - H_0)^2 H)\boldsymbol{n}. \tag{3.23}$$

Setting the material speed $\boldsymbol{v}$ proportional to $\boldsymbol{N}$ and considering the case $H_0 = 0$, the so-called Willmore flow (see Section 3.3.1) is obtained (Willmore, 1993; Deckelnick et al., 2005). Considering a constant surface energy density instead of (3.21), a force proportional to the mean curvature is recovered, i.e. $\boldsymbol{N} \sim H\boldsymbol{n}$. Such a force typically describes interface tensions and is quite often used modelling capsules and cells (Pozrikidis, 2003a).

Resistance to in-plane deformations

As derived in Section 3.2.3, the energy corresponding to the resistance to in-plane deformations is given by (considering $\eta = 0$)

$$F_{\text{in-plane}} = \int_{\Gamma_0} \left[\frac{1}{2} \sum_{i=1\ldots6} \tilde{V}_{\text{WLC}}(\mathcal{L}_i) + 2\frac{C}{\mathcal{A}^q} \right] d\mu_0 \tag{3.24}$$

with the initial shape Γ_0 of the membrane. As in Section 3.2.3, let us consider for notational convenience deformations $\tilde{\boldsymbol{F}}^\Gamma \in \mathbb{R}^{2\times2}$ in the tangent space with $\det \tilde{\boldsymbol{F}}^\Gamma > 0$ (the orientation is preserved). Hence, we have $\mathcal{L}_i = |\tilde{\boldsymbol{F}}^\Gamma \cdot \boldsymbol{\xi}_i|$ and $\mathcal{A} = \det \tilde{\boldsymbol{F}}^\Gamma$.

Considering variations of the form $\boldsymbol{x}_\varepsilon(\boldsymbol{X}) = \boldsymbol{x}(\boldsymbol{X}) + \varepsilon\boldsymbol{\phi}(\boldsymbol{X})$ with test functions $\boldsymbol{\phi} \in C^\infty(\Gamma_0; \mathbb{R}^2)$, we obtain

$$\begin{aligned} \frac{d}{d\varepsilon}\tilde{\boldsymbol{F}}^\Gamma\Big|_{\varepsilon=0} &= \nabla_0^\Gamma \boldsymbol{\phi} \\ &= \left(\nabla^\Gamma \boldsymbol{\phi}\right) \cdot \tilde{\boldsymbol{F}}^\Gamma. \end{aligned}$$

Hence, the variations of the lengths $\mathcal{L}_i = \sqrt{(\tilde{\boldsymbol{F}}^\Gamma \cdot \boldsymbol{\xi}_i)^T \cdot (\tilde{\boldsymbol{F}}^\Gamma \cdot \boldsymbol{\xi}_i)}$ read:

$$\begin{aligned} \frac{d\mathcal{L}_i}{d\varepsilon}\Big|_{\varepsilon=0} &= \frac{1}{2\mathcal{L}_i}\boldsymbol{\xi}_i^T \cdot \left(\frac{d(\tilde{\boldsymbol{F}}^\Gamma)^T \cdot \tilde{\boldsymbol{F}}^\Gamma}{d\varepsilon}\Big|_{\varepsilon=0} \right) \cdot \boldsymbol{\xi}_i \\ &= \frac{1}{2\mathcal{L}_i}\boldsymbol{\xi}_i^T \cdot (\tilde{\boldsymbol{F}}^\Gamma)^T \cdot ((\nabla^\Gamma \boldsymbol{\phi})^T + (\nabla^\Gamma \boldsymbol{\phi})) \cdot \tilde{\boldsymbol{F}}^\Gamma \cdot \boldsymbol{\xi}_i, \end{aligned}$$

where $\boldsymbol{\xi}_i$ is the vector of the ith link in the undeformed unit cell. Similarly, we obtain

$$\begin{aligned} \frac{d\mathcal{A}}{d\varepsilon}\Big|_{\varepsilon=0} &= \det \tilde{\boldsymbol{F}}^\Gamma \operatorname{tr}\left(\left(\tilde{\boldsymbol{F}}^\Gamma\right)^{-1} \cdot \frac{d\tilde{\boldsymbol{F}}^\Gamma}{d\varepsilon}\Big|_{\varepsilon=0} \right) \\ &= \mathcal{A} \operatorname{tr}(\nabla^\Gamma \boldsymbol{\phi}), \end{aligned}$$

where we have used the identity $\frac{\partial}{\partial\varepsilon}\det\tilde{\boldsymbol{F}}^{\Gamma} = \det(\tilde{\boldsymbol{F}}^{\Gamma})\,\mathrm{tr}\,((\tilde{\boldsymbol{F}}^{\Gamma})^{-1}\cdot\frac{\partial}{\partial\varepsilon}\tilde{\boldsymbol{F}}^{\Gamma})$ based on Jacobi's formula. Hence, it follows

$$\begin{aligned}\int_{\Gamma}\boldsymbol{T}\cdot\boldsymbol{\phi}d\mu &= -\left\langle F'_{\text{in-plane}},\phi\right\rangle = -\frac{d}{d\varepsilon}F_{\text{in-plane}}\Big|_{\varepsilon=0}\\ &= -\int_{\Gamma_0}\Bigg[\frac{1}{2}\sum_{i=1\dots6}\frac{1}{2\mathcal{L}_i}\frac{\partial\tilde{V}_{\text{WLC}}(\mathcal{L}_i)}{\partial\mathcal{L}_i}\hat{\boldsymbol{\xi}}_i\cdot((\nabla^{\Gamma}\boldsymbol{\phi})+(\nabla^{\Gamma}\boldsymbol{\phi})^T)\cdot\hat{\boldsymbol{\xi}}_i\\ &\qquad - 2q\frac{C}{\mathcal{A}^{q+1}}\mathcal{A}\,\mathrm{tr}\,(\nabla^{\Gamma}\boldsymbol{\phi})\Bigg]d\mu_0,\end{aligned}$$

where $\hat{\boldsymbol{\xi}}_i = \tilde{\boldsymbol{F}}^{\Gamma}\cdot\boldsymbol{\xi}_i$ is the vector of the ith link after the deformation $\tilde{\boldsymbol{F}}^{\Gamma}$. Integration by parts yields

$$\int_{\Gamma}\boldsymbol{T}\cdot\boldsymbol{\phi}d\mu = \int_{\Gamma_0}\nabla^{\Gamma}\cdot\left(\frac{1}{2\mathcal{A}}\sum_{i=1\dots6}\frac{1}{\mathcal{L}_i}\frac{\partial\tilde{V}_{\text{WLC}}(\mathcal{L}_i)}{\partial\mathcal{L}_i}\hat{\boldsymbol{\xi}}_i\otimes\hat{\boldsymbol{\xi}}_i - 2q\frac{C}{\mathcal{A}^{q+1}}\boldsymbol{I}\right)\cdot\boldsymbol{\phi}\mathcal{A}d\mu_0, \quad (3.25)$$

where boundary terms do not need to be considered since Γ_0, and accordingly Γ, is a closed surface. The corresponding strong formulation of this weak characterisation is given by

$$\boldsymbol{T} = \nabla^{\Gamma}\cdot\boldsymbol{\tau} \quad (3.26)$$

with the so-called surface stress tensor

$$\boldsymbol{\tau} = \frac{1}{2\mathcal{A}}\sum_{i=1\dots6}\frac{1}{\mathcal{L}_i}\frac{\partial V_{\text{WLC}}(\mathcal{L}_i)}{\partial\mathcal{L}_i}\hat{\boldsymbol{\xi}}_i\otimes\hat{\boldsymbol{\xi}}_i - 2q\frac{C}{\mathcal{A}^{q+1}}\boldsymbol{I}. \quad (3.27)$$

The stress tensor $\boldsymbol{\tau}$ as given in (3.27) reflects the hexagonal symmetry of the underlying network. As explained in Section 3.2.3, an isotropic energy, and accordingly an isotropic stress tensor, seems to be more appropriate due to the stochastic nature of the membrane skeleton. Isotropic energies can be characterised by the invariants of the surface deformation tensor $\boldsymbol{F}^{\Gamma}$ alone. Considering the invariants I_1 and I_2 given in (3.10), or rather (3.12), the variational approach yields

$$\boldsymbol{\tau} = \frac{2}{1+I_1}\frac{\partial\Psi}{\partial I_2}\boldsymbol{F}^{\Gamma}\cdot\boldsymbol{F}^{\Gamma T} + \frac{\partial\Psi}{\partial I_1}\boldsymbol{P}, \quad (3.28)$$

where $\boldsymbol{P} = \boldsymbol{I} - \boldsymbol{n}\otimes\boldsymbol{n}$ is the surface projection operator and $\Psi \equiv \Psi(I_1, I_2)$ the energy of the membrane skeleton in terms of the invariants I_1 and I_2. In the following we work with this characterisation of $\boldsymbol{\tau}$ rather than with expression (3.27).

Proposition 3.7. *Adopting Assumption 3.6, the mechanics of the RBC's membrane are given by the following balance law across the membrane*

$$(\boldsymbol{\sigma}_{cytosol} - \boldsymbol{\sigma}_{out}) \cdot \boldsymbol{n} = \nabla^\Gamma \cdot \boldsymbol{\tau} + \kappa(\Delta^\Gamma H + (H - H_0)(H^2 - 2K) - \frac{1}{2}(H - H_0)^2 H)\boldsymbol{n}.$$

Here, $\boldsymbol{\sigma}_{cytosol/outs}$ are the stress tensors of the RBC's cytosol and the outside medium. Furthermore, $\boldsymbol{\tau}$ is the in-plane stress tensor given by (3.28)*, i.e.*

$$\boldsymbol{\tau} = \frac{2}{1 + I_1} \frac{\partial \Psi}{\partial I_2} \boldsymbol{F}^\Gamma \cdot \boldsymbol{F}^{\Gamma T} + \frac{\partial \Psi}{\partial I_1} \boldsymbol{P},$$

with surface deformation tensor $\boldsymbol{F}^\Gamma$ and invariants I_1, I_2 given in (3.12)*.*

Typically, it is assumed that the cytosol is well described by the incompressible Stokes equation, i.e. $\boldsymbol{\sigma}_{\text{cytosol}} = \boldsymbol{\sigma}_{\text{Stokes}}$. The outside medium is also often considered to be a Stokes flow. In this case the evolution of the RBC and the surrounding flow can be simulated efficiently using boundary element methods (Pozrikidis, 2003a). If the RBC is not immersed in a flow, e.g. as in optical tweezer experiments, the outside flow can be neglected. It is assumed that the surrounding fluid has a vanishing viscosity and hence $\boldsymbol{\sigma}_{\text{out}} = -p_{\text{out}} \boldsymbol{I}$, where p_{out} is a constant pressure.

In the next section, we compare the model for the RBC's mechanics given in Proposition 3.7 with other popular continuum models in the literature (see also Table 3.1). Then in Section 3.2.7, we finally specify the model which we will use for the simulation of optical tweezer experiments.

3.2.6 Other dynamic models

Discrete models

As in the static case, discrete models are quite popular when considering dynamics (Noguchi and Gompper, 2005). Such models can not only explain the observed shapes, but e.g. also the behaviour of RBCs in flow. Starting from the discrete microscopic model outlined in Section 3.2.1, the derivation of the corresponding forces is analogous to the concept in the continuum case (Section 3.2.5). Working in a discrete setting, i.e. in a finite dimensional setting, the algebra simplifies substantially. Another advantage is the more or less straight forward computational implementation of these models.

A drawback of discrete approaches is that typically each discrete computational object does not correspond to a physical object, e.g. a spectrin vertex. The number of physical objects is typically very large such that due to a limitation of computational resources some coarse graining is necessary. Therefore, one often prefers to work with a continuum model at first hand and to discretise it appropriately.

Fully three-dimensional models

Dao et al. (2003) and Mills et al. (2004) model the membrane as a thin elastic body with a small, but finite, thickness. This allows them to use standard numerical code developed for three-dimensional solid mechanics. It is however questionable if a three-dimensional solid is an appropriate description of the lipid bilayer, which is best described as a two-dimensional hypersurface (Boal, 2002).

Thin shell models

From three-dimensional elastic models with a small thickness (e.g. Dao et al., 2003; Mills et al., 2004) so-called shell models can be derived. These are models which describe curved, thin-walled structures within a two-dimensional theory (Libai and Simmonds, 1996). Hence, these theories consider mechanics of a hypersurface embedded in a three-dimensional space, similar to our approach. The equations of shell mechanics including the corresponding constitutive equations can be derived directly from a three-dimensional description. However, the more usual approach is to start from the balance of momentum for thin shells and postulate appropriate constitutive relations. Following the work of Pozrikidis (2001), the balance of linear momentum on the cell membrane reads

$$(\boldsymbol{\sigma}_{\text{cytosol}} - \boldsymbol{\sigma}_{\text{out}}) \cdot \boldsymbol{n} = \nabla^{\Gamma} \cdot (\boldsymbol{\tau} + \boldsymbol{n}\boldsymbol{q}), \tag{3.29}$$

where inertial effects of the cell membrane are neglected. Here, $\boldsymbol{\sigma}_{\text{cytosol/out}}$ are the bulk stress tensors and $\boldsymbol{\tau}$ is the in-plane stress tensor. The transverse shear tension in the direction of the unit normal vector $\boldsymbol{n}$ exerted on the membrane that is normal to the tangential unit vector $\boldsymbol{b}$ is given by $\boldsymbol{q} \cdot \boldsymbol{b}$. An investigation of the torque balance across the membrane yields the following relationships

$$\begin{aligned} \boldsymbol{q} &= \boldsymbol{P} \cdot \left(\nabla^{\Gamma} \cdot \boldsymbol{m}\right), \\ \boldsymbol{\tau} - \boldsymbol{\tau}^{T} &= \boldsymbol{B} \cdot \boldsymbol{m}^{T} - \boldsymbol{m} \cdot \boldsymbol{B}, \end{aligned} \tag{3.30}$$

where $\boldsymbol{P} = \boldsymbol{I} - \boldsymbol{n} \otimes \boldsymbol{n}$ is the tangential projection operator, $\boldsymbol{B} = \nabla^{\Gamma}\boldsymbol{n}$ is the Cartesian mean curvature tensor, $\boldsymbol{m}$ the bending moment tensor, and ∇^{Γ} the surface gradient (see Appendix B). Note, that the stress tensors used within this work are the transposed of the ones considered in the work of Pozrikidis (2001). For a description of cells within shell theory, typically the following constitutive relations are used (Pozrikidis, 2003a):

$$\begin{aligned} \boldsymbol{\tau} &= \frac{2}{1 + I_1} \frac{\partial \Psi}{\partial I_2} \boldsymbol{F}^{\Gamma} \cdot \boldsymbol{F}^{\Gamma T} + \frac{\partial \Psi}{\partial I_1} \boldsymbol{P} \\ \boldsymbol{m} &= \kappa (H - H_0) \boldsymbol{P}, \end{aligned}$$

where the first expression agrees with (3.28), H is the mean curvature, and H_0 is a reference curvature similar to the Canham-Helfrich energy (3.7). Furthermore, $\boldsymbol{F}^{\Gamma}$ is the surface deformation tensor and I_1, I_2 are the invariants given in (3.12).

The description of in-plane stresses agrees with our approach. However, the description of the bending resistance of the lipid bilayer differs significantly. The derivation of the forces considered in our approach is based on the experimentally quite well verified Canham-Helfrich energy (Canham, 1970; Helfrich, 1973). On the other hand, the postulated constitutive relation for the bending moment tensor $\boldsymbol{m}$ as given by Pozrikidis (2001) can be related to the Canham-Helfrich energy only in the case of an incompressible one-dimensional membrane in a two-dimensional setting. A relation to a corresponding energy in three dimensions, i.e. considering a two-dimensional hypersurface, is an open problem.

3.2.7 Modelling optical tweezer experiments

In Section 3.2.5, we have derived a continuum model for the evolution of RBCs. For a validation, we investigate a typical RBC experiment, namely an optical tweezer experiment as illustrated in Fig. 3.4 (Hénon et al., 1999; Dao et al., 2003; Li et al., 2005; Mills et al., 2004).

With respect to modelling, we adopt the following assumptions:

Assumption 3.8.

- *Thermodynamical effects (e.g. membrane undulations) are neglected.*
- *The time scale of the experiment is fast compared to relaxation times.*
- *Linear momentum and masses are conserved.*
- *Inertial effects can be neglected, i.e. we consider a quasi-steady situation.*
- *The mechanics of the RBC membrane are modelled as in Proposition 3.7.*
- *In-plane stress-strain relationships are given by Corollary 3.5.*
- *The membrane is incompressible.*
- *The cytosol is described by the static incompressible Stokes equation.*
- *The outside medium is described by a constant external pressure p_{out}.*
- *The optical tweezers are rigid and prescribe the normal direction of deformation, alternatively the normal force.*
- *The reference state/initial state is the biconcave shape* (3.1) *determined by Evans and Skalak (1980). Due to constant remodelling of the spectrin network, it should be in a state with zero shear energy (Li et al., 2005).*

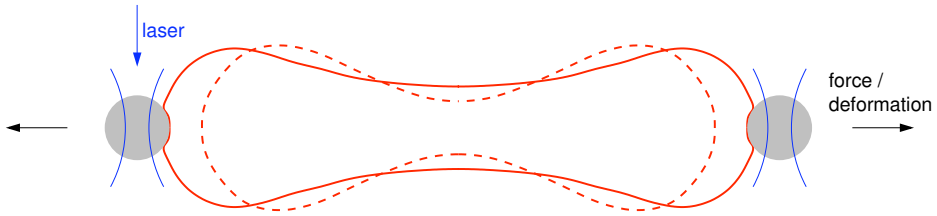

Fig. 3.4. Illustration of a typical optical tweezer experiment.

Then using Assumptions 3.8 the model for an optical tweezer experiment reads:

Model 3.9. *Using Assumption 3.8, the full three-dimensional model of an optical tweezer experiments reads (for some fixed time T):*

$$\frac{d\boldsymbol{u}}{dt} = \boldsymbol{v} \qquad \text{in } \Omega_{cell}(t) \times [0,T),$$

bulk mechanics

$$\begin{aligned} 0 &= \nabla \cdot \boldsymbol{\sigma}_{cytosol} && \text{in } \Omega_{cell}(t) \times [0,T), \\ 0 &= \nabla \cdot \boldsymbol{v} && \text{in } \Omega_{cell}(t) \times [0,T), \end{aligned} \tag{3.31}$$

surface mechanics

$$\begin{aligned} (\boldsymbol{\sigma}_{cytosol} + p_{out}\boldsymbol{I}) \cdot \boldsymbol{n} &= \boldsymbol{T} + \boldsymbol{N} && \text{on } \partial\Omega_{cell}(t) \setminus \partial\Omega_{tweezer}(t) \times [0,T), \\ 0 &= J^{\Gamma} - 1 && \text{on } \partial\Omega_{cell}(t) \times [0,T), \\ \boldsymbol{t} \cdot \boldsymbol{\sigma}_{cytosol} \cdot \boldsymbol{n} &= -\boldsymbol{t} \cdot \nabla^{\Gamma} \cdot \boldsymbol{\tau} && \text{on } \partial\Omega_{tweezer}(t) \times [0,T), \end{aligned}$$

and in the case of a prescribed bead deformation *with normal speed V_n*

$$V_n = \boldsymbol{n} \cdot \boldsymbol{v} \qquad \text{on } \partial\Omega_{tweezer}(t) \times [0,T),$$

alternatively in the case of a prescribed bead force f_{force}

$$\boldsymbol{n} \cdot (\boldsymbol{\sigma}_{cytosol} - p_{out}\boldsymbol{I}) \cdot \boldsymbol{n} = f_{force} \qquad \text{on } \partial\Omega_{tweezer}(t) \times [0,T).$$

The evolution of $\Omega_{cell}(t)$ is given by the speed on the boundary. We use the following constitutive relations

$$\begin{aligned} \boldsymbol{\sigma}_{cytosol} &= -p\boldsymbol{I} + \eta\left(\nabla\boldsymbol{v} + (\nabla\boldsymbol{v})^T\right), \\ \boldsymbol{T} &= \nabla^{\Gamma} \cdot \boldsymbol{\tau}, \\ \boldsymbol{N} &= \kappa(\Delta^{\Gamma} H + (H - H_0)(H^2 - 2K) - \frac{1}{2}(H - H_0)^2 H)\boldsymbol{n}, \\ \boldsymbol{\tau} &= -q\boldsymbol{P} + \frac{2}{1 + I_1}\frac{\partial \Psi}{\partial I_2}\boldsymbol{F}^{\Gamma} \cdot \boldsymbol{F}^{\Gamma T} + \frac{\partial \Psi}{\partial I_1}\boldsymbol{P}. \end{aligned}$$

The energy density Ψ is given by Corollary 3.5, i.e.

$$\Psi = \frac{\mu}{2}(I_2 + 2I_1^2 - 2I_1) + \beta(I_2^2 - 4I_1^2)$$

with $I_1 = J^{\Gamma} - 1$ and $I_2 = \operatorname{tr}(\boldsymbol{F}^{\Gamma} \cdot \boldsymbol{F}^{\Gamma T}) - 2$ (c.f. the definition given in (3.12)).

Here, $\boldsymbol{u}$ is the material displacement, i.e. the current position of a particle at position $\boldsymbol{X}$ in the reference configuration is given by $\boldsymbol{x} = \boldsymbol{X} + \boldsymbol{u}(\boldsymbol{X})$. Further, $\boldsymbol{F}^\Gamma$ denotes the surface deformation gradient, J^Γ the surface Jacobian given by (3.12), $\boldsymbol{v}$ the material speeds, p the volume pressure, q the surface pressure, $\boldsymbol{n}$ the outer unit normal of the cell membrane, and $\boldsymbol{t}$ an arbitrary tangential unit vector. In addition, H is the mean curvature, K the Gauss curvature, ∇^Γ the surface gradient, Δ^Γ the Laplace-Beltrami operator, and $\boldsymbol{P}$ the surface projection operator (see Appendix A). Parameters of Model 3.9 are the constant outside pressure p_{out}, the cytosol viscosity η, the modulus of bending rigidity κ, the surface shear modulus μ, and the constant β determining the nonlinear surface elasticity.

The incompressibility of the membrane, i.e. $0 = J^\Gamma - 1$ in (3.31), is equivalent to the condition

$$0 = \nabla^\Gamma \cdot \boldsymbol{v} \qquad \text{on } \partial\Omega_{\text{cell}}(t) \times [0, T), \tag{3.32}$$

which can be easily checked by differentiation of J^Γ with respect to time. For a computational implementation the condition in (3.31) is, however, more suitable since errors do not accumulate in time. This might be the case considering the incompressibility condition (3.32).

In Model 3.9, the bulk mechanics are given by the stationary incompressible Stokes equation. These are second order equations which are quite well studied from an analytical as well as numerical point of view. The tangential component of the surface mechanics is a typical example of a hyperelastic material. It is also a second order equation, which is quite well understood. On the other hand, the normal mechanics of the lipid bilayer involve fourth order derivatives and the structure is "nearly identical" to Willmore flow (see Section 3.3.1). From a numerical as well as analytical point of view only a few studies have been devoted to Willmore flows. Due to the coupling of the different models, especially the coupling of surface (two-dimensional models on a hypersurface) with bulk mechanics (three-dimensional models), investigations of Model 3.9 are quite challenging.

Here, we restrict ourselves to an investigation from a numerical point of view. Therefore, let us adopt the following assumption. A rigorous analytical treatment is an open problem which is far beyond the scope of this thesis.

Assumption 3.10. *For the rest of this chapter, we assume that solutions of Model 3.9 exist and are sufficiently regular.*

The optical tweezer experiment serve not only as a test case (benchmark problem) for the model derived here, but also as a test case for the development of appropriate numerical schemes for single cell mechanics. In the next section, we present appropriate numerical schemes, as well as some simulations.

3.3 Simulations

Let us first review some typical computational studies of RBCs: Simulations of microscopic models so far include shape minimisation (Lim et al., 2002; Li et al., 2005), optical tweezer experiments (Li et al., 2005) and micropipette aspiration experiments (Discher et al., 1998). Only recently, the dynamics of "discrete" cells suspended in flow have been investigated (Noguchi and Gompper, 2005). Being interested in steady-states, the deformed state is usually obtained by energy minimisation using Monte Carlo methods. Otherwise an integration of the Newtonian equations of motion is used.

Simulations of continuum models include optical tweezer experiments (Dao et al., 2003; Mills et al., 2004) and the evolution of RBC cells in flow (Pozrikidis, 2001, 2003a,b, 2005). Only in the latter case a two-dimensional continuum theory has been used for the description of membrane mechanics. However, as discussed in Section 3.2.6, the formulation of Pozrikidis does not coincide with the variation of the Canham-Helfrich energy, which is probably more realistic and is investigated here. Using shell theory, i.e. considering explicitly the coupling of mechanics of a hypersurface with bulk material, boundary element methods are typically used. Since boundary element methods require the Stokes equation for the fluid, they are restricted only to a small class of problems.

Here, we use a Lagrangian approach for the simulation of optical tweezer experiments. The approach is very general and can be extended easily to more complex equations. For the simulations, we use the software library Gascoigne (Becker et al., 2007), which allows a quite flexible handling. All visualisation is done with the visualisation toolkits VisuSimple (Becker et al., 2007) and ParaView (Kitware Inc.).

Our approach is similar to the one of Drury and Dembo (1999, 2001), who considered neutrophils. However, it is not restricted to two dimensions and allows implicit time stepping schemes. Here, we need to consider a three-dimensional setup because the initial rotational symmetry of the RBC is not conserved during an optical tweezer experiment. Further, our approach to membrane mechanics is based on the Canham-Helfrich energy, which suggest the use of implicit schemes. A variational formulation of the Canham-Helfrich energy corresponds to Willmore flows, which involve spatial derivatives of fourth order. Explicit time stepping schemes would imply very small time steps (Clarenz et al., 2004), thus implicit schemes are the method of choice.

As a test case for the validation of the derived models and numerical schemes, we consider a typical optical tweezer experiment (Hénon et al., 1999; Dao et al., 2003; Li et al., 2005; Mills et al., 2004). The main difficulty in the simulation of cell mechanics is the calculation of the membrane forces given by (3.23). As already stated, this problem is equivalent to Willmore flows, a typical problem of curvature dependent interface motion governed by geometric partial differential equations. Therefore, we first study some problems related to curvature dependent interface motion. These

are used to develop appropriate numerical schemes and to perform some basic tests, investigating convergence properties of the applied schemes.

3.3.1 Interface motion

Curvature dependent interface motion governed by geometric partial differential equations is a wide research topic in mathematical as well as in numerical analysis. A main idea from a computational point of view is the characterisation of the curvature via the Laplace-Beltrami operator of the interface parametrisation. This characterisation allows a weak formulation in a straight forward way, and simplifies in some cases the equations. For a general overview on interface motion, we would like to refer to the review of Deckelnick et al. (2005).

Often (apart from level set approaches) it is enough to consider all involved quantities on the hypersurface alone, i.e. the grid underlying the computations is also a hypersurface. But as we are interested in a coupling of membrane mechanics with bulk mechanics, we also need to incorporate the bulk medium enclosed by the membrane. Therefore, we consider the problem of curvature dependent interface motion as a bulk problem (formulated in the Lagrangian coordinate system). Solutions of the geometric partial differential equations on the interface are implicitly coupled with Laplace-equations in the interior (bulk problems) via weak Dirichlet boundary conditions.

The approach taken here is validated by the investigation of some well studied test cases: mean curvature flow (Dziuk, 1991), surface diffusion (Bänsch et al., 2005), and Willmore flow (Clarenz et al., 2004).

Strong formulation of the problem

To be more precise, we consider the following models:

Model 3.11. *An embedding of two-dimensional surface evolution determined by mean curvature flow, surface diffusion, or Willmore flow in a three-dimensional space is given by the* bulk equation

$$\begin{aligned} \frac{d\boldsymbol{u}}{dt} &= \boldsymbol{v} && \text{in } \Omega(t)\times[0,T), \\ 0 &= \Delta \boldsymbol{v} && \text{in } \Omega(t)\times[0,T) \end{aligned}$$

with Dirichlet boundary conditions

$$\begin{aligned} \boldsymbol{v} &= \boldsymbol{v}^{\Gamma}_{\textit{mean curv / surf diff /Willmore}} && \text{on } \partial\Omega(t)\times[0,T), \\ \boldsymbol{Y} &= -\Delta^{\Gamma}\boldsymbol{x} && \text{on } \partial\Omega(t)\times[0,T). \end{aligned}$$

for some fixed time $T > 0$. The evolution $\boldsymbol{v}^\Gamma$ of the surface is given by

$$\boldsymbol{v}^\Gamma_{mean\ curv} = -\boldsymbol{Y} = -H\boldsymbol{n} \qquad \text{on } \partial\Omega(t) \times [0,T)$$

in the case of mean curvature *flow, by*

$$\boldsymbol{v}^\Gamma_{surf\ diff} = (\Delta^\Gamma H)\boldsymbol{n} \qquad \text{on } \partial\Omega(t) \times [0,T)$$

in the case of surface diffusion*, and by*

$$\boldsymbol{v}^\Gamma_{Willmore} = \left(\Delta^\Gamma H + H\left(\frac{1}{2}H^2 - 2K\right)\right)\boldsymbol{n} \qquad \text{on } \partial\Omega(t) \times [0,T)$$

in the case of Willmore flow*.*

Here, $\boldsymbol{u}$ is the material displacement, i.e. the current position of a particle at position $\boldsymbol{X}$ in the reference configuration is given by $\boldsymbol{x} = \boldsymbol{\chi}(\boldsymbol{X}) = \boldsymbol{X} + \boldsymbol{u}(\boldsymbol{X})$, and $\boldsymbol{v}$ is the material speed. In addition, $\boldsymbol{Y}$ is the mean curvature vector, $H = C_1 + C_2 = \boldsymbol{Y} \cdot \boldsymbol{n}$ is the mean curvature (C_1 and C_2 are the principal curvatures), $K = C_1C_2 = \frac{1}{2}H^2 - \frac{1}{2}|\nabla^\Gamma \boldsymbol{n}|^2$ is the Gauss curvature, ∇^Γ the tangential gradient, Δ^Γ is the Laplace-Beltrami operator, and $\boldsymbol{n}$ the outer unit normal to $\partial\Omega(t)$. In the case of mean curvature flow, the introduction of the mean curvature vector $\boldsymbol{Y}$ as an additional variable is of course not necessary.

Weak formulation of the problem

Finite element methods are based on weak formulations of the considered problems. Let us therefore derive the corresponding weak formulations of Model 3.11. In the case of mean curvature flow, the weak formulation reads:

Model 3.12. *The componentwise weak formulation of Model 3.11 considering* mean curvature flow *is given by the* bulk part

$$\begin{aligned} \int_{\Omega(t)} \phi \frac{d\boldsymbol{u}}{dt} d\mu &= \int_{\Omega(t)} \phi \boldsymbol{v} d\mu, \\ 0 &= \int_{\Omega(t)} (\nabla \boldsymbol{v}) \cdot (\nabla \phi) d\mu \end{aligned}$$

with $\boldsymbol{v} = \boldsymbol{v}^\Gamma$ on $\partial\Omega(t)$ in the weak sense and the surface part

$$\int_{\partial\Omega(t)} \phi^\Gamma \boldsymbol{v} d\mu = -\int_{\partial\Omega(t)} (\nabla^\Gamma \boldsymbol{x}^\Gamma) \cdot (\nabla^\Gamma \phi^\Gamma) d\mu,$$

where $\phi \in C_0^\infty(\Omega(t); \mathbb{R})$ and $\phi^\Gamma \in C^\infty(\partial\Omega(t); \mathbb{R})$ are arbitrary test functions.

Multiplying the equations in Model 3.11 with test functions $\phi \in C_0^\infty(\Omega(t);\mathbb{R})$ and $\phi^\Gamma \in C^\infty(\partial\Omega(t);\mathbb{R})$, the weak formulation 3.12 is recovered after partial integration. Since $\partial\Omega$ is closed, no additional boundary conditions for $\boldsymbol{v}^\Gamma$ have to be considered.

The derivation of a corresponding weak formulation for surface diffusion is outlined in the work of Bänsch et al. (2005). For an appropriate weak formulation with respect to numerical implementation the mean curvature H and the normal surface speed V_n^Γ have to be introduced as additional variables:

Model 3.13. *The componentwise weak formulation of Model 3.11 in the case of* surface diffusion *is given by the* bulk part

$$\begin{aligned}\int_{\Omega(t)} \phi \frac{d\boldsymbol{u}}{dt} d\mu &= \int_{\Omega(t)} \phi \boldsymbol{v} d\mu,\\ 0 &= \int_{\Omega(t)} (\nabla \boldsymbol{v}) \cdot (\nabla \phi) d\mu\end{aligned}$$

with $\boldsymbol{v} = \boldsymbol{v}^\Gamma$ *on* $\partial\Omega(t)$ *in the weak sense and the* surface part

$$\begin{aligned}\int_{\partial\Omega(t)} \phi^\Gamma \boldsymbol{v}^\Gamma d\mu &= \int_{\partial\Omega(t)} \phi^\Gamma V_n^\Gamma \boldsymbol{n} d\mu,\\ \int_{\partial\Omega(t)} \phi^\Gamma \boldsymbol{Y} d\mu &= \int_{\partial\Omega(t)} (\nabla^\Gamma \boldsymbol{x}) \cdot (\nabla^\Gamma \phi^\Gamma) d\mu,\\ \int_{\partial\Omega(t)} \phi^\Gamma H d\mu &= \int_{\partial\Omega(t)} \phi^\Gamma \boldsymbol{Y} \cdot \boldsymbol{n} d\mu,\\ \int_{\partial\Omega(t)} \phi^\Gamma V_n^\Gamma d\mu &= -\int_{\partial\Omega(t)} (\nabla^\Gamma H) \cdot (\nabla^\Gamma \phi^\Gamma) d\mu,\end{aligned}$$

where $\phi \in C_0^\infty(\Omega(t);\mathbb{R})$ *and* $\phi^\Gamma \in C^\infty(\partial\Omega(t);\mathbb{R})$ *are arbitrary test functions.*

The weak formulation of Model 3.11 considering Willmore flow is given by

Model 3.14. *The componentwise weak formulation of Model 3.11 in the case of* Willmore flow *is given by the* bulk part

$$\begin{aligned}\int_{\Omega(t)} \phi \frac{d\boldsymbol{u}}{dt} d\mu &= \int_{\Omega(t)} \phi \boldsymbol{v} d\mu,\\ 0 &= \int_{\Omega(t)} (\nabla \boldsymbol{v}) \cdot (\nabla \phi) d\mu\end{aligned}$$

with $\boldsymbol{v} = \boldsymbol{v}^\Gamma$ *on* $\partial\Omega(t)$ *in the weak sense and the* surface part

$$\begin{aligned}\int_{\partial\Omega(t)} \phi^\Gamma \boldsymbol{v}^\Gamma d\mu &= \int_{\partial\Omega(t)} -\frac{1}{2}|\boldsymbol{Y}|^2 (\nabla^\Gamma \boldsymbol{x}) \cdot (\nabla^\Gamma \phi^\Gamma) + (\nabla^\Gamma \boldsymbol{Y}) \cdot (\nabla^\Gamma \phi^\Gamma)\\ &\qquad -2\boldsymbol{n} \otimes \boldsymbol{n} \cdot (\nabla^\Gamma \boldsymbol{Y}) \cdot (\nabla \phi^\Gamma) d\mu,\\ \int_{\partial\Omega(t)} \phi^\Gamma \boldsymbol{Y} d\mu &= \int_{\partial\Omega(t)} (\nabla^\Gamma \boldsymbol{x}) \cdot (\nabla^\Gamma \phi^\Gamma) d\mu,\end{aligned}$$

where $\phi \in C_0^\infty(\Omega(t);\mathbb{R})$ *and* $\phi^\Gamma \in C^\infty(\partial\Omega(t);\mathbb{R})$ *are arbitrary test functions.*

Eulerian Coordinate System	Lagrangian Coordinate system
$\int_{\Omega(t)} \dots d\mu$	$\int_{\Omega(0)} \dots J d\mu_0$
$\int_{\partial\Omega(t)} \dots d\mu$	$\int_{\partial\Omega(0)} \dots J^\Gamma d\mu_0$
$\nabla\phi$	$(\nabla_0\phi)\cdot\boldsymbol{F}^{-1} = (\boldsymbol{F}^{-T}\cdot\nabla_0)\phi$
$\nabla^\Gamma\phi = ((\boldsymbol{I}-\boldsymbol{n}\otimes\boldsymbol{n})\cdot\nabla_0)\phi$	$\nabla^\Gamma\phi = ((\boldsymbol{I}-\boldsymbol{n}\otimes\boldsymbol{n})\cdot\boldsymbol{F}^{-T}\cdot\nabla_0)\phi$

Table 3.3. Differential and integral operators appearing in Model 3.12 - 3.14 in Lagrangian and Eulerian formulations. Here, $J = \det\boldsymbol{F}$ is the Jacobian of the deformation tensor $\boldsymbol{F} = \nabla_0\boldsymbol{x}$, $J^\Gamma = \sqrt{\det\boldsymbol{g}}$ is the surface Jacobian with the metric tensor $\boldsymbol{g}$ (see expression (3.11) or Appendix B), and $\boldsymbol{n}$ the outer unit normal of $\Omega(t)$.

Multiplying the equations in Model 3.11 with test functions $\phi \in C_0^\infty(\Omega(t);\mathbb{R})$ and $\phi^\Gamma \in C^\infty(\partial\Omega(t);\mathbb{R})$, the weak formulation 3.14 is recovered after partial integration, except the equation determining $\boldsymbol{v}^\Gamma_{\text{Willmore}}$. The derivation of the latter is less straight forward, because the corresponding strong formulation 3.11 is not given in a divergence form. One possible derivation of the weak formulation starting directly from the variation of $\int_\Gamma H^2 d\mu$ has been proposed by Rusu (2005). Here, we would like to refer to Section 3.3.2, where we outline a weak formulation of the normal forces $\boldsymbol{N} = \kappa(\Delta^\Gamma H + (H-H_0)(H^2-2K) - \frac{1}{2}(H-H_0)^2 H)\boldsymbol{n}$. The normal forces $\boldsymbol{N}$ are derived in Section 3.2.5 from a variation of the more general surface energy $\int(H-H_0)^2 d\mu$ with resting curvature H_0. Choosing $H_0 = 0$, the Willmore flow $\boldsymbol{v}_{\text{Willmore}}$ is recovered. Note that the weak formulation of Willmore flows in Model 3.14 involves only first order spatial derivatives, whereas the original strong formulation (Model 3.11) is a fourth order problem. With respect to computations this is a significant simplification.

Numerical implementation

The strong and weak formulations of the surface evolution given above are all based on the Eulerian description. The Lagrangian description is, however, more appropriate with respect to implementation using standard finite element packages. Considering the Lagrangian coordinate system instead of the Eulerian for Models 3.12-3.14, differential and integral operators have to be transformed appropriately. The corresponding transformations can be derived by successive applications of the chain rule and are shown in Table 3.3.

The definition of the tangential surface gradient ∇^Γ given in Table 3.3 is equivalent to the following definition, which is probably more common: given a local parametrisation $\boldsymbol{x}(u_1,u_2)$ of the surface, the tangential gradient can be formulated using the

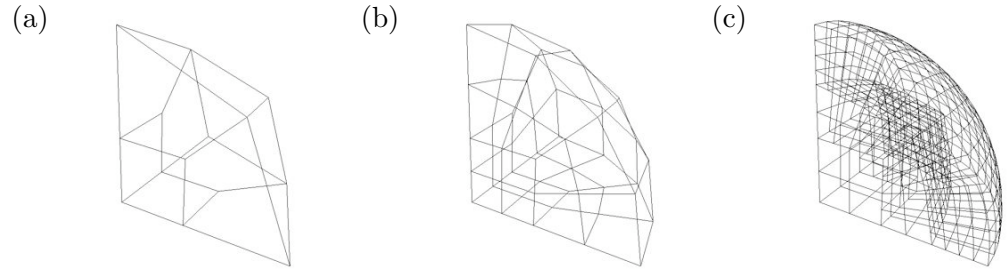

Fig. 3.5. Typical discretisations: (a) initial discretisation; (b) discretisation with one global refinement (12 surface quadrilaterals); (c) discretisation with one global refinement and 2 refinements in the vicinity of the surface (192 surface quadrilaterals)

metric tensor $\boldsymbol{g}$ (see see expression (3.11) or Appendix B)

$$\nabla^\Gamma \phi(u_1, u_2) = \sum_{i,j=1}^{2} \left(g^{ij} \frac{\partial \phi\,(u_1, u_2)}{\partial u_i} \frac{\partial \boldsymbol{x}\,(u_1, u_2)}{\partial u_j} \right),$$

where g_{ij} and g^{ij} are the components of the metric tensor and the inverse of the metric tensor, respectively.

Using the transformations to the Lagrangian coordinate system, Models 3.12-3.14 have been implemented using the finite element library Gascoigne (Becker et al., 2007). The software package Gascoigne does not allow to distinguish between surface and bulk variables. Hence, variables defined only on the boundary have to be extended appropriately. Here, we have chosen an extension by Laplace's equation. The surface speed $\boldsymbol{v}^\Gamma$ and the bulk speed $\boldsymbol{v}$ are considered as one variable, which allows a direct implicit coupling. Since the weak formulations 3.12 - 3.14 of Model 3.11 involve only first order derivatives, we use tri-linear finite elements in the bulk part and accordingly bi-linear finite elements on the surface. The evolution in time is discretised using implicit schemes, e.g. Euler or Fractional-Theta schemes. Using Newton's method, the resulting nonlinear systems are solved. Corresponding linearisations are solved with a GMRES preconditioner and a multigrid method.

The finite element toolkit Gascoigne offers the possibility of local mesh refinement, which allows a reduction of computational effort. In the case of surface evolution problems, the extension to the interior is only an auxiliary problem and does not require a high accuracy. We therefore always choose an adaptive discretisation refined in the vicinity of the surface (see Fig. 3.5). Most of the applications we consider have reflection symmetries with respect to the coordinate planes. This allows us to consider only one eighth of the object, reducing the computational effort further.

Considering the case of surface diffusion in Model 3.13 some stabilisation with respect to the tangential directions is necessary. Surface diffusion flow is not as gentle as its corresponding mean curvature flow, such that severe mesh-distortions might occur (Bänsch et al., 2005). Here, we choose an ad-hoc stabilisation by a pseudo-mechanical problem in the tangential direction (similar to the membrane mechanics

N_{surface}	$\lvert R_n(T) - R_\infty(T)\rvert$	EOC
48	0.002530	
192	0.000580	2.1250
768	0.000096	2.5949
3072	0.000025	1.9411

Table 3.4. Experimental order of convergence for mean curvature flow of a sphere with initial radius $R(0) = 1.0$ using a Crank-Nicolson scheme with $\delta t = 10^{-4}$ and n subsequent local mesh refinements in the vincinity of the surface, corresponding to N_{surface} surface quadrilaterals. Radii are compared at time $T = 0.1$ with the explicit solution (3.33), i.e. $R_\infty(T) = \sqrt{0.6}$.

of the RBC). Instead of the speed $\boldsymbol{v}^\Gamma_{\text{surf diff}}$ given in Model 3.11, we considered the stabilised counterpart given by

$$\boldsymbol{v}^\Gamma_{\text{surf diff}} = (\Delta^\Gamma H)\boldsymbol{n} + \mu_{\text{stab}} \nabla^\Gamma \cdot (\boldsymbol{F}^\Gamma \cdot \boldsymbol{F}^{\Gamma T}),$$

where $\boldsymbol{F}^\Gamma$ is the surface gradient. However, the influence of the stabilisation has not been investigated systematically.

Numerical tests and convergence

As a first test, we investigate the evolution of a sphere under mean curvature flow (Model 3.11 with $\boldsymbol{v}^\Gamma_{\text{mean curv}}$), which is a second order problem. Given a sphere with radius $R(t)$ the mean curvature is given by $H = 1/R(t) + 1/R(t)$. The evolution of the sphere is therefore determined by the following ordinary differential equation

$$\frac{\partial R(t)}{\partial t} = -\frac{2}{R(t)},$$

which can be solved explicitly

$$R(t) = \sqrt{R(0) - 4t}. \tag{3.33}$$

Comparing the explicit solution (3.33) with computations, the convergence rates can be determined. To do so, we have simulated the evolution of the radii using computations with $N_{\text{surface}} = 48 - 3072$ ($3 \cdot 4^2 - 3 \cdot 4^5$) roughly equally spaced quadrilaterals discretising the surface. Convergence properties of simulations using a Crank-Nicolson time stepping scheme are shown in Table 3.4. With respect to convergence properties, it is sufficient to consider the surface discretisation alone, since the bulk part is only an auxiliary problem, which does not influence the evolution of the surface. The experimental order of convergence is roughly two, which coincides with the theoretically expected rate of convergence (Deckelnick et al., 2005).

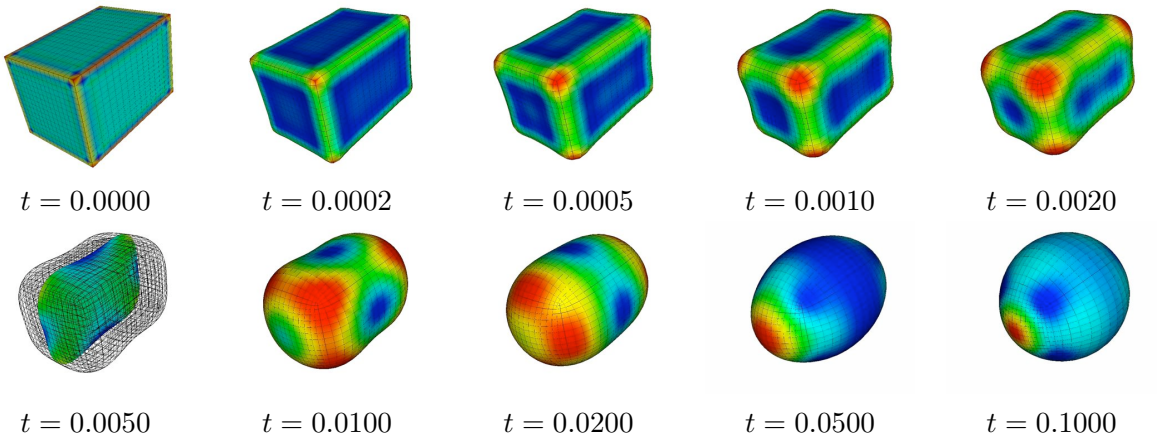

Fig. 3.6. Different time steps of a box under surface diffusion flow. The colouring indicates the magnitude of the mean curvature, but it is not normalised. For the simulations we have chosen an implicit Euler scheme with $\delta t = 10^{-4}$ and a stabilisation via an additional mechanical problem with $\mu_{\text{stab}} = 10$.

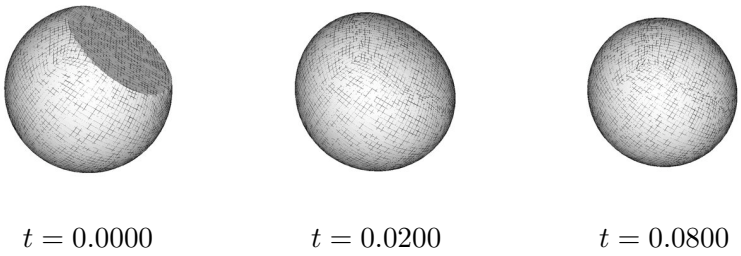

Fig. 3.7. Different time steps of a Willmore flow for an initially spherical surface with a flattened part. The solution has been computed using an implicit Euler scheme with $\delta t = 10^{-4}$.

As test cases of fourth order problems, we have simulated two typical problems: the evolution of a box under surface diffusion (see Fig. 3.6, Bänsch et al., 2005) and the surface restoration of a sphere with a flattened part (see Fig. 3.7, Clarenz et al., 2004). The latter problem is a slight modification of the example considered by Clarenz et al. (2004): here we allow the whole sphere to evolve and not only the flattened part. The results are similar, as the sphere is a stationary solution of the Willmore flow (Willmore, 1993). Our simulations of both test cases agree well with the results obtained by Bänsch et al. (2005) and Clarenz et al. (2004).

For a more systematic investigation of Willmore flows, we have further simulated the evolution of an ellipsoid using different mesh qualities (see Fig. 3.8). To be more precise, we have considered the ellipsoid given by

$$\Omega_0 = \{\boldsymbol{x} = (x, y, z) \in \mathbb{R}^3 : (x/1.5)^2 + y^2 + z^2 \leq 1\}. \tag{3.34}$$

Owing to the symmetry of the ellipsoid and the problem, it is enough to consider one eighth of the ellipsoid. Evolution under Willmore flow has been solved on a grid with

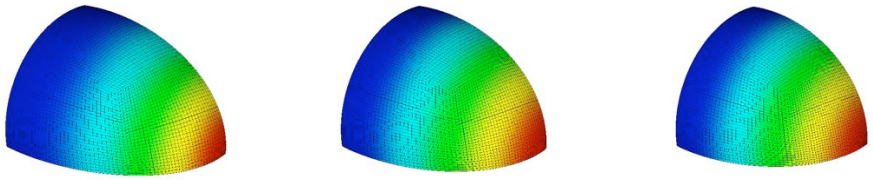

$t = 0.000$ $t = 0.025$ $t = 0.05$

Fig. 3.8. Different time steps of a Willmore flow for 1/8th of the ellipsoid (3.34), where we have used an implicit Euler scheme with $\delta t = 10^{-4}$. The colour encodes the magnitude of curvature, but it is not normalised.

N_{surface}	$\|\boldsymbol{u}_n(T) - \boldsymbol{u}_6(T)\|_{L^2(\Omega;\mathbb{R}^3)}$	EOC
48	0.00364	
192	0.00134	1.44
768	0.00039	1.79
3072	0.00010	1.97

Table 3.5. Experimental order of convergence using an implicit Euler time stepping scheme with $\delta t = 10^{-4}$ and n subsequent local mesh refinements in the vicinity of the surface, corresponding to N_{surface} surface quadrilaterals. The errors are determined at $T = 500\ \delta t$ by a comparison with the solution $\boldsymbol{u}_6(T)$ determined on a grid, where the surface is discretised by $3 \cdot 4^6 = 12\,288$ quadrilaterals.

$48 - 12\,288$ $(3 \cdot 4^2 - 3 \cdot 4^6)$ roughly equally spaced quadrilaterals approximating one eighth of the ellipsoid's surface (3.34). With respect to an investigation of convergence, it is sufficient to consider the discretisation of the surface alone, as mentioned above. Relatively small time steps have been chosen for the simulations, such that the error of the time stepping scheme should be negligible compared to errors of the spatial discretisation. The experimental order of convergence is shown in Table 3.5. It is slightly higher than the experimental order of convergence of 1.5 reported by Clarenz et al. (2004).

Simulations of $\boldsymbol{u}_6$, i.e. simulations with a discretisation of $3 \cdot 4^6 = 12\,288$ surface quadrilaterals, correspond to over 70 000 nodes discretising the ellipsoid. Using implicit schemes this corresponds to over $9 \cdot 70\,000 = 630\,000$ unknowns. The linear systems have been solved with a GMRES preconditioner and a multigrid method. This is a rather efficient method to solve sparse systems. Nevertheless, computation times were roughly 5 days on a standard PC with 3.0 GHz and 2 GB Ram. Due to computation times and required memory, we have not considered larger discretisations so far.

3.3.2 Red blood cells

In Section 3.2.7, we have derived Model 3.9 for the description of a RBC in an optical tweezer. To account for the optical tweezer, different boundary conditions have been prescribed on the boundary $\partial\Omega_{\text{cell}}$ of the RBC. For simplicity, we consider a modified version with only "one" boundary condition: we account for the optical tweezer via additional forces on the boundary. Simulations including different boundary conditions should also be possible following the approach taken by Clarenz et al. (2004) in the case of Willmore flow on non-closed surfaces. Such an approach would require that the edges of the discretisation coincide more or less with the boundaries of the optical tweezer. A construction of such a grid within the finite element library Gascoigne is at the moment not straight forward, but will be investigated in the future.

Model 3.15. *The mechanics of a RBC clamped into an optical tweezer can be described by the following model (for some fixed time $T > 0$):*

$$\begin{aligned} \frac{d\boldsymbol{u}}{dt} &= \boldsymbol{v} && \text{in } \Omega_{cell}(t) \times [0,T), \\ 0 &= \nabla \cdot \boldsymbol{\sigma}_{cytosol} && \text{in } \Omega_{cell}(t) \times [0,T), \\ 0 &= \nabla \cdot \boldsymbol{v} && \text{in } \Omega_{cell}(t) \times [0,T), \end{aligned}$$

with boundary conditions

$$\begin{aligned} (\boldsymbol{\sigma}_{cytosol} + p_{out}\boldsymbol{I}) \cdot \boldsymbol{n} &= \boldsymbol{T} + \boldsymbol{N} + \boldsymbol{F}_{tweezer} && \text{on } \partial\Omega_{cell}(t) \times [0,T), \\ 0 &= J^{\Gamma} - 1 && \text{on } \partial\Omega_{cell}(t) \times [0,T). \end{aligned}$$

The evolution of $\Omega_{cell}(t)$ is given by the speed $\boldsymbol{v}$ on the boundary. Here, we use

$$\begin{aligned} \boldsymbol{\sigma}_{cytosol} &= -p\boldsymbol{I} + \eta\left(\nabla\boldsymbol{v} + (\nabla\boldsymbol{v})^T\right), \\ \boldsymbol{T} &= \nabla^{\Gamma} \cdot \boldsymbol{\tau}, \\ \boldsymbol{N} &= \kappa(\Delta^{\Gamma} H + (H - H_0)(H^2 - 2K) - \frac{1}{2}(H - H_0)^2 H)\boldsymbol{n}, \\ \boldsymbol{\tau} &= -q\boldsymbol{P} + \frac{2}{1 + I_1}\frac{\partial\Psi}{\partial I_2}\boldsymbol{F}^{\Gamma} \cdot \boldsymbol{F}^{\Gamma^T} + \frac{\partial\Psi}{\partial I_1}\boldsymbol{P}. \end{aligned}$$

The additional forces modelling the effect of the microbeads in the case of a prescribed force are given by

$$\boldsymbol{F}_{tweezer} = \chi_{tweezer} f_{force} \boldsymbol{n}_{bead},$$

alternatively by

$$\boldsymbol{F}_{tweezer} = \chi_{tweezer} f_{speed}(\boldsymbol{u} - \boldsymbol{V}_{bead} t)$$

in the case of a prescribed speed. The energy Ψ is given by

$$\Psi = \frac{\mu}{2}(I_2 + 2I_1^2 - 2I_1) + \beta(I_2^2 - 4I_1^2)$$

with $I_1 = J^{\Gamma} - 1$ and $I_2 = \operatorname{tr}(\boldsymbol{F}^{\Gamma} \cdot \boldsymbol{F}^{\Gamma^T}) - 2$ (c.f. the definition given in (3.12)).

Here, $\boldsymbol{n}_{\text{bead}}$ is the normal of the bead, $\boldsymbol{V}_{\text{bead}}$ is the speed of the bead, and χ_{tweezer} is the characteristic function of the microbeads. Further, f_{force} and f_{speed} are force constants, where the latter has no physical meaning but ensures Dirichlet-like boundary conditions for large values. For more details on the notation we would like to refer to the original formulation of Model 3.9 in Section 3.2.7.

Guided by the examples of Section 3.3.1, we now derive the corresponding weak formulation of Model 3.15, or rather Model 3.9. The main difficulty in the derivation are the forces due to curvature, i.e. the Willmore-type forces $\boldsymbol{N}$. For notational convenience let us consider the case $\kappa = 1$. First, we rewrite the corresponding strong formulation using the following elementary geometric relations (Rusu, 2005) to obtain the normal forces in a divergence form, i.e. $\boldsymbol{N} = \nabla^\Gamma \cdot (\dots)$,

$$|\nabla^\Gamma \boldsymbol{n}|^2 = H^2 - 2K, \tag{3.35}$$

$$\Delta^\Gamma \boldsymbol{n} = -|\nabla^\Gamma \boldsymbol{n}|^2 \boldsymbol{n} + \nabla^\Gamma H. \tag{3.36}$$

Here, the sign in front of $\nabla^\Gamma H$ differs from the expression of Rusu (2005) since we work with outward unit normals rather than inward unit normals. The first expression follows immediately using the fact that the eigenvalues C_i of the shape operator $|\nabla^\Gamma \boldsymbol{n}|$ are the principal curvatures, and $K = C_1 C_2$ as well as $H = C_1 + C_2$. The second expression can be proven in a more or less straight forward manner using elementary definitions and some very tedious algebraic manipulations.

Using (3.35), (3.36), $\nabla^\Gamma(H - H_0) = \nabla^\Gamma H$, and $(H - H_0)\nabla^\Gamma H = \frac{1}{2}\nabla^\Gamma (H - H_0)^2$, we recover

$$\begin{aligned}
\boldsymbol{N} &= (\Delta^\Gamma(H - H_0))\boldsymbol{n} + (H - H_0)\left(H^2 - 2K\right)\boldsymbol{n} - \frac{1}{2}(H - H_0)^2 H\boldsymbol{n} \\
&= (\Delta^\Gamma(H - H_0))\boldsymbol{n} + (H - H_0)|\nabla^\Gamma \boldsymbol{n}|^2 \boldsymbol{n} - \frac{1}{2}(H - H_0)^2 H\boldsymbol{n} \\
&= (\Delta^\Gamma(H - H_0))\boldsymbol{n} - (H - H_0)(\Delta^\Gamma \boldsymbol{n}) + (H - H_0)(\nabla^\Gamma H) - \frac{1}{2}(H - H_0)^2 H\boldsymbol{n},
\end{aligned}$$

and hence

$$\boldsymbol{N} = (\Delta^\Gamma(H - H_0))\boldsymbol{n} - (H - H_0)(\Delta^\Gamma \boldsymbol{n}) + \frac{1}{2}(\nabla^\Gamma (H - H_0)^2) - \frac{1}{2}(H - H_0)^2 H\boldsymbol{n}.$$

In view of the definition of the tangential gradients, we have $\boldsymbol{P} \cdot \nabla^\Gamma = \nabla^\Gamma$ as well as $\boldsymbol{P}^T = \boldsymbol{P} = \nabla^\Gamma \boldsymbol{x}$, where $\boldsymbol{P}$ is the tangential projection operator. This implies

$$\begin{aligned}
\boldsymbol{N} =& (\Delta^\Gamma(H - H_0))\boldsymbol{n} - (H - H_0)(\Delta^\Gamma \boldsymbol{n}) \\
&+ \frac{1}{2}(\nabla^\Gamma \boldsymbol{x}) \cdot (\nabla^\Gamma (H - H_0)^2) + \frac{1}{2}(H - H_0)^2 \Delta^\Gamma \boldsymbol{x},
\end{aligned} \tag{3.37}$$

where we have also used $H\boldsymbol{n} = -\Delta^\Gamma \boldsymbol{x}$. Adding

$$0 = -2\nabla^\Gamma \cdot [(H - H_0)(\nabla^\Gamma \boldsymbol{n})] + 2(H - H_0)(\Delta^\Gamma \boldsymbol{n}) + 2(\nabla^\Gamma \boldsymbol{n}) \cdot (\nabla^\Gamma (H - H_0)),$$

which is also nothing else than the chain rule, to the right hand side of (3.37) and using the chain rule several times, we have

$$\begin{aligned}\boldsymbol{N} =& -2\nabla^\Gamma \cdot [(H-H_0)(\nabla^\Gamma \boldsymbol{n})] + (H-H_0)(\Delta^\Gamma \boldsymbol{n}) + 2(\nabla^\Gamma \boldsymbol{n})\cdot(\nabla^\Gamma(H-H_0)) \\ &+ (\Delta^\Gamma(H-H_0))\boldsymbol{n} + \frac{1}{2}\nabla^\Gamma \cdot [(H-H_0)^2(\nabla^\Gamma \boldsymbol{x})] \\ =& -2\nabla^\Gamma \cdot [(H-H_0)(\nabla^\Gamma \boldsymbol{n})] + \nabla^\Gamma \cdot [(H-H_0)(\nabla^\Gamma \boldsymbol{n})] \\ &+ \nabla^\Gamma \cdot [\boldsymbol{n} \otimes (\nabla^\Gamma(H-H_0))] + \frac{1}{2}\nabla^\Gamma \cdot [(H-H_0)^2(\nabla^\Gamma \boldsymbol{x})].\end{aligned}$$

After using the chain rule once more, we recover

$$\boldsymbol{N} = -2\nabla^\Gamma \cdot [(H-H_0)(\nabla^\Gamma \boldsymbol{n})] + \Delta^\Gamma((H-H_0)\boldsymbol{n}) + \frac{1}{2}\nabla^\Gamma \cdot [(H-H_0)^2(\nabla^\Gamma \boldsymbol{x})]. \quad (3.38)$$

The strong formulation (3.38) has now a divergence form, which allows us to perform a partial integration after multiplication with an arbitrary test function $\phi \in C^\infty(\partial\Omega(t); \mathbb{R})$:

$$\begin{aligned}\int_{\partial\Omega(t)} \phi \boldsymbol{N} d\mu = \int_{\partial\Omega(t)} & 2[(H-H_0)(\nabla^\Gamma \boldsymbol{n})]\cdot(\nabla^\Gamma\phi) - (\nabla^\Gamma((H-H_0)\boldsymbol{n}))\cdot(\nabla^\Gamma\phi) \\ & - \frac{1}{2}[(H-H_0)^2(\nabla^\Gamma \boldsymbol{x})]\cdot(\nabla^\Gamma\phi) d\mu,\end{aligned} \quad (3.39)$$

where no boundary terms appear because $\partial\Omega(t)$ is a closed surface.

The weak formulation (3.39) still contains derivatives of the normal $\boldsymbol{n}$. It can be simplified using the following geometric equality (Rusu, 2005):

$$\begin{aligned}(H-H_0)(\nabla^\Gamma \boldsymbol{n})\cdot(\nabla^\Gamma\phi) =& \nabla^\Gamma \cdot ((H-H_0)(\boldsymbol{n}\cdot\boldsymbol{n})\boldsymbol{n} \otimes (\nabla^\Gamma\phi)) \\ & - \boldsymbol{n}\otimes\boldsymbol{n}\cdot(\nabla^\Gamma((H-H_0)\boldsymbol{n}))\cdot(\nabla^\Gamma\phi) - (H-H_0)\boldsymbol{n}\Delta^\Gamma\phi.\end{aligned}$$

The equality follows from the chain rule and $\boldsymbol{n}\cdot\boldsymbol{n} = 1$, and accordingly $\nabla^\Gamma(\boldsymbol{n}\cdot\boldsymbol{n}) = 2\boldsymbol{n}\cdot(\nabla^\Gamma\boldsymbol{n}) = 0$. Integration over $\partial\Omega(t)$ yields

$$\begin{aligned}\int_{\partial\Omega(t)} (H-H_0)(\nabla^\Gamma \boldsymbol{n})\cdot(\nabla^\Gamma\phi) d\mu = \int_{\partial\Omega(t)} \Big[& \nabla^\Gamma \cdot ((H-H_0)(\boldsymbol{n}\cdot\boldsymbol{n})\boldsymbol{n}\otimes(\nabla^\Gamma\phi)) \\ & - \boldsymbol{n}\otimes\boldsymbol{n}\cdot(\nabla^\Gamma((H-H_0)\boldsymbol{n}))\cdot(\nabla^\Gamma\phi) - (H-H_0)\boldsymbol{n}\Delta^\Gamma\phi\Big] d\mu,\end{aligned} \quad (3.40)$$

or rather

$$\begin{aligned}\int_{\partial\Omega(t)} (H-H_0)(\nabla^\Gamma \boldsymbol{n})\cdot(\nabla^\Gamma\phi) d\mu = \int_{\partial\Omega(t)} \Big[& -\boldsymbol{n}\otimes\boldsymbol{n}\cdot(\nabla^\Gamma((H-H_0)\boldsymbol{n}))\cdot(\nabla^\Gamma\phi) \\ & + (\nabla^\Gamma((H-H_0)\boldsymbol{n}))\cdot(\nabla^\Gamma\phi)\Big] d\mu\end{aligned} \quad (3.41)$$

using partial integration. The first term on the right hand side of (3.40) vanishes since it has a divergence form and only closed surfaces are considered, i.e. no boundary terms appear.

Applying equality (3.41), expression (3.39) simplifies to

$$\int_{\partial\Omega(t)} \phi \boldsymbol{N} d\mu = \int_{\partial\Omega(t)} (\nabla^\Gamma((H-H_0)\boldsymbol{n})) \cdot (\nabla^\Gamma \phi) - 2\boldsymbol{n}\otimes\boldsymbol{n} \cdot (\nabla^\Gamma((H-H_0)\boldsymbol{n})) \cdot (\nabla^\Gamma\phi) - \frac{1}{2}[(H-H_0)^2(\nabla^\Gamma \boldsymbol{x})] \cdot (\nabla^\Gamma\phi) d\mu,$$

which agrees with the results of Rusu (2005) considering $H_0 = 0$. Introducing the mean curvature tensor

$$\boldsymbol{Y} = -\Delta^\Gamma \boldsymbol{x} - H_0 \boldsymbol{n}$$

as an additional variable, we recover a weak formulation for the normal surface forces $\boldsymbol{N}$, which includes only first order derivatives. This formula is suitable for implementation in "standard" finite element libraries. The weak formulation of all other terms in Model 3.15 is more or less straight forward, such that we recover the following weak version.

Model 3.16. *The weak formulation of Model 3.15 is given by*

$$\begin{aligned}
\int_{\Omega(t)} \phi \frac{d\boldsymbol{u}}{dt} d\mu &= \int_{\Omega(t)} \phi \boldsymbol{v} d\mu, \\
0 &= \int_{\Omega(t)} \boldsymbol{\sigma}_{cytosol} \cdot (\nabla\phi) d\mu, \\
0 &= \int_{\Omega(t)} \phi \nabla \cdot \boldsymbol{v} d\mu,
\end{aligned}$$

and

$$\begin{aligned}
\int_{\partial\Omega(t)} \phi^\Gamma(\boldsymbol{\sigma}_{cytosol} + p_{out}\boldsymbol{I}) \cdot \boldsymbol{n} d\mu = &- \int_{\partial\Omega(t)} \boldsymbol{\tau} \cdot (\nabla^\Gamma \phi^\Gamma) d\mu \\
&- \kappa \int_{\partial\Omega(t)} \frac{1}{2}|\boldsymbol{Y}|^2 (\nabla^\Gamma \boldsymbol{x}) \cdot (\nabla^\Gamma \phi^\Gamma) - (\nabla^\Gamma \boldsymbol{Y}) \cdot (\nabla^\Gamma \phi^\Gamma) \\
&\qquad + 2\boldsymbol{n}\otimes\boldsymbol{n} \cdot (\nabla^\Gamma \boldsymbol{Y}) \cdot (\nabla^\Gamma \phi^\Gamma) d\mu \\
&+ \int_{\partial\Omega(t)} \phi^\Gamma \boldsymbol{F}_{tweezer} d\mu, \\
0 = &\int_{\partial\Omega(t)} (J^\Gamma - 1)\phi^\Gamma d\mu, \\
\int_{\partial\Omega(t)} \phi^\Gamma \boldsymbol{Y} d\mu = &\int_{\partial\Omega(t)} (\nabla^\Gamma \boldsymbol{x}) \cdot (\nabla^\Gamma \phi^\Gamma) - \phi H_0 \boldsymbol{n} d\mu,
\end{aligned}$$

where $\phi \in C_0^\infty(\Omega(t);\mathbb{R})$ and $\phi^\Gamma \in C^\infty(\partial\Omega(t);\mathbb{R})$ are arbitrary test functions. Here, $\boldsymbol{\sigma}_{cytosol}$, $\boldsymbol{\tau}$, and $\boldsymbol{F}_{tweezer}$ are defined as in Model 3.15.

(a) 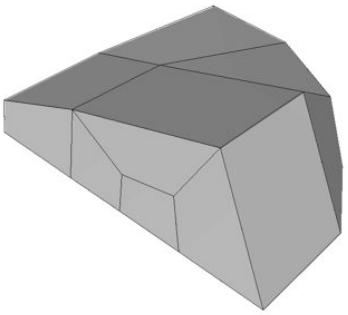 (b) 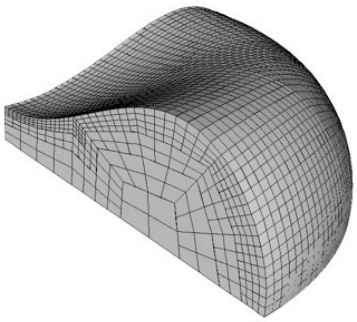

Fig. 3.9. Typical discretisations: (a) initial discretisation; (b) discretisation after grid refinement (2048 surface quadrilaterals)

The bulk part of Model 3.15 corresponds to a stationary incompressible Stokes flow. Here, we consider the following perturbed version of the Stokes equation

$$\begin{aligned} 0 &= \nabla \cdot \boldsymbol{\sigma}_{\text{cytosol}} && \text{in } \Omega_{\text{cell}}(t) \times [0,T), \\ 0 &= \nabla \cdot (\boldsymbol{v} + \varepsilon_{\text{stab},1} \nabla p) && \text{in } \Omega_{\text{cell}}(t) \times [0,T) \end{aligned} \tag{3.42}$$

with an additional natural boundary condition for p, i.e.

$$\boldsymbol{n} \cdot \nabla p = 0 \qquad \text{on } \partial\Omega_{\text{cell}}(t) \times [0,T).$$

This perturbation allows a discretisation via the standard Galerkin procedure, i.e. using the same type of ansatzfunctions for all variables. Typically one uses $\varepsilon_{\text{stab},1} \approx \frac{\delta x^2}{\mu}$, where δ_x is the size of the discretisation. In many cases the solutions depend only weakly on the exact value of $\varepsilon_{\text{stab},1}$. Similarly to the incompressible Stokes equation, we work with the following perturbed problem for the membrane mechanics:

$$\begin{aligned} (\boldsymbol{\sigma}_{\text{cytosol}} + p_{\text{out}} \boldsymbol{I}) \cdot \boldsymbol{n} &= \boldsymbol{T} + \boldsymbol{N} + \boldsymbol{F}_{\text{tweezer}} && \text{on } \partial\Omega_{\text{cell}}(t) \times [0,T), \\ 0 &= J^{\Gamma} - 1 + \varepsilon_{\text{stab},2} \Delta^{\Gamma} q && \text{on } \partial\Omega_{\text{cell}}(t) \times [0,T). \end{aligned} \tag{3.43}$$

An introduction of additional boundary conditions for the surface pressure q is not necessary since $\partial\Omega_{\text{cell}}$ is closed. An extension of the weak formulation 3.16 with respect to the perturbed problems (3.42) and (3.43) is straight forward.

In Model 3.15, we include the optical tweezers as additional forces on the boundary. This implies the introduction of the characteristic function χ_{tweezer} of the optical tweezers. The tweezers coincide of course not directly with the grid. This might lead to inaccuracies if the grid-size and the microbead are of a similar order. Therefore, we have chosen an "adaptive" integration with 100 function evaluations per quadrilateral close to the optical tweezer. Typically, the weak formulation is approximated by an integration formula with four function evaluations. Grids used in the computations are shown in Fig. 3.9. For further implementational aspects we refer to Section 3.3.1.

Bending elasticity κ	$2 \cdot 10^{-19}$J	Scheffer et al. (2001), Mohandas and Evans (1994)
Shear elasticity modulus μ	$2 - 6 \cdot 10^{-6}$N/m	Lenormand et al. (2001), Mohandas and Evans (1994)
Cytosol viscosity η	$6.0\text{cp} = 6.0 \cdot 10^{-3}$Pa s	Pozrikidis (2003b)
Spont. membrane curvature H_0	$0 - 0.35 \cdot 10^{6}\text{m}^{-1}$	see text
Initial shape		Evans and Skalak (1980)

Table 3.6. Experimentally determined parameters

Simulations

The goal of this section is to simulate Model 3.15 in a setting as realistic as possible. To do so, parameters and initial conditions are taken from experiments rather than from a microscopic estimation of parameters as given in Section 3.2.3. Once "better" microscopic models are available, a connection between microscopic and macroscopic equations in a quantitative way should be possible. The simulations presented here are compared with experimental results, obtained by Hénon et al. (1999) and Li et al. (2005).

A quantitative characterisation of the rest shape of RBCs has been given by Evans and Skalak (1980), c.f. formula (3.1). This characterisation is used as the initial shape in our simulations. We follow Li et al. (2005) and assume that the attachment of the microbead to the RBC does not alter the initial shape of the RBC. This is of course a quite crude assumption, but it should not influence the results quantitatively on the order of experimental accuracy. Let the contact area of the microbead with respect to the reference configuration be given by

$$\partial\Omega_{\text{tweezer},0} = \{\boldsymbol{x} = (x, y, z) \in \partial\Omega_{\text{cell},0} : x^2 + z^2 \leq R^2_{\text{tweezer}}\}, \tag{3.44}$$

with $R_{\text{tweezer}} = 0.8\mu$m. This corresponds to an area of contact of approximately $2.1\mu\text{m}^2$ per bead.

Parameters of Model 3.9 for RBCs found in the literature are summarised in Table 3.6. The spontaneous membrane curvature can be "guessed" only roughly: The volume of the RBC equals $V = 1.57R_0^3 = 94.10\mu\text{m}^3$, which corresponds to a ball of radius $R = 2.82\mu$m. We therefore expect the spontaneous membrane curvature in the range from $H_0 = 0$ to $H_0 = \frac{1}{2.82} \cdot 10^6\text{m}^{-1}$. Since the exact nature of nonlinearities in surface elasticity is not clear (Li et al., 2005), we choose for simplicity $\beta = 0$. In a later step, parameter estimation could be used to extract corresponding parameters of our model from experiments (see e.g. Mills et al., 2004).

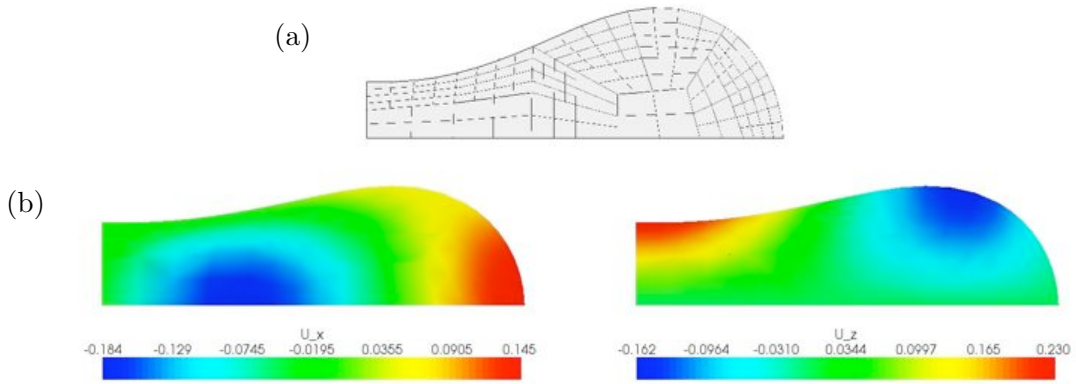

Fig. 3.10. Relaxation of the initial shape of a red blood cell given by Evans and Skalak (1980), i.e. formula (3.1). Here, we have used an implicit Euler time stepping scheme with time step size $\delta t = 0.0003$s and parameters $\mu = 0$, $\kappa = 0.2 \cdot 10^{-19}$J, $H_0 = 0.1 \cdot 10^{6}\mathrm{m}^{-1}$, $\eta = 6.0$cp. Figure (a) shows the initial shape given by formula (3.1). Figure (b) shows the relaxed shape after 3s. In the left part the deformation in the radial direction and in the right part the deformation in the z-direction is shown.

Relaxation experiments (Fig. 3.10): (Li et al., 2005) have proposed that rest shapes of RBCs minimise the Canham-Helfrich energy (3.21), since the membrane-bound cytoskeleton is constantly rearranging and thus allows relaxation of any stresses on long time scales. The minimal energy configuration of the Canham-Helfrich energy depends solely on the volume/area ratio and the spontaneous curvature H_0 (Seifert et al., 1991). The rest shape given by formula (3.1) is based on an experimental characterisation of RBCs by Evans and Skalak (1980). Hence, it might not necessarily be a minimal energy configuration with respect to the Canham-Helfrich energy.

Let us neglect the mechanics of the membrane-associated cytoskeleton for the moment. Simulations with an initial shape given by formula (3.1) are shown in Fig. 3.10. The shape has been allowed to relax over $3s$ (10^4 time steps), after which the velocity is virtually zero. Since the shape has relaxed only slightly, we can conclude that the minimal energy configuration of the Canham-Helfrich energy with $H_0 = 0.1 \cdot 10^{-6}\mathrm{m}^{-1}$ is indeed close to the experimentally observed rest shapes. A variation of H_0 within the range $0 - 0.2 \cdot 10^{-6}\mathrm{m}^{-1}$ does not change the results qualitatively.

Deformation experiments (Fig. 3.11): The next computational experiment considers the evolution of a RBC with a prescribed deformation of the optical tweezers. As explained above, this is achieved via non-physical forces enforcing the deformation of the tweezer. The results shown in Fig. 3.11 agree qualitatively with the discrete model of Li et al. (2005) as well as with the shapes observed by Hénon et al. (1999).

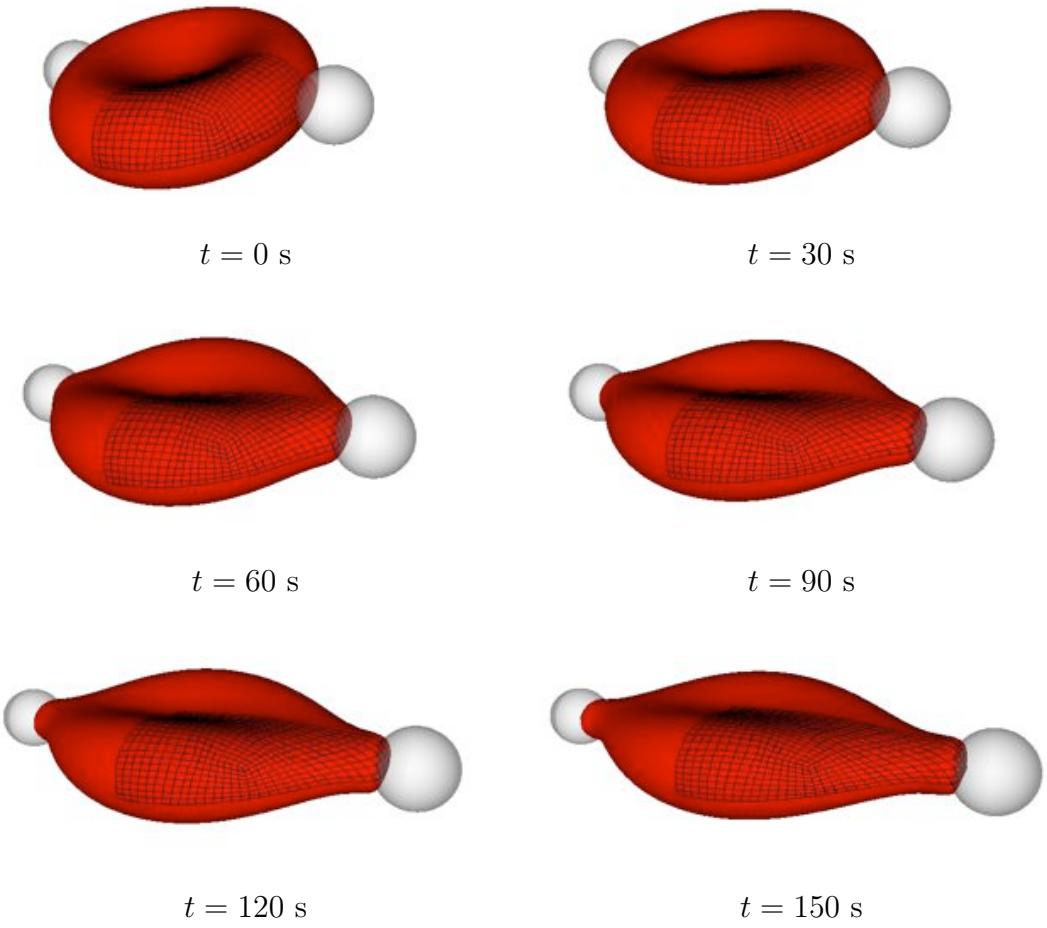

Fig. 3.11. Evolution of a red blood cell (Model 3.15) under a prescribed deformation of the microbead. Parameters of the model are $\eta = 6.0$cp, $\mu = 4 \cdot 10^{-6}$N/m, $\kappa = 0.2 \cdot 10^{-19}$J, and $H_0 = 0.1 \cdot 10^6 \mathrm{m}^{-1}$ (see Table 3.10). The results have been obtained using an implicit Euler scheme with time step size $\delta t = 0.06$s.

Force experiments (Fig. 3.12): Typical experiments consider microbeads subject to a constant force and not subject to a prescribed deformation as above. The objective of such force experiments is to measure the longitudinal and transversal radii as a function of the applied stretching force (Hénon et al., 1999; Li et al., 2005). Here, we consider the same experiments *in silicio* using Model 3.15. The results for different shear elasticity moduli μ are shown in Fig. 3.12. They agree within experimental accuracies quantitatively quite well with the ones reported in the literature (Hénon et al., 1999; Li et al., 2005).

Choosing different radii of the microbeads, our results change only slightly, i.e. curves shown in Fig. 3.12 cannot be distinguished. This justifies our very crude approach introducing the microbeads.

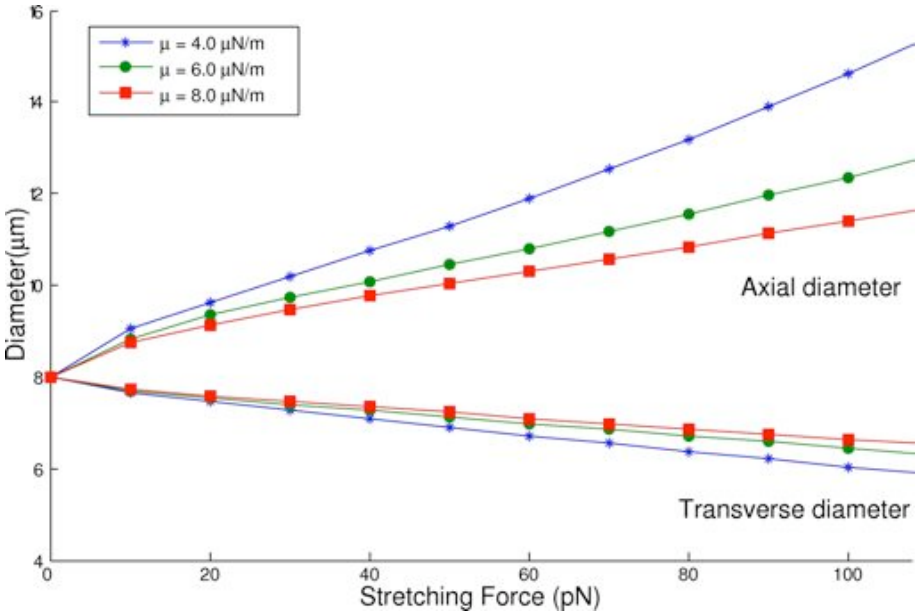

Fig. 3.12. Evolution of a red blood cell (Model 3.15) for different values of μ and prescribed forces. Parameters are $\eta = 6.0\text{cp}$, $\kappa = 0.2 \cdot 10^{-19}\text{J}$, and $H_0 = 0.1 \cdot 10^{6}\text{m}^{-1}$.

N_{surface}	$\lvert R_n^{\text{L}} - R_5^{\text{L}} \rvert$	EOC
128	0.0184	
512	0.0054	1.77
2048	0.0018	1.59

Table 3.7. Experimental order of convergence with respect to the longitudinal radius R^L of the red blood cell after stretching by a given force. The different surface discretisations with N_{surface} quadrilaterals are obtained by n subsequent local mesh refinements in the vicinity of the surface. The following parameters have been used $\mu = 6 \cdot 10^{-6}\text{N/m}$, $\eta = 6.0\text{cp}$, $\kappa = 0.2 \cdot 10^{-19}\text{J}$, and $H_0 = 0.1 \cdot 10^{6}\text{m}^{-1}$.

In addition, we have used the force experiments to determine convergence properties of the applied numerical scheme. To do so, we have simulated the same set of parameters on meshes with different local mesh refinements close to the surface. An experimental order of convergence determined from this set of simulations (see Table 3.7) is however only a rough guideline. It is based on subsequent refinements close to the surface, whereas the evolution of the cell is due to the interaction of membrane and bulk mechanics. But as the evolution is driven by surface mechanics, the region in the vicinity of the surface and the surface itself should the "critical" regions where the largest error is made. Thus the experimental order of convergence shown in Table 3.7 should have some predictive power and therefore affirms convergence of the applied numerical scheme. A more rigorous investigation using adaptive mesh refinement is an open problem for future research.

3.4 Summary and discussion

In this chapter, we have rigorously derived a macroscopic continuum model for the RBC based on a microscopic description. Mechanics of the RBC are determined by the mechanics of the cytosol, the membrane (lipid bilayer), and the membrane-bound cytoskeleton. The latter consists of a network of spectrin filaments with a roughly hexagonal symmetry. The considered microscopic models of the spectrin network is given in terms of an energy functional, as it is typical in soft-matter physics. Such a microscopic description via energy functionals has allowed us to apply the mathematical tools outlined in Chapter 2. Considering the limit where the length scale of the spectrin network converges to zero, we have rigorously derived the corresponding continuum model. Further, we have assumed that the mechanics of the lipid bilayer are determined by the Canham-Helfrich energy (Canham, 1970; Helfrich, 1973). Using a variational approach, corresponding stress tensors have been derived (Section 3.2.5). Together with a model of the cytosol, we have been thus able to give a complete continuum description of the RBC.

In Section 3.2.3, we have shown convergence of the discrete models to a continuum model considering the limit of vanishing spectrin link lengths. However in reality, the structure is discrete with link lengths strictly larger than zero. It is an open problem to determine rigorous error estimates. With respect to simulations and a comparison to experimental results such an analysis would be highly relevant.

A drawback of the approach pursued here is the required hexagonal symmetry for the derivation of a homogenisation formula. With respect to convergence results this assumption might be lifted (see Discussion 2.6). Assuming a hexagonal symmetry in the discrete model, the continuum model usually reflects the symmetry. However, the membrane skeleton does not show a perfect hexagonal symmetry, such that an isotropic description would be more realistic. Here, we have applied some heuristic averaging to account for isotropy. Alternative approaches should be investigated in the future. A stochastic approach would offer the chance to characterise continuum models quantitativly very exactly, as a statistical description of cytoskeletal networks is well in reach (Beil et al., 2006).

Our rigorous approach is similar to the formal approach of Discher et al. (1997) or Dao et al. (2006). However in this thesis, we have proved rigorous convergence results and related the results to typical constitutive relations used for hyperelastic materials. Within hyperelasticity the constitutive relations, i.e. the relations linking strain and stress, or rather deformation and force, are given as energy functions in terms of invariants of the deformation tensor. In addition, Dao et al. (2006) and Mills et al. (2004), like many others, do not consider the membrane and the membrane-associated cytoskeleton as a hypersurface. Instead, they assume that the membrane is an object with a small, but finite thickness. Thus standard commercial finite element solvers can be used. However, a two-dimensional surface embedded in a three-dimensional

space is the widely accepted description for the lipid bilayer (Boal, 2002).

In this chapter, we have further investigated the application of the derived continuum model to optical tweezer experiments. To do so, the model has been implemented using the finite element toolbox GASCOIGNE (Becker et al., 2007). Considering the membrane as a hypersurface and assuming that bulk mechanics are given by the Stokes equation, boundary element methods are typically used (e.g. Pozrikidis, 2001). These allow an efficient simulation but are restricted to linear models for bulk mechanics. Using a finite element approach allows a greater flexibility with respect to an extension to more complex cells. Therefore, our implementation within a finite element framework does not only serve as a verification of the derived model, but also as a test case for the development of flexible computational tools for single cell mechanics.

The implementation of the derived model within a finite element framework is discussed in detail in Section 3.3. A fully implicit coupling of surface mechanics with bulk mechanics has not been investigated so far. Therefore, some typical surface evolution problems of differential geometry have been considered to validate the approach and to determine convergence properties of the numerical schemes (Section 3.3.1). Simulations of optical tweezer experiments with the developed computational framework reproduce the experimental results qualitatively and quantitatively quite well (Section 3.3.2). Hence, the models as well as the applied numerical schemes are validated.

The developed numerical framework is highly flexible. We thus hope to apply it in the future to different experiments, e.g. micropipette aspiration, to more realistic models, e.g models including viscoelasticity, as well as to other more complex cells. Using the optimisation package RODOBO (Becker et al., 2007) for partial differential equations with an interface to GASCOIGNE, also parameter estimation problems are directly accessible by our approach. Since the computations are quite time consuming, the use of adaptive mesh refinement strategies is a further important issue, especially with respect to parameter estimation problems, to be addressed in the future.

The developed modelling and simulation framework is a promising starting point for theoretical investigations of cytoskeletal networks, or alternatively polymer networks, and single cell mechanics.

Chapter 4

Growing cell cultures

Our investigation of red blood cells has been restricted to mechanics alone. In this chapter, we investigate growing cell cultures as a test case for the multiscale analysis introduced in Chapter 2 considering also the interactions between biological processes and mechanics. From an experimental point of view, cell cultures are less understood than red blood cells, therefore this chapter is more concerned with qualitative rather than quantitative behaviour.

First, we review some biological facts about growing cell cultures in Section 4.1. Describing growing cell cultures as an elastic or viscoelastic material, the characterisation of constitutive equations (stress-strain relations) is non-trivial. Using the multiscale ansatz, an appropriate derivation of stress-strain relationships is possible. Our approach, outlined in Section 4.2, is based on a simple microscopic cellular-automaton-like description of a growing cell culture.

To validate the derived continuum models, we investigate the generation of branch structures common to many growing cell cultures. Considering a viscoelastic model in the limit of fast stress relaxation, we show in Section 4.3 via a linear stability analysis that the model can reproduce the formation of branch structures.

4.1 Biological background

Spatial growth of cell populations is a major issue in biology, e.g. developmental biology, and it has been studied from an experimental viewpoint for a long time. Since growth fulfils many different functions in biological systems, quite a variety of different growth processes are found. In a coarse classification, one can distinguish between tip growth, surface growth, and volumetric growth. Tip growth is typically found in many filamentary systems, like fungi or plants, whereas surface growth is typically responsible for growth of hard tissues, like teeth or horns and to a lesser extent bones (Ben Amar and Goriely, 2005). Here, we restrict ourselves to volumetric growth typically found in soft tissues, e.g. embryonic tissues (Miura and Shiota,

2002), growth of arteries (Ambrosi et al., 2007), or tumour growth (Ambrosi and Mollica, 2002). As an application of our multiscale approach, we consider the problem of branching morphogenesis in developmental biology (see Section 4.1.2).

4.1.1 Different aspects of volumetric growth

For an appropriate modelling of growth a lot of different effects have to be considered. In this thesis, we concentrate on the interplay between growth and mechanics. Let us first outline a few aspects which are important in this context. For more details we would like to refer to the review of Cowin (2004).

Typically, growth is modulated by availability of nutrients as well as by a complex chemical control. In addition, a dependence of growth on mechanical stresses has been reported (Ambrosi and Mollica, 2002; Ambrosi and Guana, 2005). Such a dependence accounts for the natural tendency of biological systems to maintain equilibrium by adaptation. Due to this complex "control", growth is typically non-uniform as well as anisotropic. This complicates the identification of corresponding growth laws from experiments. But in general the influence is bidirectional: on the one hand stresses influence growth, on the other hand growth also influences the mechanics of a biological material. Because growth is often not uniform it enforces the material to stretch or shrink, ensuring that no cavitation or overlap occurs, i.e. growth induces stresses. Furthermore, growth implies in many cases also a remodelling of the biological system via an adaptation of the shape and internal microstructure. Therefore, growth influences the way the material responds to strains, i.e. growth implies an evolution of the constitutive equations.

4.1.2 Morphogenesis and growth

Understanding growth is of high interest in the field of morphogenesis, a fundamental aspect of developmental biology. Morphogenesis is concerned with the shapes of tissues, organs, and entire organisms. Such shapes do not exist as a blueprint in the genome, but are rather the achievement of self-organisation via the interactions of growth, mechanics, and chemical control. One example of such highly organised structures are branch structures, typically found in systems where growth is stimulated by the uptake / binding of a diffusing chemical (see Fig. 4.1).

Among the systems showing branching morphogenesis, epithelial lung cell cultures are one of the best studied systems, since good *in vitro* experimental systems are available. Functionally, the formation of branch patterns *in vivo* enlarges the surface area of the lung to exchange O_2 and CO_2. From a physiological point of view it is of high interest to understand the generation of branch structures.

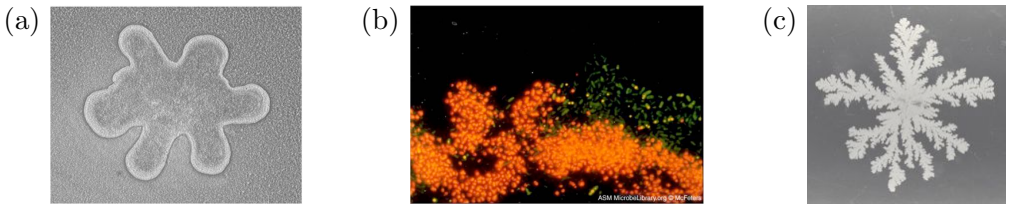

Fig. 4.1. Three examples of branch structures in growing cell cultures: (a) lung epithelium cells (courtesy to Takashi Miura, Kyoto University); (b) biofilm composed of two bacterial species, *Klebsiella pneumoniae* and *Pseudomonas aeruginosa* (©McFeters. Licensed for use, ASM MicrobeLibrary.org); (c) *Bacillus subtilis* colony growing on an agar plate with only a few nutrients (courtesy to Mitsugu Matsushita).

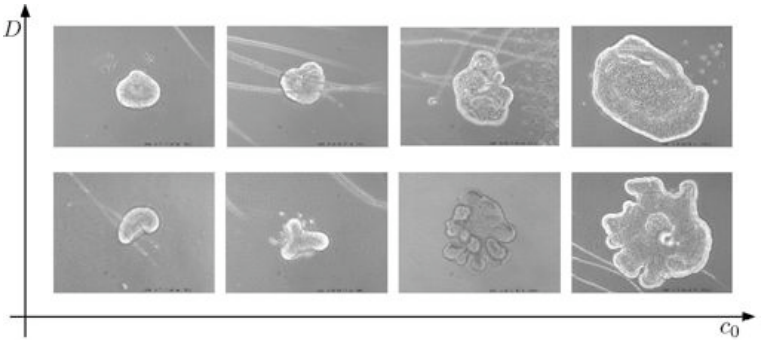

Fig. 4.2. Phase diagram of lung explant morphology with different initial fibroblast growth factor concentrations (FGF) c_0 and diffusion coefficients D. Under very low FGF concentrations branching morphogenesis does not occur since no growth takes place. Under low FGF concentrations a branched morphology is more prominent, and as the FGF concentration rises we obtain a cyst-like morphology with clefts. (reprinted from Hartmann and Miura, 2006, ©2006 Elsevier)

Using *in vitro* experiments, chemical control as well as mechanical influences on the pattern formation are well documented for epithelial lung cell cultures. Varying the chemical control via a modification of the concentration and the diffusion coefficient of fibroblast growth factors (FGF) it is possible to systematically modify the resulting patterns (see Fig. 4.2). Similarly, the resulting patterns can be modified by changing mechanical properties of the cell culture via cytochalasin D (Hartmann and Miura, 2006), which is known to affect actin polymerisation.

Despite all experimental efforts, the main principles of branching morphogenesis of lung cell cultures are not understood among experimental biologists. Especially, it remains unrevealed why the same type of tissue can generate different structures varying among species (Romer and Parsons, 1986): the lung is homologous to the fish swim-bladder, in which no branch structures exist. In birds, distal parts of the airway form simple sac-like structures called air-sacs, while proximal parts retain branched structures. In humans, an initial 2-3 branch pattern is common and at the distal part branch patterns become stochastic.

To answer this type of questions, mathematical modelling may provide a more appropriate form of analysis than molecular biology. Therfore, it is necessary to develop adequate models for interactions between growth, mechanics, and chemical control. Due to the complexity of the biological and mechanical nature of the problem, such a modelling approach is rather hard and has to rely often on crude assumptions. Using the multiscale approach outlined in Chapter 2, we derive appropriate models including mechanical effects in a "realistic" way. The models introduced here, clearly improve the models applied so far as an explanation of branching morphogenesis (Hartmann and Miura, 2007, 2006).

4.2 Modelling

Due to the complexity of the mechanics and biology involved in growth, quite a range of models have been proposed for growing cell cultures: reaction-diffusion equations (Greenspan, 1976), fluid-like models (Cogan and Keener, 2004), elastic models (Ambrosi and Mollica, 2002), as well as multiphasic systems (Humphrey and Rajagopal, 2002), to mention only a few continuous modelling approaches.

Here, we consider a continuous mechanical model (Section 4.2.1): the evolution of the culture due to growth is governed by the balance of mass and momentum. Within this class of models, we restrict our analysis to elastic and viscoelastic models. Corresponding elastic stress tensors are derived in Section 4.2.2 using the multiscale techniques introduced in Chapter 2. In a next step, the derived stress tensors are extended to viscoelastic models (Section 4.2.4).

4.2.1 Continuum model

Let us consider an idealised cell culture $\Omega_{\text{cult}}(t)$ embedded in a medium Ω, as shown in Fig. 4.3a. We consider the cell culture as a continuous material with a sharp boundary, i.e. we treat the evolution of biomass with density ρ and not the evolution of single cells. This makes perfectly sense since typically the number of cells is rather large and one does not see any localisation of growth in single cells. Additionally, let us assume that the medium outside the culture has no influence on the mechanics of the culture. Indeed, it can be shown via a linear stability analysis as in Section 4.3.2 that the mechanics of the outside medium would have no influence on the qualitative behaviour. In our model, the sharp boundary $\partial\Omega_{\text{cult}}(t)$ between the tissue and the surrounding material is considered explicitly.

Let us further assume that growth is promoted by a diffusing chemical substance, e.g. nutrients or growth factors. The chemical substance is taken up by the culture which subsequently induces growth as a function of "consumed" chemicals, one of the most simple bio-chemical controls. A generalisation to more complicated biochemical

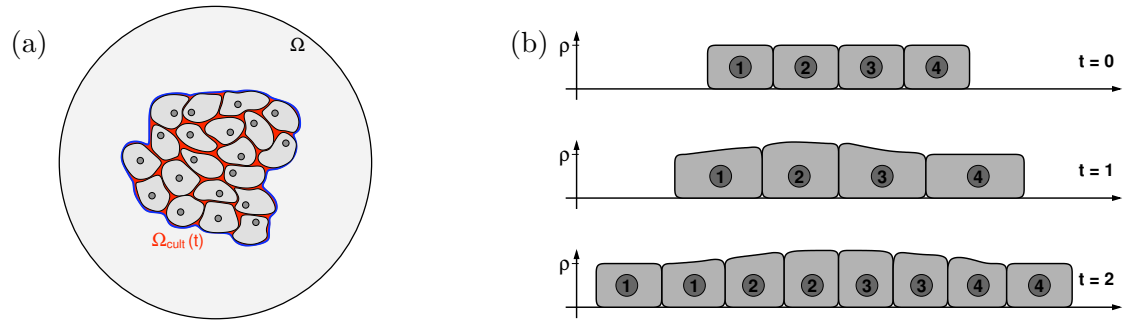

Fig. 4.3. Illustrations of a growing cell culture. Since cells are only compressible to some extent, growth causes an expansion of the culture.

pathways is of course possible. The evolution of the concentration of the growth promoting substance c should be determined by the balance of mass with fluxes given by Fickian diffusion. Further, the concentration should have a smooth distribution throughout the whole domain Ω.

Because cells are only compressible to some extent, growth causes expansion of the culture area $\Omega_{\text{cult}}(t)$ as illustrated in Fig. 4.3b. Here, we assume an incompressible cell culture, which seems reasonable considering that cells consist mainly of water. The evolution of $\Omega_{\text{cult}}(t) \subset \Omega$ is given by the material speed $\boldsymbol{v}$, which is determined by the balance of linear momentum and mass. We further assume that the expansion of the cell culture might be constrained by membrane mechanics of the culture boundary. For example, in the case of epithelial cell cultures such mechanical resistance might originate from the basement membrane. It is a supportive matrix that contains macromolecular components like collagen or laminin, bordering the culture. The mechanical properties of the boundary might be also an "artifact" of the tightly linked cells on the boundary of the cell cultures or due to surface tension. As we will see later, such surface mechanics are important to stabilise the growth of the culture, otherwise one would expect instabilities with "arbitrarily small" wavelengths. One of the simplest approaches to surface mechanics is a description via surface tension, which is supported by the experimental evidences found by Forgacs et al. (1998).

In summary, the following assumptions should hold:

Assumption 4.1.

- *The cell culture is incompressible and its evolution is determined by the balance of momentum and mass.*
- *Mechanics of the outside medium are negligible.*
- *The boundary of the cell cultures resists extension via an effective surface tension.*
- *Growth is promoted by a diffusing chemical, whose evolution is given by a conservation equation with Fickian diffusion.*

The assumptions agree quite well with typical examples of growing cell cultures, e.g. tumour growth (Friedmann, 2004; Ambrosi and Mollica, 2004; Byrne, 1999; Chaplain et al., 1995) or growth of lung epithelial cells *in vitro* (Hartmann and Miura, 2006). They imply that the evolution of the growing cell culture is determined by the following free boundary model, where appropriate boundary conditions on Ω, as well as initial conditions still have to be specified.

Model 4.2. *Let Assumption 4.1 be true, then the evolution of the cell culture is determined by the following set of equations (for some fixed time $T > 0$)*

$$\begin{aligned} \frac{d}{dt}\boldsymbol{u} &= \boldsymbol{v} && \text{in } \Omega_{cult}(t) \times [0,T), \\ \frac{\partial}{\partial t}\rho + \nabla \cdot (\rho \boldsymbol{v}) &= \rho g(c) && \text{in } \Omega_{cult}(t) \times [0,T), \\ \frac{\partial}{\partial t}(\rho \boldsymbol{v}) + \nabla \cdot (\rho \boldsymbol{v} \otimes \boldsymbol{v}) &= \nabla \cdot \boldsymbol{\sigma} + g(c)\rho \boldsymbol{v} && \text{in } \Omega_{cult}(t) \times [0,T), \\ \frac{\partial}{\partial t}c - \nabla \cdot (D \nabla c) &= -\chi_{\Omega_{cult}} \rho f(c) && \text{in } \Omega \times [0,T), \end{aligned} \tag{4.1}$$

with the balance of momentum across the culture boundary

$$(\boldsymbol{\sigma} + p_{medium}\boldsymbol{I}) \cdot \boldsymbol{n} = -\kappa H \boldsymbol{n} \qquad \text{on } \partial\Omega_{cult}(t) \times [0,T).$$

The evolution of $\Omega_{cult}(t) \subset \Omega$ is given by the normal speed of the culture boundary

$$V_n = \boldsymbol{n} \cdot \boldsymbol{v} \qquad \text{on } \partial\Omega_{cult}(t) \times [0,T).$$

The constant ρ is the material density, $\boldsymbol{u}$ the material displacement, $\boldsymbol{v}$ the material speed, c the growth factor concentration, and p_{medium} the constant pressure outside the culture. Further, $\boldsymbol{n}$ is the outside unit normal, H the mean curvature, and $\chi_{\Omega_{\text{cult}}(t)}(\boldsymbol{x})$ the characteristic function of the culture. So far the kinetics f and g, the diffusion constant D, the stress tensor $\boldsymbol{\sigma}$, and the modulus of bending resistance κ have not been specified. Above, we have implicitly assumed that growth also implies the generation of momentum via mass growth, which is a typical assumption considering growing cell cultures (Ambrosi and Mollica, 2002). Furthermore, we have neglected any body forces.

The assumption of a surface tension modelling the resistance of the culture boundary might be oversimplified. In a more "realistic" setting one should consider a shell theory (Libai and Simmonds, 1996), e.g. by extending the approach proposed for a single cell by Pozrikidis (2001) (c.f. Section 3.2.6). To do so, let us assume for simplicity the following linear constitutive relation for the bending moment tensor $\boldsymbol{m}$:

$$\boldsymbol{m} = \kappa H \boldsymbol{P}, \tag{4.2}$$

where κ is the bending modulus, H is the mean curvature, and $\boldsymbol{P} = \boldsymbol{I} - \boldsymbol{n} \otimes \boldsymbol{n}$ is the surface projection operator. Neglecting tangential mechanics, using $\nabla^\Gamma \cdot \boldsymbol{P} = \nabla^\Gamma \cdot (\nabla^\Gamma \boldsymbol{x}) = H\boldsymbol{n}$ with surface gradient $\nabla^\Gamma = \boldsymbol{P} \cdot \nabla$, as well as relations (3.29) and (3.30), we obtain the following balance of momentum across the culture boundary:

Remark 4.3. *Considering the boundary of the cell culture as a thin shell and assuming a linear relationship between the bending moment tensor $\boldsymbol{m}$ and the mean curvature H, the following balance of momentum across the boundary follows:*

$$(\boldsymbol{\sigma} + p_{medium}\boldsymbol{I}) \cdot \boldsymbol{n} = \kappa \nabla^{\Gamma} \cdot \left(\boldsymbol{n} \otimes \nabla^{\Gamma} H\right) \qquad \text{on } \partial\Omega_{cult}(t) \times [0, T).$$

As already mentioned, we have not specified the stress tensor $\boldsymbol{\sigma}$ used in Model 4.2 so far. In general, $\boldsymbol{\sigma}$ could depend on the material velocity $\boldsymbol{v}$ as well as on the material displacement $\boldsymbol{u}$, or rather their gradients. Due to cell culture growth, we would expect large displacements $\boldsymbol{u}$ and especially large displacement gradients. However, these might not coincide with large stresses, since the displacements are mainly due to growth. This raises the question: *deformations with respect to what?* (Ambrosi and Mollica, 2002). In the case of small growth and small displacements, we could use the theory of linear thermo-elasticity (Landau and Lifschitz, 1991). However, here we expect large growth and therefore cannot apply a linear theory.

Restricting ourselves to the solely elastic case, we derive in Section 4.2.2 an appropriate stress tensor based on the multiscale analysis outlined in Chapter 2. In Section 4.2.4, we then generalise this ansatz to Maxwell's viscoelastic theory, which in many cases seems to be a more appropriate description of cell cultures (Forgacs et al., 1998).

4.2.2 Multiscale derivation of the stress tensor

A popular approach for the description of growing cell cultures are cellular automaton models. Among them the most promising are off-lattice models (often referred to as individual based models), where the basic units are single cells. Cells are typically modelled as deformable quasi-spherical (e.g. Drasdo and Höhme, 2005) or as ellipsoidal (e.g. Palsson and Othmer, 2000) particles. The deformation of a cell culture is solely determined via the interaction of the discrete cells, usually given in an energetic description.

Based on a cellular automaton approach, Drasdo (2005) has derived a macroscopic description of growing cell cultures in the framework of reaction-diffusion systems by computational means. Drasdo compared computations of reaction-diffusion equations and off-lattice cellular automata model to determine coefficients and functional dependencies of the continuous reaction-diffusion systems. However, this approach is not rigorous and makes a priori assumptions on the approximating continuum model. Here, we show how to derive rigorously a continuum model based on a discrete description without any a priori assumptions on the structure of the continuum model. To do so, we restrict ourselves without loss of generality to a two-dimensional cell culture.

Multiscale derivation of continuous energy functionals

Let us first consider a quasi-static discrete cell culture, where the mechanics are given by energy functionals. From such a discrete description a continuum model can be derived as we have shown in Chapter 2. To do so, we consider the two-dimensional idealised cell culture shown in Fig. 4.4 which satisfies:

Assumption 4.4.

- *For simplicity, the cell culture is two-dimensional.*
- *Cells tightly adhere to each other in a hexagonal manner.*
- *By definition, the size of the cells is given such that the centre of a link between two cells is at the point of contact of the two cells, i.e. at the adhesion site of the two cells.*
- *The elastic response of the cell culture is due to the cytoskeleton, modelled as springs with rest lengths $\hat{\mathcal{L}}_{i,\boldsymbol{\xi}}(t)$. The mechanical interactions are determined by the energies*

$$f_{link}(\mathcal{L}_{i,\boldsymbol{\xi}}(t)/\hat{\mathcal{L}}_{i,\boldsymbol{\xi}}(t)) = k_{link}\left(\frac{\mathcal{L}_{i,\boldsymbol{\xi}}(t)-\hat{\mathcal{L}}_{i,\boldsymbol{\xi}}(t)}{\hat{\mathcal{L}}_{i,\boldsymbol{\xi}}(t)}\right)^2.$$

  Here, $\boldsymbol{\xi}$ is the vector in the reference configuration of the link between two cells and $\mathcal{L}_{i,\boldsymbol{\xi}}(t)$ its length in the deformed configuration at time t.
- *Growth of cell i implies growth of the rest lengths $\hat{\mathcal{L}}_{i,\boldsymbol{\xi}}(t)$, i.e.*

$$\hat{\mathcal{L}}_{i,\boldsymbol{\xi}}(t) = \gamma(i,\boldsymbol{\xi};t)\hat{\mathcal{L}}_{i,\boldsymbol{\xi}}(0) = \gamma(i,\boldsymbol{\xi};t)\varepsilon,$$

  where the initial rest length $\hat{\mathcal{L}}_{i,\boldsymbol{\xi}}(0)$ is given by the network spacing ε. Growth may be anisotropic, i.e. $\gamma(i,\boldsymbol{\xi};t)$ may depend on $\boldsymbol{\xi}$. Division of cells is not considered explicitly.
- *Growth is typically continuous and hence can be considered to be locally constant. Here, we restrict ourselves to constant growth, i.e. $\gamma(i,\boldsymbol{\xi};t) \equiv \gamma(\boldsymbol{\xi};t)$ does not depend on i. Symmetry requires $\gamma(i,\boldsymbol{\xi};t) = \gamma(i+\boldsymbol{\xi},-\boldsymbol{\xi};t)$.*
- *Time scales of growth and mechanics can be clearly distinguished, i.e. we assume that the mechanics are in a quasi-steady state.*

Assumption 4.4 implies a solely elastic cell culture which is at any time in a static state. Any mechanical response is solely due to the cytoskeleton of the cell. In a "realistic" setting also the mechanics of the membrane as well as a compressible cytosol should be taken into account.

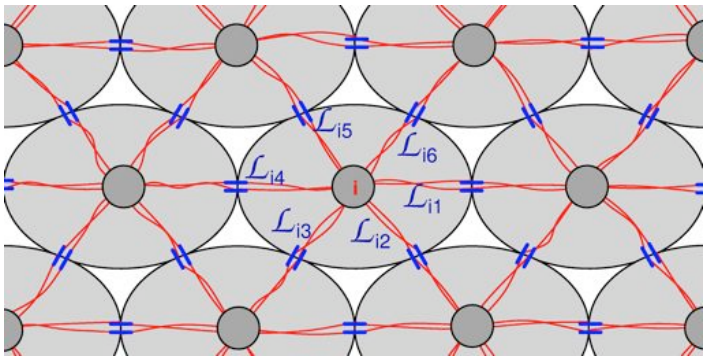

Fig. 4.4. A simple cellular-automaton-like model for mechanical interactions of cells. Each cell consists of six cytoskeletal fibres $\boldsymbol{\xi}$ with lengths $\mathcal{L}_{i,\boldsymbol{\xi}}/2$ anchored on one side at the adhesion points of the cells and on the other side at the cell centre (cell nucleus). Links between two cells, which are considered in the model, consist of the two cytoskeletal fibres connecting the corresponding nuclei.

For a given evolution law of growth $\gamma(\boldsymbol{\xi};t)$, we consider the following microscopic model for the cell culture:

Model 4.5. *Let us consider a cell culture satisfying Assumption 4.4, as shown in Fig. 4.4. Then for any time $t \in [0,T)$, $T>0$ fixed, the quasi-steady state mechanics are determined by the following energy functional*

$$F_{\varepsilon,culture}(t) = \sum_{i\in cells}\sum_{\boldsymbol{\xi}\in fibres} \varepsilon^2\frac{\sqrt{3}}{4} f_{link}\left(\frac{\mathcal{L}_{i,\boldsymbol{\xi}}(t)}{\varepsilon\gamma(\boldsymbol{\xi};t)}\right), \tag{4.3}$$

i.e. the deformation of the cell culture is given by minimisers of the energy $F_{\varepsilon,culture}(t)$.

The factor $\varepsilon^2\sqrt{3}/4$ accounts for the geometrical scaling, as well as the fact that each link is actually counted twice (consists of two cytoskeletal fibres). Similarly to energy (3.8) in Assumption 3.2, it is possible to introduce also an energy which accounts for the compressibility of the cytosol. In analogy to Theorem 3.3, we have:

Theorem 4.6. *Let us consider the discrete Model 4.5. The discrete energies $F_{\varepsilon,culture}(t)$ Γ-converge in the limit $\varepsilon\to 0$ to a continuous energy functional $F_{culture}(t)=\int_\Omega \Psi(t)d\mu$. The energy density Ψ is given by the following homogenisation formula:*

$$\Psi(t) = \sum_{i=1\ldots6} f_{link}\left(|\boldsymbol{F}(t)\cdot\boldsymbol{\xi}_i|/\gamma(\boldsymbol{\xi}_i;t)\right), \tag{4.4}$$

where $\boldsymbol{F}(t)$ is the deformation gradient and $\boldsymbol{\xi}_i\in\mathcal{G}^{\boldsymbol{\xi}}$ are the undeformed fibre vectors.

Proof. The lengths $\mathcal{L}_{i,\boldsymbol{\xi}}(t)$ in (4.3) can be reformulated in terms of finite difference quotients $D_\varepsilon^{\boldsymbol{\xi}}\boldsymbol{\chi}$ (see Section 2.1):

$$\mathcal{L}_{i,\boldsymbol{\xi}}(t) = |D_\varepsilon^{\boldsymbol{\xi}}\boldsymbol{\chi}|\varepsilon.$$

We have assumed, that the energies $f_{\text{link}}(|\cdot|/\gamma(\boldsymbol{\xi};t)\varepsilon)$ are convex functions with 2-growth and thus they satisfy Assumption 2.1. They depend however on the direction of interaction $\boldsymbol{\xi}$, or rather on $\gamma(\boldsymbol{\xi};t)$, opposed to the ones outlined in expression (2.2). But as already discussed in Section 2.1, all arguments in the proofs of Section 2.3 hold also for pair interactions dependent on the direction of interaction (see also Alicandro and Cicalese, 2004). Therefore, the proof follows directly from Theorem 2.6. □

Proposition 2.11 holds also in the case of growing materials if the timescale of mechanics is faster than the timescale of growth (Di Carlo and Quiligotti, 2002; Ambrosi and Guana, 2005), such that the energy density $\Psi(t)$ can be considered as a constitutive relation and corresponding stress tensors can be derived. In general, the stress tensors reflect the underlying symmetries as in the case of red blood cells (see Section 3.2.5). Such a symmetry might not be realistic from a biophysical viewpoint. Hence, some averaging would be necessary.

The mechanics of growing cell cultures are far more complicated and less understood than the mechanics of red blood cells. Therefore, the multiscale analysis bridging the gap between discrete and continuous models has only an illustrative character: it shows the structure of appropriate continuum equations, but it is not yet possible to extract coefficients from the microscopic theory in a quantitative way. Our approach shows that a description via an elastic theory, alternatively viscoelastic theory, as it will be discussed in Section 4.2.4, is probably more appropriate than a characterisation via reaction-diffusion systems as proposed by Drasdo (2005). In addition, this approach yields some information on underlying material laws.

Notion of multiple natural configurations

To classify the continuous energetic description (4.4) in Theorem 4.6 within the existing literature, let us shortly review the notion of multiple natural configurations. It has been originally introduced for modelling problems in thermo-elasticity and elasto-plasticity (Lubarda, 2004). As a description of biological growth it has been first introduced by Rodriguez et al. (1994). The main idea is to decompose the deformation tensor $\boldsymbol{F}$ into two consecutive deformations (see also Fig. 4.5):

$$\boldsymbol{F} = \boldsymbol{F}^{\text{m}} \cdot \boldsymbol{G}.$$

Considering growth phenomena, the tensor $\boldsymbol{G}$, which is assumed to be invertible, is a map from a reference state, e.g. the initial force-free configuration, to the current natural, i.e. force-free, configuration. The tensor $\boldsymbol{G}$ can be directly related to growth. $\boldsymbol{F}^{\text{m}}$ is the deformation tensor due to mechanics. Hence, the stress tensor $\boldsymbol{\sigma}$ should depend on $\boldsymbol{F}^{\text{m}}$ rather than on $\boldsymbol{F}$. Similarly, the "mechanical"energies should depend on $\boldsymbol{F}^{\text{m}}$. Here, it has been assumed that the natural state, which is reached upon unloading from the current configuration, is unique. A consequence of this assumption

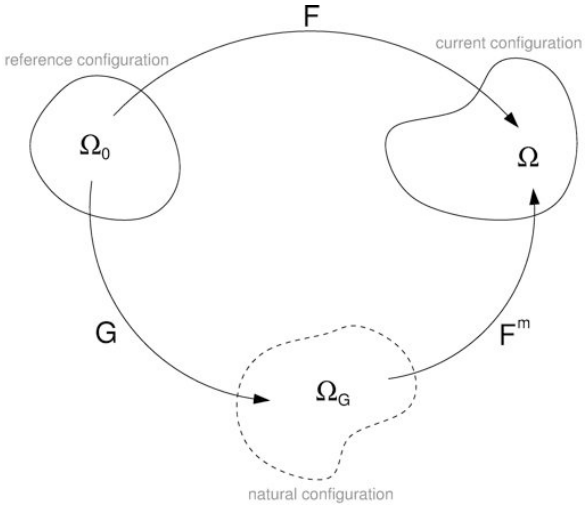

Fig. 4.5. The multiplicative decomposition of the deformation gradient $\boldsymbol{F} = \boldsymbol{F}^{\mathrm{m}} \cdot \boldsymbol{G}$

is that the density field in the natural configuration is identical to the density field in the original reference configuration (Ambrosi and Mollica, 2002). In addition, it is typically assumed that the constitutive relation of the stress tensor $\boldsymbol{\sigma}$, i.e. the relation between stress and mechanical deformation $\boldsymbol{F}^{\mathrm{m}}$, is independent of growth.

Let us revisit our discrete (4.3), and accordingly continuous (4.4), energy functionals and try to reformulate them in a similar manner as the approach of multiple natural configurations. To do so, we further assume that the growth of the cytoskeleton, and hence of the cell, is such that it does not induce additional mechanical energy. The three factors $\gamma(\boldsymbol{\xi}_{1/4}; t)$, $\gamma(\boldsymbol{\xi}_{2/5}; t)$, and $\gamma(\boldsymbol{\xi}_{3/6}; t)$ are not independent of each other. Since we have restricted ourselves to the two-dimensional case, we have only two free parameters. Without loss of generality let us consider the two free parameters $\gamma(\boldsymbol{\xi}_1; t) = \gamma_1(t)$ and $\gamma(\boldsymbol{\xi}_2; t) = \gamma(\boldsymbol{\xi}_3; t) = \gamma_2(t)$.

This allows us the reformulation in terms of a growth tensor, i.e.

$$\gamma(\boldsymbol{\xi}_i; t) = \boldsymbol{G}(t) \cdot \frac{\boldsymbol{\xi}_i}{|\boldsymbol{\xi}_i|}$$

with

$$\boldsymbol{G}(t) = \boldsymbol{\Phi}^T \cdot \begin{pmatrix} \gamma_1(t) & 0 \\ 0 & \sqrt{\frac{4}{3}\gamma_2(t)^2 - \frac{1}{3}\gamma_1(t)^2} \end{pmatrix} \cdot \boldsymbol{\Phi}$$

and a rotation $\boldsymbol{\Phi}$ around an angle ϕ. Let us assume that ϕ is chosen such that after rotation $\frac{\boldsymbol{\xi}_i}{|\boldsymbol{\xi}_i|} = (\cos(-2\pi/6(i-1)), \sin(-2\pi/6(i-1)))$ for $i = 1 \ldots 6$. The energy f_{link} in Model 4.5 depends on $\mathcal{L}_{i,\boldsymbol{\xi}}(t)/\hat{\mathcal{L}}_{i,\boldsymbol{\xi}}(t) - 1$. Assuming that the growth tensor $\boldsymbol{G}$ is

invertible, we conclude

$$\begin{aligned}\frac{(\mathcal{L}_{i,\boldsymbol{\xi}})}{(\hat{\mathcal{L}}_{i,\boldsymbol{\xi}_i})} &= \frac{(\boldsymbol{F}\cdot\boldsymbol{\xi})^T\cdot(\boldsymbol{F}\cdot\boldsymbol{\xi})}{(\boldsymbol{G}\cdot\boldsymbol{\xi})^T\cdot(\boldsymbol{G}\cdot\boldsymbol{\xi})}\\ &= \frac{(\boldsymbol{F}\cdot\boldsymbol{G}^{-1}\cdot\boldsymbol{G}\cdot\boldsymbol{\xi})^T\cdot(\boldsymbol{F}\cdot\boldsymbol{G}^{-1}\cdot\boldsymbol{G}\cdot\boldsymbol{\xi})}{(\boldsymbol{G}\cdot\boldsymbol{\xi})^T\cdot(\boldsymbol{G}\cdot\boldsymbol{\xi})}\\ &= \frac{(\boldsymbol{G}\cdot\boldsymbol{\xi})^T\cdot(\boldsymbol{F}\cdot\boldsymbol{G}^{-1})^T\cdot(\boldsymbol{F}\cdot\boldsymbol{G}^{-1})\cdot(\boldsymbol{G}\cdot\boldsymbol{\xi})}{(\boldsymbol{G}\cdot\boldsymbol{\xi})^T\cdot(\boldsymbol{G}\cdot\boldsymbol{\xi})}\end{aligned}$$

and hence

$$\frac{(\mathcal{L}_{i,\boldsymbol{\xi}})}{(\hat{\mathcal{L}}_{i,\boldsymbol{\xi}_i})} = \frac{\hat{\boldsymbol{\xi}}^T}{|\hat{\boldsymbol{\xi}}|}\cdot(\boldsymbol{F}\cdot\boldsymbol{G}^{-1})^T\cdot(\boldsymbol{F}\cdot\boldsymbol{G}^{-1})\cdot\frac{\hat{\boldsymbol{\xi}}^T}{|\hat{\boldsymbol{\xi}}|}, \tag{4.5}$$

where $\hat{\boldsymbol{\xi}} = \boldsymbol{G}\cdot\boldsymbol{\xi}$ is the link-vector in the grown configuration. For notational convenience, we have dropped the dependence on t above.

Isotropic growth: In the case of isotropic growth, i.e. $\boldsymbol{G} = \gamma\boldsymbol{I}$, we have $\hat{\boldsymbol{\xi}}/|\hat{\boldsymbol{\xi}}| = \boldsymbol{\xi}/|\boldsymbol{\xi}|$, and hence $\frac{(\mathcal{L}_{i,\boldsymbol{\xi}})^2}{(\hat{\mathcal{L}}_{i,\boldsymbol{\xi}_i})^2} = \boldsymbol{\xi}^T\cdot(\boldsymbol{F}\cdot\boldsymbol{G}^{-1})^T\cdot(\boldsymbol{F}\cdot\boldsymbol{G}^{-1})\cdot\boldsymbol{\xi}$. It follows that the mechanical energies $F_{\varepsilon,\text{culture}}(t)$ and accordingly $F_{\text{culture}}(t)$ depend only on the mechanical deformation tensor $\boldsymbol{F}^{\text{m}} = \boldsymbol{F}\cdot\boldsymbol{G}^{-1}$. The stress tensor $\boldsymbol{\sigma}$ is a function of $\boldsymbol{F}^{\text{m}}$ as postulated by the notion of multiple natural configurations.

Anisotropic growth: Considering our relatively simple setup (Fig. 4.4) in the case of anisotropic growth, there is however a difference between our approach and the typical approaches in the framework of multiple natural configurations (e.g. Ambrosi and Guana, 2005). Rewriting relation (4.5) in terms of mechanical deformations $\boldsymbol{F}^{\text{m}} = \boldsymbol{F}\cdot\boldsymbol{G}^{-1}$, we obtain

$$\frac{\mathcal{L}_{i,\boldsymbol{\xi}}}{\hat{\mathcal{L}}_{i,\boldsymbol{\xi}_i}} = \frac{\hat{\boldsymbol{\xi}}^T}{|\hat{\boldsymbol{\xi}}|}\cdot(\boldsymbol{F}^{\text{m}})^T\cdot\boldsymbol{F}^{\text{m}}\cdot\frac{\hat{\boldsymbol{\xi}}^T}{|\hat{\boldsymbol{\xi}}|}.$$

In the case of multiple natural configurations, the energy / stress tensor should solely depend on $\boldsymbol{F}^{\text{m}}$. Since $\hat{\boldsymbol{\xi}} = \boldsymbol{G}\cdot\boldsymbol{\xi}$ still depends on $\boldsymbol{G}$, also the energies $F_{\varepsilon,\text{culture}}$ and F_{culture}, alternatively the corresponding stress tensors, would depend on $\boldsymbol{G}$ in general. Growth also influences the constitutive relation. Typically, this is neglected in approaches using the framework of multiple natural configurations. However, already our very simple idealised cell culture shows that an adaptation of the material should be considered in biological systems in the case of anisotropic growth.

Remark 4.7. *In the case of* isotropic growth*, i.e.* $\boldsymbol{G} = \gamma \boldsymbol{I}$*, the mechanical energy and hence the stress tensor* $\boldsymbol{\sigma}$ *depend on the mechanical deformation tensor* $\boldsymbol{F}^m = \boldsymbol{F} \cdot \boldsymbol{G}^{-1}$ *rather than on the true deformation tensor* $\boldsymbol{F}$*. This is in perfect agreement with the so-called notion of multiple natural configurations (Rodriguez et al., 1994; Ambrosi and Mollica, 2002; Lubarda, 2004).*

In the case of anisotropic growth *it becomes clear that it is necessary to consider not only the "right" deformations, i.e.* $\boldsymbol{\sigma}(\boldsymbol{F}^m)$*, but also an evolution of the constitutive relations. That is, growth implies often also remodelling of the material. The latter is typically neglected and assumed to be independent of growth. But as our simple example shows, remodelling is important in growing biological systems and should be considered in the case of anisotropic growth. The multiscale approach indicates how remodelling might influence the constitutive relations.*

For the rest of this chapter, we restrict ourselves to isotropic growth. This implies that the constitutive relations do not evolve. Because modelling single components of our idealised cell culture would be not more than vague speculation, we prefer to work at the moment with typical constitutive relations proposed in the literature rather than with stress tensors based on a multiscale approach. Nevertheless, the multiscale approach will become very useful once better experimental data is available. In the following, we consider a Blatz-Ko (1962) material as proposed by Ambrosi and Mollica (2002) modelling tumour growth:

$$\boldsymbol{\sigma} = \frac{\mu}{\det \boldsymbol{F}^m} \left(\boldsymbol{F}^m \cdot \boldsymbol{F}^{mT} - (\det \boldsymbol{F}^m)^q \boldsymbol{I} \right) \tag{4.6}$$

with constants μ and $q < 0$. Here, μ it the shear modulus and the constant q can be related to the bulk modulus K:

$$K = (1 - q)\mu.$$

4.2.3 Evolution of growth

Often, it is much more convenient to describe growth in terms of growth rates, rather than growth tensors. To relate both, let us consider a given evolution of the growth tensor $\boldsymbol{G}(t)$. Considering only growth and no mechanical deformations, i.e. $\boldsymbol{F}^{\mathrm{m}}(t) \equiv \boldsymbol{I}$ and hence $\boldsymbol{F}(t) = \boldsymbol{G}(t)$, we obtain the following relationship between the initial volume of the cell $dV_{\mathrm{cell}}(0)$ and its volume $dV_{\mathrm{cell}}(t)$ at time t:

$$dV_{\mathrm{cell}}(t) = (\det \boldsymbol{G}(t)) dV_{\mathrm{cell}}(0).$$

If we restrict our consideration to one cell the assumption $\boldsymbol{F}^{\mathrm{m}}(t) = \boldsymbol{I}$ clearly holds, since we have chosen the setup such that growth does not induce stresses inside the

cell. Assuming further that the density ρ is not influenced by growth, we obtain the following evolution law for the cell mass:

$$\begin{aligned}\frac{dM_{\text{cell}}(t)}{dt} &= \rho\frac{dV_{\text{cell}}(t)}{dt}\\ &= \rho V_{\text{cell}}(0)\frac{d\det \boldsymbol{G}(t)}{dt}\\ &= dM_{\text{cell}}(0)\,\text{tr}\,\boldsymbol{D}_G(t)\det \boldsymbol{G}(t)\end{aligned}$$

and hence

$$\frac{dM_{\text{cell}}(t)}{dt} = dM_{\text{cell}}(t)\,\text{tr}\,\boldsymbol{D}_G(t), \tag{4.7}$$

where we have used $\frac{d}{dt}\det \boldsymbol{G} = \det(\boldsymbol{G})\,\text{tr}\,(\boldsymbol{G}^{-1}\cdot\frac{d}{dt}\boldsymbol{G})$ and the definition $2\boldsymbol{D}_G = (\frac{d}{dt}\boldsymbol{G}\cdot\boldsymbol{G}^{-1})^T + (\frac{d}{dt}\boldsymbol{G}\cdot\boldsymbol{G}^{-1})$ (Ambrosi and Mollica, 2002).

Comparing relation (4.7) with the Lagrangian formulation of mass balance, i.e. with $\frac{d}{dt}dM(t) = dM(t)g(c)$, we recover the following equality

$$\text{tr}\,\boldsymbol{D}_G = g(c). \tag{4.8}$$

Therefore, the growth rate determines at least one of the invariants of the growth tensor. In the case of isotropic growth $\boldsymbol{G}(t) = \gamma(t)\boldsymbol{I}$, the growth tensor is completely determined:

$$\frac{d\gamma(t)}{dt} = \frac{\gamma(t)}{n}g(c), \tag{4.9}$$

where n is the dimension of space.

Relation (4.8), and accordingly relation (4.9), imposes some restrictions on the evolution of the growth tensor $\boldsymbol{G}(t)$ in terms of growth rates. Considering not only quasi-steady state mechanics, as we have done here, further thermodynamical restrictions for the structure of the growth tensor exist (Di Carlo and Quiligotti, 2002).

4.2.4 Maxwell viscoelasticity

In Section 4.2.2, we have derived appropriate constitutive relations for growing cell cultures using techniques from multiscale analysis. To do so, we have assumed that the culture is elastic and that the mechanics are always in a steady state, i.e. the deformations are minimisers of the energy functionals. Although the quasi-static elastic approach is quite often used in the context of growing cell cultures (Ambrosi and Mollica, 2002; Ben Amar and Goriely, 2005), it might not be very realistic in soft tissues. The time scale of growth is quite slow, hence we expect relaxation of stresses due to the viscoelastic nature of cell cultures (Forgacs et al., 1998). The "passive" mechanical

behaviour of cells can be approximated quite well by Maxwell's theory of viscoelasticity on long time scales. In one dimension such a behaviour can be characterised by a spring and a dashpot in series

$$G\sigma + \eta\frac{d\sigma}{dt} = G\eta\frac{d\epsilon}{dt}, \tag{4.10}$$

where G is the modulus of elasticity, η is the modulus of friction, σ is the force / stress, and ϵ is the deformation / strain (Findley, 1976).

To derive an appropriate description in a viscoelastic setting let us drop the assumption of a quasi-steady state adopted in Section 4.2.2. We rather start from a given stress tensor and then derive corresponding viscoelastic laws which will be used for modelling. This approach is only formal and solely based on physical principles, a rigorous treatment is an open problem.

For simplicity, let us assume that growth is isotropic and let the elasticity of the cell culture in the elastic case (i.e. considering experiments on a time scale much faster than stress relaxation) be of a Blatz-Ko (1962) type as discussed above. Of course also stress tensors derived from a multiscale approach as in the case of red blood cells (c.f. Chapter 3) could be considered. But due to our limited knowledge on the microscale we prefer to work with the stress tensor given in (4.6). Additionally, we restrict ourselves for the moment to small mechanical deformations $\boldsymbol{F}^{\mathrm{m}}$. (Attention, $\boldsymbol{F}$ still might be quite large due to growth.) Following the standard derivation of Maxwell's theory of viscoelasticity, we show that our ansatz leads to an additive correction term in the viscoelastic evolution law of the stress tensor.

For the rest of this section, we rely on the following assumptions:

Assumption 4.8.

- *Growth is isotropic, i.e.* $\boldsymbol{G} = \gamma(t)\boldsymbol{I}$.
- *The behaviour of the cell culture in the elastic regime is of a Blatz-Ko (1962) type, i.e.*
$$\boldsymbol{\sigma}_{elastic} = \frac{\mu}{\det \boldsymbol{F}^m}\left(\boldsymbol{F}^m \cdot \boldsymbol{F}^{mT} - (\det \boldsymbol{F}^m)^q \boldsymbol{I}\right). \tag{4.11}$$
- *Mechanical deformations* $\boldsymbol{F}^m$ *are small, i.e.* $|\boldsymbol{F}^m - \boldsymbol{I}| \ll 1$.

Adopting Assumption 4.8 and considering times much smaller than the relaxation time the behaviour of a Maxwell solid is well described by $\boldsymbol{\sigma}_{\mathrm{elastic}}$, given in (4.11), with $\boldsymbol{F}^{\mathrm{m}} = \frac{1}{\gamma}\boldsymbol{F}$. Taking the total time derivative of $\boldsymbol{\sigma}_{\mathrm{elastic}}$ and using $\frac{d}{dt}\det \boldsymbol{F} = \det(\boldsymbol{F})\,\mathrm{tr}\,(\boldsymbol{F}^{-1}\cdot\frac{d}{dt}\boldsymbol{F})$, or rather $\frac{d}{dt}\det \boldsymbol{F} = \det(\boldsymbol{F})\,\mathrm{tr}\,(\boldsymbol{D})$, as well as (4.9), we obtain

$$\begin{aligned}\frac{d\boldsymbol{\sigma}}{dt} =& \frac{\mu}{\det \boldsymbol{F}^{\mathrm{m}}}(g(c) - \mathrm{tr}\,\boldsymbol{D})\left(\boldsymbol{F}^{\mathrm{m}}\cdot\boldsymbol{F}^{\mathrm{m}T} - (\det \boldsymbol{F}^{\mathrm{m}})^q\boldsymbol{I}\right)\\ &+ \frac{\mu}{\det \boldsymbol{F}^{\mathrm{m}}}\left(\boldsymbol{F}^{\mathrm{m}}\cdot\boldsymbol{F}^{\mathrm{m}T}\cdot\boldsymbol{L}^T + \boldsymbol{L}\cdot\boldsymbol{F}^{\mathrm{m}}\cdot\boldsymbol{F}^{\mathrm{m}T} - \frac{2}{n}g(c)\boldsymbol{F}^{\mathrm{m}}\cdot\boldsymbol{F}^{\mathrm{m}T}\right)\\ &- \frac{q\mu}{\det \boldsymbol{F}^{\mathrm{m}}}(\det \boldsymbol{F}^{\mathrm{m}})^q\,(\mathrm{tr}\,\boldsymbol{D} - g(c)),\end{aligned}$$

where n is the dimension under consideration, $\boldsymbol{L} = \nabla \boldsymbol{v}$, and $\boldsymbol{D} = \frac{1}{2}(\boldsymbol{L} + \boldsymbol{L}^T)$. Since we have assumed small deformations, i.e. $|\boldsymbol{F}^{\mathrm{m}} - \boldsymbol{I}| \ll 1$, using relation (4.9) we obtain

$$\frac{\partial \boldsymbol{\sigma}}{\partial t} = 2\mu(\boldsymbol{D} - \frac{1}{n} g(c)\boldsymbol{I}) + (K - \mu)(\mathrm{tr}\,(\boldsymbol{D}) - g(c))\boldsymbol{I} \tag{4.12}$$

in a first order approximation. In analogy to Maxwell viscoelasticity, let us allow for relaxation of stresses by introducing the decay term $-\lambda\boldsymbol{\sigma}$ on the right hand side of evolution law (4.12) with $\lambda = \frac{G}{\eta}$, c.f. relation (4.10). Thus, the following material law is found:

Remark 4.9. *The evolution of the stress tensor for a growing Maxwell viscoelastic material is given by*

$$\frac{d\boldsymbol{\sigma}}{dt} = 2\mu(\boldsymbol{D} - \frac{1}{n} g(c)\boldsymbol{I}) + (K - \mu)(\mathrm{tr}\,(\boldsymbol{D}) - g(c))\boldsymbol{I} - \lambda\boldsymbol{\sigma}, \tag{4.13}$$

where λ is proportional to the relaxation time. We can therefore conclude, that growth appears only as an additive correction in the evolution law for the stress tensor.

A treatment of such viscoelastic laws is even more difficult as the solely elastic case, since it includes additional equations for the evolution of the stress tensor. Therefore, it often makes sense to restrict oneself to the situation of slow relaxation or the situation of fast relaxation. Neglecting relaxation, i.e. in the limit of slow relaxation, the stress tensor $\boldsymbol{\sigma}$ is given by the "standard" elasticity tensor (4.11). In the limit of fast relaxation, we can neglect the time derivative in (4.13) and have the following "fluid-type" stress tensor:

$$\boldsymbol{\sigma} = \frac{2\mu}{\lambda}(\boldsymbol{D} - \frac{1}{n} g(c)\boldsymbol{I}) + \frac{K - \mu}{\lambda}(\mathrm{tr}\,(\boldsymbol{D}) - g(c))\boldsymbol{I}. \tag{4.14}$$

Choosing $\kappa = \mu$ this definition differs from the stress tensor of a Stokes fluid by the correction terms due to growth. In the case of no growth, expression (4.14) is identical to the stress tensor of a Stokes fluid.

4.2.5 A viscoelastic model in the limit of fast relaxation

In Section 4.2.1, we have outlined a continuum model for growing cell cultures up to a specification of the constitutive relations as well as the kinetics. Let us now specify these with respect to a typical experimental setup considered in branching morphogenesis (Hartmann and Miura, 2006). In addition to Assumption 4.1 the following assumptions are made.

Assumption 4.10.

- *Mechanics of the cell culture are viscoelastic with a relaxation time much faster than the time scale of growth, i.e. we consider the "fluid-like" stress tensor* (4.14)*.*
- *The diffusion coefficient D is linear. Kinetics are given by $f(c) = Fc$ and $g(c) = Gc$.*
- *Inertial terms and body forces in the balance of linear momentum* (4.1) *are negligible. We consider only quasi-steady states.*

Since we do not aim at predicting quantitative properties so far, we should take the simplest kinetics f and g reproducing the results qualitatively. Therefore, we assume simple linear mass action laws. For the same reasons, we choose D to be constant in the whole domain Ω. So far we have not specified the spatial dimension n. Typical experiments involve cell culture growth in two or three dimensions. The analysis performed in the next chapter is based on the case $n = 2$.

Inserting the balance of mass into the balance of linear momentum in Model 4.2 and using $\rho = \text{const.}$ the balance of linear momentum reads

$$\rho\big(\frac{\partial}{\partial t}\boldsymbol{v} + \boldsymbol{v}\cdot\nabla\boldsymbol{v}\big) = \nabla\cdot\boldsymbol{\sigma}.$$

Neglecting inertia terms and using Assumption 4.10, Model 4.2 reads:

Model 4.11. *Let Assumption 4.1 and 4.10 be true. Then the evolution of a growing cell culture is described by the following set of equations (for some fixed time $T > 0$):*

$$\begin{aligned}
\rho\nabla\cdot\boldsymbol{v} &= \rho Gc && \text{in } \Omega_{cult}(t)\times[0,T),\\
0 &= \nabla\cdot\boldsymbol{\sigma} && \text{in } \Omega_{cult}(t)\times[0,T),\\
\frac{\partial}{\partial t}c - \nabla\cdot(D\nabla c) &= -\chi_{\Omega_{cult}}\rho f(c) && \text{in } \Omega\times[0,T),
\end{aligned}$$

with the balance of momentum across the culture boundary

$$(\boldsymbol{\sigma} + p_{medium}\boldsymbol{I})\cdot\boldsymbol{n} = -\kappa H\boldsymbol{n} \qquad \text{on } \partial\Omega_{cult}(t)\times[0,T)$$

and stress tensor

$$\boldsymbol{\sigma} = -p\boldsymbol{I} + \frac{2\mu}{\lambda}(\boldsymbol{D} - \frac{1}{n}Gc\boldsymbol{I}),$$

where p is the pressure of the culture due to incompressibility. The evolution of $\Omega_{cult}(t) \subset \Omega$ is given by the normal speed of the culture boundary

$$V_n = \boldsymbol{n}\cdot\boldsymbol{v} \qquad \text{on } \partial\Omega_{cult}(t)\times[0,T).$$

Furthermore, zero-flux boundary conditions for the chemical c are imposed on $\partial\Omega$. Initial conditions are $\boldsymbol{v}(\boldsymbol{x};0) = 0$, $c(\boldsymbol{x};0) = c_0$ constant, and a compact $\Omega_{cult}(0)$.

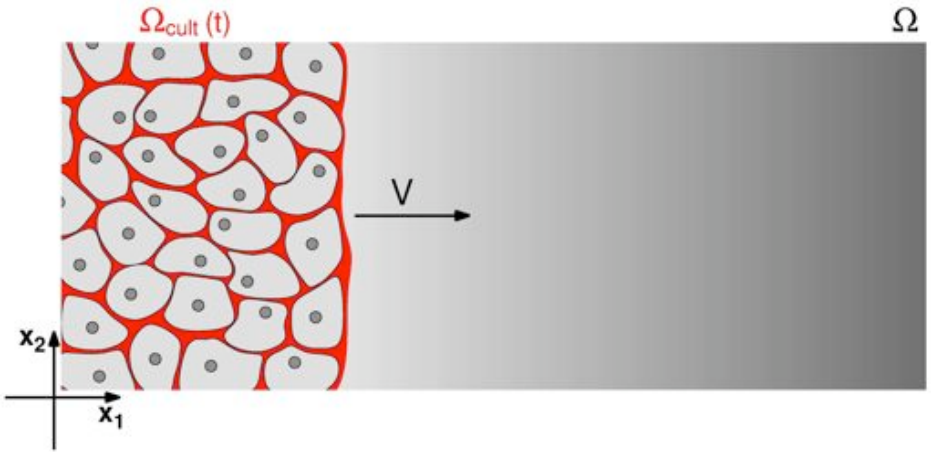

Fig. 4.6. A plane wave in an infinite domain $\Omega = \mathbb{R}^2$. The gradient encodes growth factor concentration c_0.

In the following, we use $\mu^\star = \mu/\lambda$ for notational convenience. Simulations of Model 4.11 are beyond the scope of this thesis. Here, we restrict ourselves to an analytical investigation of the instabilities leading to branch structures. Although all terms in Model 4.11 are linear, the model is nonlinear with the nonlinearity coming from the free boundary. This nonlinearity makes the equations rather hard to study. Nevertheless, some results can be obtained as shown in the next section.

4.3 Analysis

Investigating partial differential equations, it is often beneficial to look for specific solutions which reflect various symmetries of the equations. In the following, we investigate plane waves:

Definition 4.12 (Evans, 1998)**.** *A solution* $\boldsymbol{u}$ *of a partial differential equation in the* $n+1$ *variables* $\boldsymbol{x} = (x_1, \dots x_n) \in \mathbb{R}^n$, $t \in \mathbb{R}$ *having the form*

$$\boldsymbol{u}(\boldsymbol{x}, t) = \boldsymbol{v}(\boldsymbol{y} \cdot \boldsymbol{x} - Vt) \qquad (\boldsymbol{x} \in \mathbb{R}^n, t \in \mathbb{R})$$

is called a travelling wave *or* plane wave *with a* wavefront *normal to* $\boldsymbol{y} \in \mathbb{R}^n$ *(*$|\boldsymbol{y}| = 1$*), velocity* V*, and profile* $\boldsymbol{v}$*.*

In the case of isotropy and homogeneity one can fix $\boldsymbol{y}$ without loss of generality. Let us assume $\boldsymbol{y} = (1, 0, \dots)$, i.e. a plane wave in the x_1-direction. For Model 4.11 explicit plane wave solutions can be constructed (Section 4.3.1). In Section 4.3.2, we investigate their linear stability. The corresponding dispersion relations (relation between growth rate and wavelength of a perturbation) show that the travelling waves exhibit a front instability, which can lead to branch patterns.

For the rest of this chapter, we consider for simplicity a two-dimensional setup $\Omega \subset \mathbb{R}^2$ as shown in Fig. 4.6. Often a two-dimensional description of a growing cell culture is sufficient, e.g. in the case of lung cells cultured *in vitro* (Miura and Shiota, 2002). Therefore, let us consider the following model (c.f. Model 4.11):

Model 4.13. *Considering an infinite domain $\Omega = \mathbb{R}^2$ as shown in Fig. 4.6, Model 4.11 reads (for some fixed time $T > 0$):*

$$\begin{aligned} \rho \nabla \cdot \boldsymbol{v} &= \rho G c && \text{in } \Omega_{cult}(t) \times [0,T), \\ 0 &= \nabla \cdot \boldsymbol{\sigma} && \text{in } \Omega_{cult}(t) \times [0,T), \\ \frac{\partial}{\partial t} c - D\Delta c &= -\chi_{\Omega_{cult}} \rho f(c), && \text{in } \mathbb{R}^2 \times [0,T), \end{aligned} \tag{4.15}$$

with the balance of momentum across the culture boundary

$$(\boldsymbol{\sigma} + p_{medium}\boldsymbol{I}) \cdot \boldsymbol{n} = -\kappa H \boldsymbol{n} \qquad \text{on } \partial\Omega_{cult}(t) \times [0,T)$$

and the asymptotic behaviour

$$\lim_{x_1 \to +\infty} \boldsymbol{c} = c_0, \qquad \lim_{x_1 \to -\infty} \boldsymbol{c} = 0, \qquad \lim_{x_1 \to -\infty} \boldsymbol{v} = 0. \tag{4.16}$$

4.3.1 Existence of plane waves

Many reaction-diffusion systems are well known to exhibit plane wave / travelling wave solutions (Heinze, 1987). As the following proposition shows, this is also the case for Model 4.11, and accordingly Model 4.13. Given a constant wave speed V, we know a priori the evolution of the free boundary. This eliminates the nonlinearity of the models (the coupling of the equations with the free boundary) and plane wave solutions can be calculated explicitly.

Proposition 4.14. *Let $c_0 = \frac{F}{G}$ be true and let the front pass $\boldsymbol{x} = 0$ at time $t = 0$. Then for any given wave speed V, bounded plane wave solutions of Model 4.11 exist and can be calculated explicitly:*

$$\begin{aligned} c^{TW}(\xi) &= \begin{cases} \frac{2c_0 V}{V+\sqrt{V^2+4FD}} \exp\left(\frac{-V+\sqrt{V^2+4FD}}{2D}\xi\right) & \xi \le 0 \\ c_0 + \left(\frac{2c_0 V}{V+\sqrt{V^2+4FD}} - c_0\right) \exp\left(-\frac{V}{D}\xi\right) & \text{else,} \end{cases} \\ \boldsymbol{v}^{TW}(\xi) &= V \exp\left(\frac{-V+\sqrt{V^2+4FD}}{2D}\xi\right) && \xi \le 0, \\ p^{TW}(\xi) &= \frac{2\mu c_0 G V}{V+\sqrt{V^2+4FD}} \exp\left(\frac{-V+\sqrt{V^2+4FD}}{2D}\xi\right) && \xi \le 0, \end{aligned} \tag{4.17}$$

with $\xi = (1,0) \cdot \boldsymbol{x} - Vt$ and $\Omega_{cult} = \{\xi = \boldsymbol{y} \cdot \boldsymbol{x} - Vt < 0\}$.

Proof. Transforming Model 4.13 to a moving coordinate system and considering plane wave solutions, i.e. considering $\boldsymbol{v}(\boldsymbol{x},t) = \boldsymbol{v}((1,0)\cdot\boldsymbol{x} - Vt)$ and $c(\boldsymbol{x},t)$, $p(\boldsymbol{x},t)$ similar, the system (4.15) simplifies to

$$\begin{aligned} -V\frac{\partial c^{\mathrm{TW}}}{\partial \xi} &= D\frac{\partial^2 c^{\mathrm{TW}}}{\partial \xi^2} c^{\mathrm{TW}} - \chi_{\mathbb{R}^-}\, F c^{\mathrm{TW}} && \text{in } \mathbb{R}, \\ \frac{\partial v_1^{\mathrm{TW}}}{\partial \xi} &= G c^{\mathrm{TW}} && \text{in } \mathbb{R}^-, \\ 0 &= -\frac{\partial p^{\mathrm{TW}}}{\partial \xi} + \mu^\star \left(\frac{\partial^2 v_1^{\mathrm{TW}}}{\partial \xi^2} - G\frac{\partial c^{\mathrm{TW}}}{\partial \xi} \right) && \text{in } \mathbb{R}^-. \end{aligned} \tag{4.18}$$

Splitting the first equation in (4.18) into one part inside the culture ($\xi \in \mathbb{R}^-$) and one part outside the culture ($\xi \in \mathbb{R}^+$), the system of ordinary differential equations can be integrated explicitly. Requiring continuity of concentration and fluxes of the growth factor across the culture interface ($\xi = 0$) together with the boundary conditions (4.16), the travelling wave solutions (4.17) are recovered.

The material speed at the front should equal the speed of the travelling wave, i.e. $(V, 0) = \boldsymbol{v}^{\mathrm{TW}}(0)$. This implies

$$c_0 = \frac{F}{G}, \tag{4.19}$$

which we call in the following the *plane wave condition*: given a set of parameters (F, G, ρ) only for one initial concentration of chemicals c_0 plane waves exist. □

Above, we have proven that travelling waves with an arbitrary speed V exist if the plane wave condition (4.19) is fulfilled. The issue whether solutions of a one-dimensional version of Model 4.13 converge to plane waves or not has not been addressed. This question as well as the question of the selected wave speed are of importance and should be considered in the future. Here, we have restricted ourselves to linear kinetics, since in this case explicit solutions can be obtained. Being not interested in explicit solutions, it is possible to consider a wider class of kinetics and prove the existence of travelling waves (Dockery and Klapper, 2001; Hartmann and Miura, 2007).

4.3.2 Stability analysis of plane waves

In this section, we investigate the stability of plane wave solutions (4.17) of Model 4.13 with respect to small perturbations of the front, i.e. $x_1 = Vt + \delta(x_2, t)$ with $\delta \ll 1$. If the front is unstable to such perturbations, the model can account for branching morphogenesis.

Any sufficiently regular perturbation $\delta(x_2, t)$ of the plane wave front can be decomposed into spatial Fourier components. The Fourier components are periodic in

space, but generally the periodicity is not conserved. However within a linear theory, i.e. for small perturbations, the periodicity can be assumed to be conserved. By superposition, we can restrict our analysis to one wavenumber k.

Assumption 4.15.

- *The interface of the culture moving in direction* $\boldsymbol{y} = (1, 0)$ *with speed* V *is slightly perturbed, i.e.*

$$\Omega_{cult}(t) = \{\boldsymbol{x} = (x_1, x_2) \in \Omega : x \leq Vt + \delta \exp(\theta t) \exp(ikx_2) + O(\delta^2)\}$$

with $\delta \ll 1$.

This assumption allows us to consider only first order approximations in δ and to drop all contributions from terms of the order $O(\delta^2)$, i.e. we work within a linear theory. Under this assumption the evolution of the perturbation can be characterised explicitly for small times:

Proposition 4.16. *Let Assumption 4.15 be true and* c^{TW}, $\boldsymbol{v}^{TW}$, p^{TW} *the plane wave solution* (4.17) *of Model 4.14 with the interface* $\partial\Omega_{cult} = \{\boldsymbol{y} \cdot \boldsymbol{x} - Vt = 0\}$. *Then, for short times the evolution of a small and sufficiently smooth perturbation of the interface is given by*

$$\partial\Omega_{cult}(0) = \left\{ x_1 - \left(Vt + \int_{\mathbb{R}} \delta(k, t) \exp(ix_2 k) dk \right) = 0 \right\} \tag{4.20}$$

with

$$\delta(k, t) = \delta(k, 0) \exp(\theta(k)\, t).$$

The exponential growth rate $\theta(k)$ *(not necessarily unique) is determined by the dispersion relation*

$$\begin{aligned} 0 = \quad & -\theta(k) - \frac{\kappa k}{2\mu^\star} + \frac{2VF}{V + \sqrt{V^2 + 4FD}} \\ & + \frac{4c_0 VF}{(\sqrt{V^2 + 4D\theta(k) + 4k^2D^2} + \sqrt{V^2 + 4D\theta(k) + 4k^2D^2 + 4FD})} \\ & \times \frac{F(-V + 2Dk - \sqrt{V^2 + 4D\theta(k) + 4k^2D^2 + 4FD})}{2c_0(F + \theta(k) + Vk)(V + \sqrt{V^2 + 4FD})}. \end{aligned} \tag{4.21}$$

Note, that the growth rate θ still depends on the speed V of the travelling wave, which is a priori not known. The proof of Proposition 4.16 given here is only a formal proof. A rigorous proof is an open problem and should be addressed in the future.

Proof. We have restricted ourselves to small perturbations. By superposition, it is therefore sufficient to consider the evolution of a single Fourier component with

wavenumber k. For notational convenience we drop the dependence on k in the following.

Let us consider the slightly perturbed culture

$$\Omega_{\text{cult}}(t) = \{\boldsymbol{x} = (x_1, x_2) \in \Omega : x \leq Vt + \delta \exp(\theta t) \exp(ikx_2) + O(\delta^2)\}, \tag{4.22}$$

with $\delta \ll 1$. The assumption of exponential growth / decay of perturbations, i.e $\delta(k,t) = \delta(k) \exp(\theta(k)t)$, is reasonable because we are considering basically a linear model. Ansatz (4.22) implies the normal speed of the boundary

$$\begin{aligned} V_n &= \boldsymbol{n} \cdot (V + \delta\theta \exp(\theta t) \exp(ikx_2), 0) + O(\delta^2) \\ &= V + \delta\theta \exp(\theta t) \exp(ikx_2) + O(\delta^2), \end{aligned} \tag{4.23}$$

where $\boldsymbol{n}$ is the outer unit normal, and the mean curvature

$$\begin{aligned} H &= -\frac{\partial^2}{\partial x_2^2} \left[F(t) + \delta \exp(\theta t) \exp(ikx_2) + O(\delta^2)\right] \\ &= k^2 \delta \exp(\theta t) \exp(ikx_2) + O(\delta^2) \end{aligned}$$

of the boundary.

In a linear theory, it is further reasonable to assume that the perturbed travelling wave solutions of Model 4.13 have the same structure as the interface perturbation (4.20). This justifies the following ansatz:

$$\begin{aligned} c(x_1, x_2; t) = &\ c^{\text{TW}}(x_1 - Vt) + \delta c^{\text{PER}}(x_1 - Vt) \exp(\theta t) \exp(ikx_2) + O(\delta^2), \\ \boldsymbol{v}(x_1, x_2; t) = &\ \boldsymbol{v}^{\text{TW}}(x_1 - Vt) + \delta \boldsymbol{v}^{\text{PER}}(x_1 - Vt) \exp(\theta t) \exp(ikx_2) + O(\delta^2), \\ p(x_1, x_2; t) = &\ p^{\text{TW}}(x_1 - Vt) + \delta p^{\text{PER}}(x_1 - Vt) \exp(\theta t) \exp(ikx_2) + O(\delta^2). \end{aligned} \tag{4.24}$$

Plugging ansatz (4.24) into Model 4.13 and considering a moving coordinate system $\xi = x_1 - Vt$, we have at a first order approximation

$$\begin{aligned} \theta c^{\text{PER}} &= D\left(\frac{\partial^2 c^{\text{PER}}}{\partial \xi^2} - k^2 c^{\text{PER}}\right) - \chi_{\Omega_{\text{cult}}(t)} F \rho c^{\text{PER}} && \text{in } \mathbb{R}^2 \times [0,T), \\ 0 &= \frac{\partial v_1^{\text{PER}}}{\partial \xi} + k v_1^{\text{PER}} - G c^{\text{PER}} && \text{in } \Omega_{\text{cult}}(t) \times [0,T), \\ 0 &= -\frac{\partial p^{\text{PER}}}{\partial \xi} + \mu^\star \left(\frac{\partial^2 v_1^{\text{PER}}}{\partial \xi^2} - k^2 v_1^{\text{PER}}\right) && \text{in } \Omega_{\text{cult}}(t) \times [0,T), \\ 0 &= -ikp^{\text{PER}} + \mu^\star \left(\frac{\partial^2 v_2^{\text{PER}}}{\partial \xi^2} - k^2 v_2^{\text{PER}}\right) && \text{in } \Omega_{\text{cult}}(t) \times [0,T)\ . \end{aligned}$$

Splitting up the first equation into one part inside and another outside the culture, the system of ordinary differential equations can be solved explicitly. Together with the continuity of the concentration and the flux of growth factors across the culture

boundary, as well as the boundary conditions (4.16), solutions are approximated up to first order by

$$
\begin{aligned}
c^{\mathrm{PER}}(\xi) =& C_1 \cdot \begin{cases} \exp\left(-\frac{V-\sqrt{V^2+4D\theta+4k^2D^2+4FD}}{2D}\xi\right) & \text{in } \Omega_{\mathrm{cult}}(t)\times[0,T) \\ \exp\left(-\frac{V+\sqrt{V^2+4D\theta+4k^2D^2}}{2D}\xi\right) & \text{otherwise,} \end{cases} \\
v_1^{\mathrm{PER}}(\xi) =& \exp(k\xi)(-C_2+C_3\xi-C_3/k) \\
&+ C_1 G \frac{2DVk^2+(F+\theta)(V+\sqrt{V^2+4D\theta+4k^2D^2+4FD})}{2(F+\theta+Vk)(F+\theta-Vk)} \\
&\qquad \times \exp\left(-\frac{V-\sqrt{V^2+4D\theta+4k^2D^2+4FD}}{2D}\xi\right), \\
v_2^{\mathrm{PER}}(\xi) =& i\exp(k\xi)(-C_2+C_3\xi) \\
&+ iC_1Gk \frac{2D(F+\theta)+V(V+\sqrt{V^2+4D\theta+4k^2D^2+4FD})}{2(F+\theta+Vk)(F+\theta-Vk)} \\
&\qquad \times \exp\left(\frac{-V+\sqrt{V^2+4D\theta+4k^2D^2+4FD}}{2D}\xi\right), \\
p^{\mathrm{PER}}(\xi) =& 2\mu^\star C_3 \exp(k\xi) \\
&+ C_1 G\mu^\star \exp\left(\frac{-V+\sqrt{V^2+4D\theta+4k^2D^2+4FD}}{2D}\xi\right)
\end{aligned}
\tag{4.25}
$$

with constants

$$
\begin{aligned}
C_1 =& \frac{c_0V(V-\sqrt{V^2+4FD})}{D(\sqrt{V^2+4D\theta+4k^2D^2}+\sqrt{V^2+4D\theta+4k^2D^2+4FD})}, \\
C_2 =& \frac{FV}{V+\sqrt{V^2+4FD}} \\
&+\frac{FC_1(2DVk^2+(F+\theta)(V+\sqrt{V^2+4D\theta+4k^2D^2+4FD}))}{2c_0(F+\theta+Vk)(F+\theta-Vk)}, \\
C_3 =& +\frac{\kappa k^2}{2\mu^\star} - \frac{FVk}{V+\sqrt{V^2+4FD}} \\
&+FC_1k\frac{-V+2kD-\sqrt{V^2+4D\theta+4k^2D^2+4FD}}{2c_0(F+\theta+Vk)}.
\end{aligned}
$$

On the culture boundary, the normal material speed $\boldsymbol{n}\cdot\boldsymbol{v}$ should equal the normal speed V_n given by (4.23). This closes our ansatz and yields the dispersion relation (4.21).

Choosing for a given wavenumber k an appropriate growth rate $\theta(k)$ determined by the dispersion relation (4.21), ansatz (4.24) together with (4.25) is a first order approximation of the perturbed plane wave, i.e. the solution is determined up to order δ^2. □

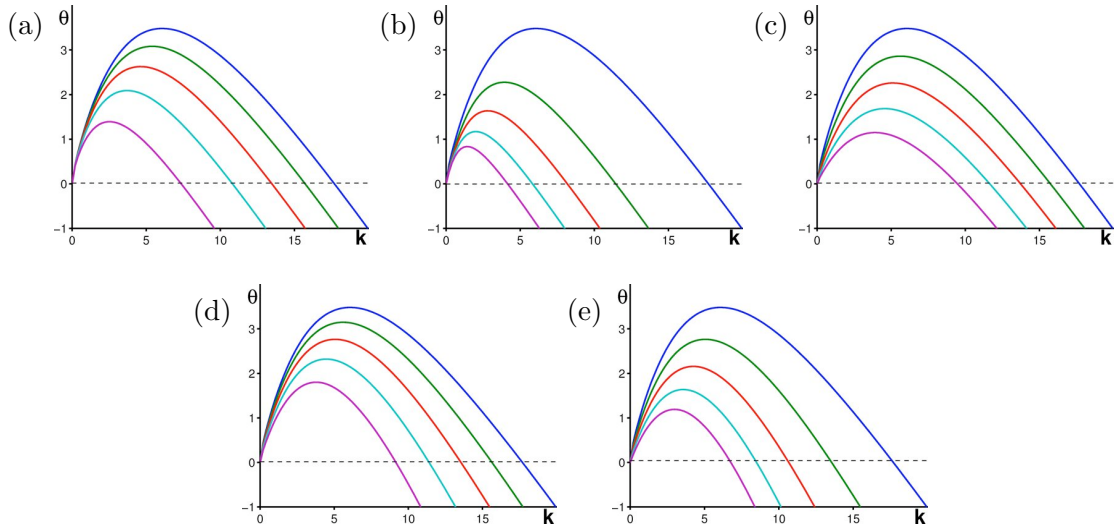

Fig. 4.7. Evaluation of the dispersion relation (4.21) for different parameters: (a) $F = 100.0, 80.0, 60.0, 40.0, 20.0$, (b) $D = 1.0, 2.5, 5.0, 10.0, 20.0$, (c) $V = 1.0, 0.9, 0.8, 0.7, 0.6$, (d) $\mu^\star = 1.0, 0.9, 0.8, 0.7, 0.6$, and (e) $\kappa = 1.00, 1.25, 1.50, 1.75, 2.00$. The order of the parameters is chosen such that growth rates decay. If not varied the parameters are $\rho = 1.0$, $c_0 = 1.0$, $V = 1.0$, $F = 100.0$, $D = 1.0$, $\kappa = 1.0$, and $\mu^\star = 1.0$.

The linear stability analysis above has yielded a dispersion relation, which determines the growth rate θ of periodic interface perturbations with wavenumber k. Because the dispersion relation is highly nonlinear for a given wavenumber k, the growth rate θ might not be unique. In such case it is assumed that the growth rate is always given by the largest one. Considering an arbitrary perturbation, typically a solution with a length scale of the order of the wavenumber with the largest growth rate is selected. Numerical solutions of dispersion relation (4.21) obtained with MATLAB (The MathWorks Inc.) are shown in Fig. 4.7 for different parameter values. However, the dispersion relation still depends on V, which is arbitrary.

The dispersion relations shown in Fig. 4.7 reproduce the experimental evidences (Miura and Shiota, 2002; Hartmann and Miura, 2006) that a decrease in the growth factor diffusion leads to an increase in the most unstable wavenumber and in the corresponding growth rate. Additionally, the dispersion relation predicts that increasing κ the most unstable wavenumber decreases and so does its growth rate in accordance with the experiments. We therefore conclude that within the explanatory power of a linear stability analysis, Model 4.11, and accordingly Model 4.13, reproduce typical experimental findings in growing cell cultures. Qualitatively, our results agree well with the ones obtained previously for a much simpler Darcy-like model (Hartmann and Miura, 2007), which is based on the assumption that the the material speed is simply proportional to a pressure gradient.

Our results do not change qualitatively, if we consider a shell-like theory (see Remark 4.3) as a model for the surface mechanics of the cell culture. The term $(\kappa k)/(2\mu^\star)$ in the dispersion relation (4.21) is simply replaced by $(\kappa k^3)/(2\mu^\star)$, which does not affect the qualitative structure. If we would neglect completely surface mechanics, arbitrarily small wavelengths, corresponding to arbitrarily large wavenumbers k, would have the largest growth rates. The curves shown in Fig. 4.7 would not decay for $k \to \infty$.

In this section, we have investigated the linear stability of plane wave fronts of Model 4.11, and accordingly Model 4.13. The results indicate that the models are able to reproduce branching morphogenesis. Here, we have restricted ourselves to fast stress relaxation, linear kinetics, travelling waves, and short time scales. Therefore, our results can be only of a qualitative nature. The investigated model shows the same qualitative behaviour as a much simpler model proposed earlier (Hartmann and Miura, 2007). With respect to quantitative predictions more realistic models, as derived in Section 4.2, have to be considered. However, quantitative predictions can be achieved only by computational means due to the complexity of the models. A detailed computational investigation of theses models including viscoelasticity and a more complex chemical control is an open problem which definitely should be addressed in the future.

Our analysis has been restricted to the solely "viscous" Model 4.11, because only in this case travelling wave solutions could be constructed. But an instability with similar properties is expected also in the elastic case. Perturbing the front periodically, the chemical concentration would have the same form, since it is independent of the mechanical problem - mechanics determine only the evolution of the perturbation. Moreover, the isotropic growth γ (growth tensor $\boldsymbol{G} = \gamma \boldsymbol{I}$) would have the same form as the chemical concentration in a linear theory. Thus, in a linear theory the elasticity equations would have the same structure as the "viscous" model (interchanging material speed $\boldsymbol{v}$ and displacements $\boldsymbol{u}$). Therefore, the same instability would be observed, i.e. elasticity of the bulk medium would not stabilise the front within a linear theory as it might be expected. That is, membrane mechanics would still be needed to prevent instabilities with arbitrarily large wavenumbers, and accordingly arbitrarily small wavelength. However, a stabilisation via bulk mechanics might still occur in a nonlinear way.

4.4 Summary and discussion

This chapter has been devoted to the investigation of growing cell cultures as an example of the multiscale concept introduced in Chapter 2 where the interactions between biological processes and mechanics are important.

The main difficulty modelling mechanics of growing cell cultures is the characterisation of appropriate stress-strain relationships (constitutive equations). Growth induces deformations, i.e. an evolution of the underlying discrete network, which do not give rise to stresses. Hence, it is typically not clear which deformation measure should be used to determine the stress-strain relationships.

Assuming a solely elastic behaviour of the cell culture, we have shown in Section 4.2 how do derive appropriate macroscopic stress tensors from a discrete description. We have based our analysis on an oversimplified lattice-free cellular automaton model (similar to discrete models proposed by Palsson and Othmer, 2000, or Drasdo, 2005). The approach assumes that the mechanical properties of a cell are determined by the cytoskeleton, which is growing with cell size. Using the multiscale theory outlined in Chapter 2, the continuous limit functional has been rigorously and explicitly determined. In the case of isotropic growth, our approach coincides with the so-called notion of multiple natural configurations (Lubarda, 2004). It postulates a multiplicative decomposition of the deformation gradient into a deformation related to mechanics and one related to growth. However, in the case of anisotropic growth our approach postulates, in addition, that remodelling has to be considered. That is, an evolution of the underlying stress-strain relationships (constitutive equations) is already found in the oversimplified model proposed here. Approaches using multiple natural configurations directly often neglect remodelling.

One difficulty considering interactions between growth and mechanics is the identification of appropriate growth laws. The postulation of appropriate growth tensors on an experimental basis is so far "quite impossible" due to complexity of growth on the one hand and a limited explanatory power of typical experiments on the other hand. Only one invariant of the growth tensor can be related to the growth rate. Because of the limited biological knowledge, we have restricted ourselves in the rest of the chapter mainly to isotropic growth.

Our multiscale approach in Section 4.2 is based on the assumption that the cell culture is solely elastic, or rather viscoelastic, an assumption common in many works (e.g. Rodriguez et al., 1994; Ambrosi and Mollica, 2002; Ben Amar and Goriely, 2005). However, experimental findings suggest that a Maxwell viscoelastic description is more appropriate, since stress relaxation occurs on the time scale of growth (Forgacs et al., 1998). Therefore, in the case of growing cultures the multiscale analysis can yield only limited information on the structure of the stress tensor. However, using a formal approach we have further derived a viscoelastic description of growing cell cultures. A rigorous approach is an open problem.

Based on such a viscoelastic description, we have proposed a model for branching morphogenesis in the limit of fast relaxation of stresses. The model comprises explicitly the coupling of biological processes and mechanics: growth occurs due to a signal of growth factors, which are diffusing inside and outside the cell culture. Since simulations of the model are not straight forward, we have investigated the model via a linear

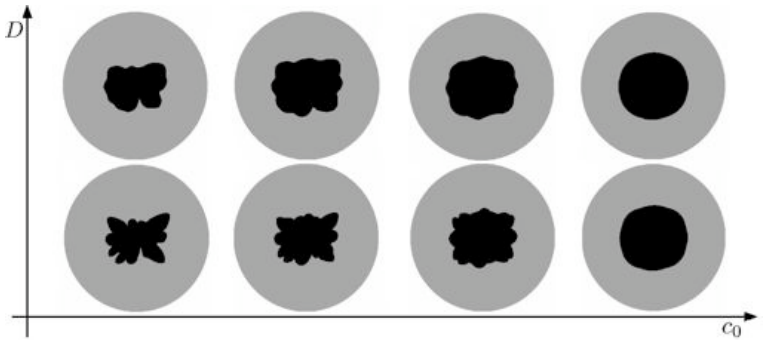

Fig. 4.8. Phase diagram of computed lung explant morphologies with different initial FGF concentrations c_0 and diffusion coefficients D based on a simplified Darcy-like model. The results agree qualitatively well with the experimental findings shown in Fig. 4.2. (reprinted from Hartmann and Miura, 2006, ©2007 Elsevier)

stability analysis in Section 4.3. The analysis clearly shows that the model exhibits a front instability leading to branch patterns. Qualitatively, it has the same properties as a much simpler model proposed earlier for branching morphogenesis (Hartmann and Miura, 2007, 2006). The simpler model is based on a Darcy-like assumption that the material speed is proportional to a pressure gradient, i.e. $\boldsymbol{v} = -\alpha \nabla p$. This allows to neglect the balance of momentum and simplifies the model drastically. The Darcy-like model reproduces the experimental findings for lung branching morphogenesis on a qualitative level quite well (Fig. 4.8). However, with respect to quantitative results a more realistic approach taking mechanics into account is necessary.

Ben Amar and Goriely (2005) have shown that growth can give rise to instabilities in elastic tissues within the theory of multiple natural configurations even without external load. The authors considered a spherical shell experiencing large anisotropic growth, which leads to a buckling instability. The instability observed in our system is of a different type, it is a diffusive instability as found e.g. in the Stefan problem (Visintin, 1996). By asymptotic analysis it has been shown formally that the Darcy-like model "converges" in the limit of small growth factor diffusion to the Stefan problem (Hartmann, 2007). The applied methods are quite general and a similar approach should be considered for the more complex model outlined in this chapter. Other open mathematical questions include a more rigorous approach with respect to the linear stability analysis, as well as addressing the issue of existence and uniqueness, which have not been touched at all.

The linear stability analysis presented in Section 4.3 is restricted to travelling waves and short time scales. Its quantitative predictive power might be questionable. Since similar models are well accessible by computational techniques (Ambrosi et al., 2007), it should be possible to perform a stability analysis by numerical means following the approach of Hartmann and Miura (2007). Thus a numerical stability analysis is the next logical step to be investigated in future.

The application of multiscale analysis to the growth of cell cultures underlines that the multiscale theory outlined in Chapter 2 is not restricted to constant networks, but can yield valuable information also in the case of evolving networks. We believe that similar approaches can be used to derive appropriate macroscopic models in many other applications considering interactions between biological processes and discrete mechanical elements on a microscopic scale.

Chapter 5

Outlook

In this thesis, we have shown that Γ-convergence, a mathematical concept in multiscale-analysis, is a powerful tool for rigorously deriving models in biomechanics and mechanobiology on the basis of a microscopic discrete description. Here, we have considered microscopic models defined in terms of energy functions on regular networks. As applications, we have investigated the mechanics of red blood cells (Chapter 3) and the interactions between mechanics and biological processes in growing cell cultures (Chapter 4).

Furthermore, we have developed a highly flexible simulation framework for single cell mechanics. The approach includes the coupling of mechanics on a hypersurface with bulk mechanics. It allows a realistic treatment of membrane mechanics as well as a broad class of constitutive relations (stress-strain relationships) for bulk mechanics. Simulations so far have been restricted to Stokes laws, or considered the membrane as a three-dimensional body rather than a two-dimensional hypersurface, which is a more appropriate description (Boal, 2002). The simulation framework can be easily extended to include biochemical processes inside the cell as well as on the membrane and makes it an ideal tool for studying the mechanobiology of single cells.

The results achieved in this thesis show the power of multiscale analysis with respect to the derivation of appropriate models. The considered models yield qualitative as well as quantitative predictions. Especially the latter require sophisticated numerical tools. The two test cases are well defined, but of a relatively "simple" structure. However, the same techniques could be applied to a wide class of other problems in mechanobiology.

On a microscopic level the characterisation of biochemical and biomechanical systems advances incredibly fast. Sometimes not only the biochemical processes or mechanical characteristics alone can be determined in detail, but also its interactions, e.g. in the case of moving epidermal fish keratocytes (Fig. 5.1). In the case of keratocytes a detailed microscopic picture of the underlying actin-myosin machinery and its biological control has been sketched (Verkhovsky et al., 1999; Oliver et al., 1999). On the other hand, many models describing movement of keratocytes do not benefit

(a) 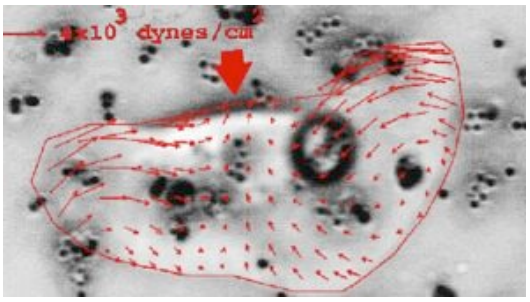

(b) 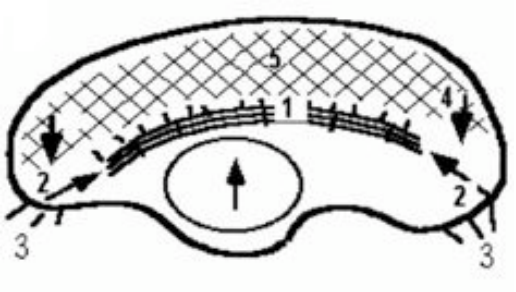

Fig. 5.1. (a) Fish epidermal keratocyte undergoing steady gliding in a straight line. Bold arrow indicates the direction of locomotion. (b) Modified network contraction model: Actomyosin contractility along a proposed equatorial sarcomere-like structure (1) generates pinching tractions (2) and breaks adhesive bonds beneath retraction fibres (3). Dynamic network contraction generates propulsive tractions in the "wings" of the cell (4), but is down-regulated at the front leading edge (5). (reprinted from Oliver et al., 1999, ©1999 Rockefeller University Press)

from the available experimental information (e.g. Rubinstein et al., 2005; Kruse et al., 2005, for an extensive list of models see `http://www.cellmigration.org`).

Similarly in many other cases, the available microscopic information and data is used only rarely to derive appropriate macroscopic models. The approaches outlined in this thesis will provide invaluable information on how to connect the increasing knowledge on a microscopic scale with macroscopic properties and behaviour. And thus they follow the dictum of Schnell, Grima, and Maini (2007):

> *Molecular biology took Humpty Dumpty apart; mathematical modeling is required to put him back together again.*

Appendices

Appendix A

Notation

For the sake of notational convenience, we will sometimes consider in the following scalars and vectors as matrices, i.e. $a = a_{11}$, respectively $(\boldsymbol{a})_i = a_{1i}$.

General scheme of notation

a	Scalars
$\boldsymbol{a}$	Vectors or matrices with components a_{ij}, i.e. $(\boldsymbol{a})_{ij} = a_{ij}$
$\boldsymbol{a} \cdot \boldsymbol{b}$	Standard matrix / vector multiplication, i.e. $(\boldsymbol{a} \cdot \boldsymbol{b})_{ik} = \sum_j a_{ij} b_{jk}$
$\boldsymbol{a} : \boldsymbol{b}$	Frobenius or componentwise inner product, i.e. $\boldsymbol{a} : \boldsymbol{b} = \sum_{ij} a_{ij} b_{ij}$
$\boldsymbol{a} \otimes \boldsymbol{b}$	Tensor product of two vectors, i.e. $(\boldsymbol{a} \otimes \boldsymbol{b})_{ij} = a_i b_j$
$\boldsymbol{a}^T$	Transpose of a matrix, i.e. $(\boldsymbol{a}^T)_{ij} = (\boldsymbol{a})_{ji}$

Global notation

Ω	Domain
$\Gamma = \partial\Omega$	Boundary of the domain Ω
$\boldsymbol{X}$	Lagrangian coordinates, i.e. coordinates with respect to the reference coordinate system
$\boldsymbol{x}$	Eulerian coordinates, i.e. coordinates with respect to the laboratory coordinate system
$\boldsymbol{\chi}$	Material deformation / motion, i.e. $\boldsymbol{x} = \boldsymbol{\chi}(\boldsymbol{X})$
$\boldsymbol{v}$	Material speeds
$\boldsymbol{u}$	Material displacements, i.e. $\boldsymbol{u} = \boldsymbol{\chi} - \boldsymbol{X}$
$\boldsymbol{F}$	Deformation gradient, i.e. $\boldsymbol{F} = \nabla_0 \boldsymbol{x}$ and accordingly $F_{ij} = \frac{\partial x_i}{\partial X_j}$
J	Jacobian of $\boldsymbol{F}$, i.e. $J = \det \boldsymbol{F}$
$\boldsymbol{L}$	Deformation rate tensor, i.e. $\boldsymbol{L} = \nabla \boldsymbol{v}$
$\boldsymbol{D}$	Symmetric deformation rate tensor, i.e. $\boldsymbol{D} = \frac{1}{2}(\boldsymbol{L} + \boldsymbol{L}^T)$

$\boldsymbol{F}^\Gamma$	Surface deformation gradient, defined as $\boldsymbol{F}^\Gamma = \boldsymbol{F} \cdot (\boldsymbol{I} - \boldsymbol{n}_0 \otimes \boldsymbol{n}_0)$ (By construction, we have $(\boldsymbol{I} - \boldsymbol{n} \otimes \boldsymbol{n}) \cdot \boldsymbol{F}^\Gamma = \boldsymbol{F}^\Gamma$.)
J^Γ	Surface Jacobian (Attention, $J^\Gamma \neq \det \boldsymbol{F}^\Gamma = 0$)
$\boldsymbol{\sigma}$	True volume stress tensor (or Cauchy stress tensor), defined such that the force/traction per unit area acting on a plane with normal $\boldsymbol{n}$ is given by $\boldsymbol{\sigma} \cdot \boldsymbol{n}$
$\boldsymbol{\tau}$	True surface stress tensor (or Cauchy stress tensor), defined such that the in-plane traction exerted on a cross section of the membrane that is normal to the tangential unit vector $\boldsymbol{b}$ is given by $\boldsymbol{\tau} \cdot \boldsymbol{b}$
$\boldsymbol{n}$	Outer unit normal
$\boldsymbol{P}$	Surface projection operator, i.e. $\boldsymbol{P} = \boldsymbol{I} - \boldsymbol{n} \otimes \boldsymbol{n}$
C_1, C_2	Principal curvatures
H	Mean curvature, i.e. $H = C_1 + C_2$
H_0	Reference mean curvature
K	Gaussian curvature, i.e. $K = C_1 C_2$
$\boldsymbol{Y}$	Mean curvature vector, defined as $\boldsymbol{Y} = H\boldsymbol{n}$

Differential and integral operators

$\int \ldots d\mu$	Volume or surface integral
$\frac{d}{dt}$	Total derivative w.r.t. t, which agrees with the material derivative in all the cases considered in this thesis, i.e. $\frac{d}{dt} = \frac{\partial}{\partial t} + \boldsymbol{v} \cdot \nabla$
$\frac{\partial}{\partial t}$	Partial derivative w.r.t. t
$\nabla \boldsymbol{a}$	Gradient, i.e. $(\nabla \boldsymbol{a})_{ijk} = \frac{\partial a_{ij}}{\partial x_k}$
$\nabla \cdot \boldsymbol{a}$	Divergence operator, i.e. $(\nabla \cdot \boldsymbol{a})_i = \sum_j \frac{\partial a_{ij}}{\partial x_j}$
$\Delta \boldsymbol{a}$	Laplace operator, i.e. $\Delta \boldsymbol{a} = \nabla \cdot (\nabla \boldsymbol{a})$ and accordingly $(\Delta \boldsymbol{a})_{ij} = \sum_k \frac{\partial^2 a_{ij}}{\partial x_k^2}$
$\nabla^\Gamma \boldsymbol{a}$	Tangential gradient, i.e. $\nabla^\Gamma \boldsymbol{a} = (\boldsymbol{P} \cdot \nabla)\boldsymbol{a} = (\nabla \boldsymbol{a}) \cdot \boldsymbol{P}$ and accordingly $(\nabla^\Gamma \boldsymbol{a})_{ijk} = \sum_l P_{kl} \frac{\partial a_{ij}}{\partial x_l}$
$\nabla^\Gamma \cdot \boldsymbol{a}$	Surface divergence operator, i.e. $(\nabla^\Gamma \cdot \boldsymbol{a})_i = \sum_{jk} P_{jk} \frac{\partial a_{ij}}{\partial x_k}$
$\Delta^\Gamma \boldsymbol{a}$	Laplace-Beltrami operator, i.e. $\Delta^\Gamma \boldsymbol{a} = \nabla^\Gamma \cdot (\nabla^\Gamma \boldsymbol{a})$ and accordingly $(\Delta^\Gamma \boldsymbol{a})_{ij} = \sum_{klm} P_{mk} \frac{\partial}{\partial x_k} (P_{ml} \frac{\partial a_{ij}}{\partial x_l})$

Quantities with respect to the reference or initial configuration, i.e. considering the Lagrangian coordinate system, are marked by the subscript 0, e.g.

$\boldsymbol{n}_0$	Normal with respect to the initial configuration
∇_0,	Differential operator with respect to the Lagrangian coordinates
$\int \ldots d\mu_0$	Integral operator with respect to the Lagrangian coordinates

Appendix B

Some geometric analysis

For the convenience of the reader, let us repeat the definitions and results from differential geometry used in this thesis. For more details especially with respect to numerical implementations, we refer to the review Deckelnick et al. (2005).

For each $t \in [0,T]$, $T > 0$, let $\Gamma(t)$ be a compact, closed, and orientable hypersurface in $\mathbb{R}^n$, which is twice differentiable. Since Γ is orientable, a vector field $\boldsymbol{n} \in C^1(\Gamma;\mathbb{R}^n)$ normal to Γ exists by definition. In the following, we consider only outer unit normals $\boldsymbol{n}$.

Parametric representation

Typically, we consider *parametric representations*: For each point $x \in \Gamma$ there exist an open set $U \subset \mathbb{R}^n$ containing x, an open set $V \subset \mathbb{R}^{n-1}$, and a map $\boldsymbol{\chi} \in C^2(V,\mathbb{R}^n)$ such that $U \bigcap \Gamma = \boldsymbol{\chi}(V)$ and $\operatorname{rank} D\boldsymbol{\chi}(\boldsymbol{\theta}) = n-1$ for all $\boldsymbol{\theta} \in V$. A basis of the tangent space at $\boldsymbol{x} = \boldsymbol{\chi}(\boldsymbol{\theta})$ is then given by the vectors $\frac{\partial \boldsymbol{\chi}(\boldsymbol{\theta})}{\partial \theta_1}, \dots, \frac{\partial \boldsymbol{\chi}(\boldsymbol{\theta})}{\partial \theta_{n-1}}$.

Let us define the *metric / metric tensor* on Γ:

$$g_{ij}(\boldsymbol{\theta}) = \frac{\partial \boldsymbol{\chi}(\boldsymbol{\theta})}{\partial \theta_i} \cdot \frac{\partial \boldsymbol{\chi}(\boldsymbol{\theta})}{\partial \theta_j}, \quad i,j = 1,\dots,n-1.$$

Furthermore, let $g = \det(g_{ij})$ and g^{ij} be the components of the inverse of the matrix (g_{ij}). Then the tangential gradient and the Laplace-Beltrami operator of a function f (defined in a neighbourhood of Γ) are given by:

$$\nabla^\Gamma f = \sum_{i,j=1}^{n-1} g^{ij} \frac{\partial f}{\partial \theta_j} \frac{\partial \boldsymbol{\chi}}{\partial \theta_i},$$

$$\Delta^\Gamma f = \frac{1}{\sqrt{g}} \sum_{i,j=1}^{n-1} \frac{\partial}{\partial \theta_i} \left(\sqrt{g} g^{ij} \frac{\partial f}{\partial \theta_j} \right).$$

These characterisations are equivalent to the ones given in Appendix A via the projection operator $\boldsymbol{P}$, but are more suitable with respect to a numerical implementation.

Shape operator, mean curvature, and Gauss curvature

Let us introduce the *shape operator*:

$$\boldsymbol{H} = \nabla^\Gamma \boldsymbol{n} = (\nabla \boldsymbol{n}) \cdot \boldsymbol{P},$$

where $\boldsymbol{P} = \boldsymbol{I} - \boldsymbol{n} \otimes \boldsymbol{n}$ is the tangential projection operator.

The shape operator $\boldsymbol{H}$ is a symmetric matrix and hence can be diagonalised. It has one eigenvalue equal to zero with corresponding eigenvector $\boldsymbol{n}$. The remaining $n-1$ eigenvalues $C_1, \ldots, C_{n-1}$ are called the *principal curvatures* of Γ. The *mean curvature* is defined as

$$H = \sum_{j=1}^{n-1} C_j = \sum_{j=1}^{n} H_{jj} = \nabla^\Gamma \cdot \boldsymbol{n}.$$

Our definition implies in particular that $H > 0$ if $\Gamma = S^n$. Here, we use the definition of Deckelnick et al. (2005), which differs from the probably more common definition $H = \frac{1}{n-1} \sum_{j=1}^{n-1} C_j$.

Other important quantities used in differential geometry are the so-called *Gauss curvature* K, defined as

$$K = \prod_{j=1}^{n-1} C_j$$

and the mean curvature vector

$$\boldsymbol{Y} \equiv H\boldsymbol{n} = -\Delta^\Gamma \boldsymbol{x},$$

which allows a straight forward weak formulation.

Integration by parts

The following formula of *integration by parts* is true for any function f, which is continuously differentiable in a neighbourhood of closed surfaces Γ:

$$\int_\Gamma \nabla^\Gamma f d\mu = \int_\Gamma f H \boldsymbol{n} d\mu.$$

Using the product rule, we obtain Green's formula:

$$\int_\Gamma \nabla^\Gamma f \cdot \nabla^\Gamma g d\mu = -\int_\Gamma f \Delta^\Gamma g d\mu, \tag{B.1}$$

where f and g are sufficiently smooth functions. In particular (B.1) implies the weak characterisation of the mean curvature

$$\int_\Gamma H\nu \cdot \boldsymbol{\phi} d\mu = \int_\Gamma \nabla^\Gamma \boldsymbol{x} \cdot \nabla^\Gamma \boldsymbol{\phi} d\mu,$$

where ϕ is an appropriate test function.

Appendix C

Some polymer physics

Considering mechanics of polymer networks, different concepts than the usual elasticity theory are needed. For example, polymers can usually not be considered as "simple" elastic rods. The size of single polymers is rather small and therefore thermodynamical effects play an important role. By the system's statistical tendency to increase its entropy, thermodynamic effects lead to an apparent elasticity, also referred to as entropic elasticity.

Here, we consider the so-called freely jointed chain, which is a very rough model of a single polymer. It shows elegantly how entropic effects could lead to an elastic behaviour. For more details we would like to refer e.g. to the books of Grosberg and Khokhlov (1997) or Boal (2002).

The freely jointed chain

Let us consider an oversimplified polymer (see Fig. C.1): the freely jointed chain. It consists of N units $\boldsymbol{r}_i$ with a fixed length $l = |\boldsymbol{r}_i|$. The directions of the vectors $\boldsymbol{r}_i$ shall be random and independent of each other. Hence, the end-to-end vector of such

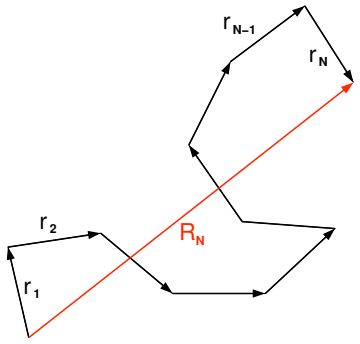

Fig. C.1. Illustration of a freely jointed chain - an oversimplified polymer.

a polymer is given by

$$\boldsymbol{R}_N = \sum_{i=1}^{N} \boldsymbol{r}_i.$$

Using the recursive relation $\boldsymbol{R}_N = \boldsymbol{R}_{N-1} + \boldsymbol{r}_N$, we can rewrite the average length of the end-to-end vector to the power 2 as

$$\begin{aligned}\left\langle \boldsymbol{R}_N^2 \right\rangle &= \left\langle \boldsymbol{R}_{N-1}^2 + 2\boldsymbol{R}_{N-1}\boldsymbol{r}_N + \boldsymbol{r}_N^2 \right\rangle \\ &= \left\langle \boldsymbol{R}_{N-1}^2 + 2|\boldsymbol{R}_{N-1}| l\cos\gamma_N + l^2 \right\rangle \\ &= \left\langle \boldsymbol{R}_{N-1}^2 \right\rangle + l^2,\end{aligned}$$

where we have used that the angle γ_N between $\boldsymbol{R}_{N-1}$ and $\boldsymbol{r}_N$ is random, i.e. $\langle \cos\gamma_N \rangle = 0$. By induction, we recover

$$\langle |\boldsymbol{R}_N| \rangle = \sqrt{Nl^2} = \sqrt{L_N}\sqrt{l}. \tag{C.1}$$

Hence, the end-to-end distance of a polymer consisting of N subunits is much smaller than the contour length $L_N = Nl$. This is the so-called "$L^{1/2}$ rule".

Relation (C.1) yields some information on the average length of the idealised polymer. It is also possible to calculate the probability distribution $\mathcal{P}_N(\boldsymbol{R})$ of end-to-end vectors (Boal, 2002). For a large number of subunits this probability distribution converges to a Gaussian distribution, i.e it holds

$$\mathcal{P}(\boldsymbol{R}) = \lim_{N\to\infty} \mathcal{P}_N(\boldsymbol{R}) = \left[\frac{3}{2\pi N l^2}\right]^{3/2} \exp\left(-\frac{3\boldsymbol{R}^2}{2Nl^2}\right). \tag{C.2}$$

Entropic elasticity

In analogy to an ideal gas (Meschede and Gerthsen, 2006), a free energy can be assigned to an ensemble of polymers. Considering freely jointed chains the free energy reads

$$F = -TS,$$

with temperature T and entropy S. Here, the internal energy of the polymer has been neglected as it is a constant independent of the end-to-end distance $\boldsymbol{R}$. (The subsegments are allowed to rotate freely and are not elastic.)

The entropy S can be calculated using the Boltzmann principle. Suppose there are Z ways in which molecules can occupy a certain state, then the entropy is given by

$$S = k_B \ln Z,$$

where k_B is the Boltzmann constant. Obviously, the number of ways Z in which the ensemble can attain an end-to-end distance $\boldsymbol{R}$ is proportional to the probability distribution $\mathcal{P}(\boldsymbol{R})$ given by (C.2). We therefore get (Grosberg and Khokhlov, 1997)

$$F(\boldsymbol{R}) \sim k_B T \left(\frac{3\boldsymbol{R}^2}{2Nl^2}\right). \tag{C.3}$$

Using the relation $\boldsymbol{f}(\boldsymbol{R}) = -\frac{\partial F(\boldsymbol{R})}{\boldsymbol{R}}$ between forces $\boldsymbol{f}$ and energies F, we conclude

$$\boldsymbol{f} \sim -\left(\frac{3k_BT}{Nl^2}\right)\boldsymbol{R}.$$

The force $\boldsymbol{f}$ is proportional to the "deformation" $\boldsymbol{R}$. That is, the freely jointed chain obeys Hooke's law, which has been originally introduced as a description of springs. Of course there are some fundamental differences. In contrast to springs, the force constant depends on the temperature T. Further, the average value of $\boldsymbol{R}$ for an undeformed polymer is zero and we cannot work with relative deformations $\Delta l/l$, usually used in the definition of Hooke's law.

The example of the freely jointed chain shows a fundamental concept of polymer mechanics: Often the apparent elasticity is due to thermodynamic effects and not due to elastic properties of the polymers themselves. For more details on polymer mechanics, we would like to refer to the books by Grosberg and Khokhlov (1997) or Boal (2002). More information on the concept of free energies, entropy, or the Boltzmann principle can be found e.g. in the book by Meschede and Gerthsen (2006).

Appendix D

Bibliography

Alicandro, R. and M. Cicalese (2004). A general integral representation result for continuum limits of discrete energies with superlinear growth. *SIAM J. Appl. Math. 36*, 1–37.

Alt, H. W. (2002a). *Lineare Funktionalanalysis* (4th ed.). Berlin-Heidelberg-New York: Springer-Verlag.

Alt, W. (2002b). Nonlinear hyperbolic systems of generalized Navier-Stokes type for interactive motion in biology. In S. Hildebrand and H. Karcher (Eds.), *Geometric Analysis and Nonlinear Partial Differential Equations*, pp. 431–461. Berlin-Heidelberg-New York: Springer-Verlag.

Ambrosi, D. and F. Guana (2005). Stress modulated growth. *Math. Mech. Solids, in press.*

Ambrosi, D., A. Guillou, and E. Di Martino (2007). Stress-modulated remodelling of a non-homogeneous body. *Biomech. Model. Mechan., in press.*

Ambrosi, D. and F. Mollica (2002). On the mechanics of a growing tumor. *Int. J. Eng. Sci. 40*, 1297–1316.

Ambrosi, D. and F. Mollica (2004). The role of stress in the growth of a multicell spheroid. *J. Math. Biol. 48*, 477–499.

Bänsch, E., P. Morin, and R. H. Nochetto (2005). A finite element method for surface diffusion: the parametric case. *J. Comput. Phys. 203*, 321–343.

Bao, G. and S. Suresh (2003). Cell and molecular mechanics of biological materials. *Nat. Mater. 2*, 715–725.

Barthés-Biesel, D. and J. M. Rallison (1981). The time-dependent deformation of a capsule freely suspended in a linear shear flow. *J. Fluid Mech. 113*, 251–267.

Becker, R., M. Braack, T. Dunne, D. Meidner, T. Richter, M. Schmich, T. Stricker, and B. Vexler (2007). GASCOIGNE 3D - a finite element toolbox (`http://www.gascoigne.uni-hd.de`).

Becker, R., T. Dunne, and D. Meidner (2007). VISUSIMPLE (`http://www.visusimple.uni-hd.de`).

Becker, R., D. Meidner, and B. Vexler (2007). RODOBO (`http://www.rodobo.uni-hd.de`).

Beil, M., S. Eckel, F. Fleischer, H. Schmidt, V. Schmidt, and P. Walther (2006). Fitting of random tessellation models to keratin filament networks. *J. Theor. Biol. 241*, 62–72.

Beil, M., A. Micoulet, G. von Wichert, S. Paschke, P. Walther, M. B. Omary, P. P. Van Veldhoven, U. Gern, E. Wolff-Hieber, J. Eggermann, J. Waltenberger, G. Adler, J. Spatz, and T. Seufferlein (2003). Sphingosylphosphorylcholine regulates keratin network architecture and visco-elastic properties of human cancer cells. *Nat. Cell Biol. 5*, 803–811.

Ben Amar, M. and A. Goriely (2005). Growth and instability in elastic tissues. *J. Mech. Phys. Solids 53*, 2284–2319.

Berezhnyy, M. and L. Berlyand (2006). Continuum limit for three-dimensional mass-spring networks and discrete Korn's inequality. *J. Mech. Phys. Solids 54*, 635–669.

Blatz, P. J. and W. L. Ko (1962). Application of finite elasticity theory to the deformation of rubbery materials. *T. Soc. Rheol. 6*, 233–251.

Boal, D. (2002). *Mechanics of the Cell*. Cambridge: Cambridge University Press.

Boey, S. K., D. H. Boal, and D. E. Discher (1998). Simulations of the erythrocyte cytoskeleton at large deformation. I. Microscopic models. *Biophys. J. 75*, 1573–1583.

Braides, A. (2001). From discrete to continuous variational problems: An introduction. Lecture notes, School on Homogenization Techniques and Asymptotic Methods for Problmes with Multiple Scales (`http://axp.mat.uniroma2.it/~braides/pdf/Torino.pdf`).

Braides, A. (2002). Γ-*convergence for Beginners*. Oxford: Oxford University Press.

Braides, A. and Defranceschi (1998). *Homogenization of Multiple Integrals*. Oxford: Oxford University Press.

Braides, A. and A. Piatnitsky (2004). Overall properties of a discrete membrane with randomly distributed defects. Preprint, Scuola Normale Superiore, Pisa.

Byrne, H. M. (1999). A weakly nonlinear analysis of a model of avascular solid tumour growth. *J. Math. Biol. 39*, 59–89.

Canham, P. (1970). The minimum energy of bending as a possible explanation of the biconcave shape of the human red blood cell. *J. Theor. Biol. 26*, 61–81.

Chaplain, M. A. J., S. Giles, B. D. Sleeman, and R. J. Jarvis (1995). A mathematical analysis of a model for tumour angiogenesis. *J. Math. Biol. 33*, 744–770.

Clarenz, U., U. Diewald, G. Dziuk, M. Rumpf, and R. Rusu (2004). A finite element method for surface restoration with smooth boundary conditions. *Comput. Aided Geom. Design 21*, 427–445.

Cogan, N. G. and J. P. Keener (2004). The role of the biofilm matrix in structural development. *Math. Med. Biol. 21*, 147–166.

Cowin, S. C. (2004). Tissue growth and remodeling. *Annu. Rev. Biomed. Eng. 6*, 77–107.

Dacorogna, B. (1989). *Direct Methods in the Calculus of Variations*. Berlin-Heidelberg-New York: Springer-Verlag.

Dal Maso, G. (1993). *An Introduction to* Γ*-convergence*. Boston: Birkhäuser.

Dao, M., J. Li, and S. Suresh (2006). Molecularly based analysis of deformation of spectrin network and human erythrocyte. *Mat. Sci. Eng. C 26*, 1232–1244.

Dao, M., C. Lim, and S. Suresh (2003). Mechanics of the human red blood cell deformed by optical tweezers. *J. Mech. Phys. Solids 51*, 2259–2280. Erratum, 53:493-494.

D'Arcy Thompson (1917). *On Growth and Form (Abr. ed. by J. T. Bonner, 1961)*. Cambridge: Cambridge University Press.

Deckelnick, K., G. Dziuk, and C. M. Elliott (2005). Computation of geometric partial differential equations and mean curvature flow. *Acta Numer. 14*, 139–232.

Di Carlo, A. and S. Quiligotti (2002). Growth and balance. *Mech. Res. Comm. 29*, 449–456.

Discher, D. E., D. H. Boal, and S. K. Boey (1997). Phase transitions and anisotropic responses of planar triangular nets under large deformation. *Phys. Rev. E 55*, 4762–4772.

Discher, D. E., D. H. Boal, and S. K. Boey (1998). Simulations of the erythrocyte cytoskeleton at large deformation. II. Micropipette aspiration. *Biophys. J. 75*, 1584–1597.

Dockery, J. and I. Klapper (2001). Finger formation in biofilm layers. *SIAM J. Appl. Math. 62*, 853–869.

Drasdo, D. (2005). Coarse graining in simulated cell populations. *Adv. Complex Syst. 2-3*, 319–363.

Drasdo, D. and S. Höhme (2005). A single-cell based model to tumor growth *in-vitro*: Monolayers and spheroids. *Phys. Biol. 2*, 133–147.

Drury, J. L. and M. Dembo (1999). Hydrodynamics of micropipette aspiration. *Biophys. J. 76*, 110–128.

Drury, J. L. and M. Dembo (2001). Aspiration of human neutrophils: Effects of shear thinning and cortical dissipation. *Biophys. J. 81*, 3166–3177.

Dziuk, G. (1991). An algorithm for evolutionary surfaces. *Numer. Math. 58*, 603–611.

Evans, E. A. and R. Skalak (1980). *Mechanics and Thermal Dynamics of Biomembranes*. Boca Raton: CRC Press.

Evans, L. C. (1998). *Partial Differential Equations*. Providence: American Mathematical Society.

Findley, W. N. (1976). *Creep and Relaxation of Nonlinear Viscoelastic Materials*. Amsterdam: North-Holland.

Forgacs, G., R. A. Foty, Y. Shafrir, and M. S. Steinberg (1998). Viscoelastic properties of living embryonic tissues: a quantitative study. *Biophys. J. 74*, 2227–2234.

Friedmann, A. (2004). A hierarchy of cancer models and their mathematical challenges. *Discrete Cont. Dyn. S. - B 4*, 147–159.

Friesecke, G. and F. Theil (2002). Validity and failure of the Cauchy-Born hypothesis in a two-dimensional mass-spring lattice. *J. Nonlinear Sci. 12*, 445–478.

Fung, Y. C. (1980). *Biomechanis: Mechanical Properties of Living Tissues* (2nd ed.). Berlin-Heidelberg-New York: Springer-Verlag.

Gov, N. S. and S. A. Safran (2005). Red blood cell membrane fluctuations and shape controlled by ATP-induced cytoskeletal defects. *Biophys. J. 88*, 1859–1874.

Greenspan, H. P. (1976). On the growth and stability of cell cultures and solid tumors. *J. Theor. Biol. 56*, 229–242.

Grosberg, A. Y. and A. R. Khokhlov (1997). *Giant Molecules: Here, there, and everywhere*. San Diego: Academic Press.

Hansen, J. C., R. Skalak, S. Chien, and A. Hoger (1997). Influence of network topology on the elasticity of the red blood cell membrane skeleton. *Biophys. J. 72*, 2369–2381.

Hartmann (2007). Limit behaviour of spatially growing cell cultures. *J. Theor. Biol. 244*, 409–415.

Hartmann, D. and T. Miura (2006). Modelling *in vitro* lung branching morphogenesis during development. *J. Theor. Biol. 242*, 862–872.

Hartmann, D. and T. Miura (2007). Mathematical analysis of a free boundary model for lung branching morphogenesis. *Math. Med. Biol., 24*, 209–224.

Heinze, S. (1987). Traveling waves in combustion processes with complex chemical networks. *Trans. Amer. Math. Soc. 304*, 405–416.

Helfrich, W. (1973). Elastic properties of lipid bilayers: Theory and possible experiments. *Z. Naturforsch. C 28*, 693–703.

Hénon, S., G. Lenormand, A. Richert, and F. Gallet (1999). A new determination of the shear modulus of the human erythrocyte membrane using optical tweezers. *Biophys. J. 76*, 1145–1151.

Humphrey, J. D. and Rajagopal (2002). A constrained mixture model for growth and remodeling of soft tissues. *Math. Models Methods Appl. Sci. 12*, 407–430.

Ingber, D. E. (2003). Tensegrity I. Cell structure and hierarchical systems biology. *J. Cell Sci. 116*, 1157–1173.

Kruse, K., J. F. Joanny, F. Jülicher, J. Prost, and K. Sekimoto (2005). Generic theory of active polar gels: A paradigm for cytoskeletal dynamics. *Eur. Phys. J. E 16*, 5–16.

Kuzman, D., S. Svetina, R. E. Waugh, and B. Zeks (2004). Elastic properties of the red blood cell membrane that determine echinocyte deformability. *Eur. Biophys. J. 33*, 1–15.

Landau, L. D. and E. M. Lifschitz (1991). *Elastizitätstheorie* (7th ed.), Volume 7 of *Lehrbuch der theoretischen Physik*. Frankfurt: Verlag Harri Deutsch.

Lenormand, G., S. Hénon, A. Richert, J. Simeon, and F. Gallet (2001). Direct measurement of the area expansion and shear moduli of the human red blood cell membrane skeleton. *Biophys. J. 81*, 43–56.

Li, J., M. Dao, C. T. Lim, and S. Suresh (2005). Spectrin-level modeling of the cytoskeleton and optical tweezer stretching of the erythrocyte. *Biophys. J. 88*, 3707–3719.

Libai, A. and J. G. Simmonds (1996). *The Nonlinear Theory of Elastic Shells* (2nd ed.). Cambridge: Cambridge University Press.

Lim, G. H. W., M. Wortis, and R. Mukhopadhyay (2002). Stomatocyte discocyte echinocyte sequence of the human red blood cell: Evidence for the bilayer couple hypothesis from membrane mechanics. *P. Natl. Acad. Sci. USA 99*, 16766–16769.

Liu, S., L. H. Derick, and J. Palek (1987). Visualization of the hexagonal lattice in the erythrocyte membrane skeleton. *J. Cell Biol. 104*, 527–536.

Lubarda, V. A. (2004). Constitutive theories based on the multiplicative decomposition of deformation gradient: Thermoelasticity, elastoplasticity, and biomechanics. *Appl. Mech. Rev. 57*, 95–108.

Marko, J. and E. D. Siggia (1995). Stretching DNA. *Macromolecules 28*, 8759–8770.

McDonald, P. H. (1996). *Continuum Mechanics*. Boston: PWS Publishing Company.

Meschede, D. and C. Gerthsen (2006). *Gerthsen Physik* (23rd ed.). Berlin-Heidelberg-New York: Springer-Verlag.

Mills, J. P., L. Qie, M. Dao, C. T. Lim, and S. Suresh (2004). Nonlinear elastic and viscoelastic deformation of the human red blood cell with optical tweezers. *Mech. Chem. Biosys 1*, 169–180.

Miura, T. and K. Shiota (2002). Depletion of FGF acts as a lateral inhibitory factor in lung branching morphogenesis *in vitro*. *Mech. Develop. 116*, 29–38.

Mohandas, N. and E. Evans (1994). Mechanical properties of the red cell membrane in relation to molecular structure and genetic defects. *Annu. Rev. Bioph. Biom. 23*, 787–818.

Mukhopadhyay, R., G. H. W. Lim, and M. Wortis (2002). Echinocyte shapes: Bending, stretching, and shear determine spicule shape and spacing. *Biophys. J. 82*, 1756–1772.

Neuman, K. C. and S. M. Block (2004). Optical trapping. *Rev. Sci. Instrum. 75*, 2787–2809.

Noguchi, H. and G. Gompper (2005). Shape transitions of fluid vesicles and red blood cells in capillary flows. *P. Natl. Acad. Sci. USA 102*, 14159–14164.

Oliver, T., M. Dembo, and K. Jacobsen (1999). Separation of propulsive and adhesive traction stresses in locomoting keratocytes. *J. Cell Biol. 145*, 589–604.

Palsson, E. and H. Othmer (2000). A model for individual and collective cell movement in dictyostelium discoideum. *P. Natl. Acad. Sci. USA 12*, 10448–10453.

Pozrikidis, C. (2001). Effect of membrane bending stiffness on the deformation of capsule in simple shear flow. *J. Fluid Mech. 440*, 269–291.

Pozrikidis, C. (2003a). *Modeling and Simulation of Capsules and Biological Cells*. Boca Raton: CRC Press.

Pozrikidis, C. (2003b). Numerical simulation of the flow-induced deformation of red blood cells. *Ann. Biomed. Eng. 31*, 1194–1205.

Pozrikidis, C. (2003c). Shell theory for capsules and cells. In C. Pozrikidis (Ed.), *Modeling and Simulation of Capsules and Biological Cells*, pp. 35–102. Boca Raton: CRC Press.

Pozrikidis, C. (2005). Numerical simulation of cell motion in tube flow. *Ann. Biomed. Eng. 33*, 165–178.

Rodriguez, E. K., A. Hoger, and A. D. McCulloch (1994). Stress-dependent finite growth in soft elastic tissues. *J. Biomech. 27*, 455–467.

Romer, A. and T. Parsons (1986). *The Vertebrate Body* (6th ed.). Philadelphia: W. B. Saunders.

Rubinstein, B., K. Jacobson, and A. Mogilner (2005). Multiscale two-dimensional modeling of a motile simple-shaped cell. *Multiscale Model. Sim. 3*, 413–439.

Rusu, R. E. (2005). An algorithm for the elastic flow of surfaces. *Interface. Free Bound. 7*, 229–239.

Scheffer, L., A. Bitler, E. Ben-Jacob, and R. Korenstein (2001). Atomic force pulling: Probing the local elasticity of the cell membrane. *Eur. Biophys. J. 30*, 83–90.

Schmidt, B. (2005). On the passage from atomic to continuum theory for thin films. Preprint 82, Max-Planck-Institut für Mathematik in den Naturwissenschaften, Leipzig.

Schnell, S., R. Grima, and P. K. Maini (2007). Multiscale modeling in biology. *Am. Sci. 95*, 134–142.

Seifert, U., K. Berndl, and R. Lipowsky (1991). Shape transformations of vesicles: Phase diagram for spontaneous-curvature and bilayer-coupling models. *Phys. Rev. A 44*, 1182 – 1202.

Skalak, R., A. Tözeren, P. R. Zarda, and S. Chien (1973). Strain energy function of red blood cell membranes. *Biophys. J. 13*, 245–264.

Trusdell, C. A. (1983). The influence of elasticity on analysis: The classical heritage. *Bull. Amer. Math. Soc. 9*, 293–310.

Verkhovsky, A. B., T. M. Svitkina, and G. G. Borisy (1999). Network contraction model for cell translocation and retrograde flow. *Biochem. Soc. Symp. 65*, 207–222.

Visintin, A. (1996). *Models of Phase Transitions*. Boston: Birkhäuser.

Wang, J.-C. and B. P. Thampatty (2006). An introductory review of cell mechanobiology. *Biomech. Model. Mechan. 5*, 1–16.

Willmore, T. J. (1993). *Riemannian Geometry*. Oxford: Clarendon Press.

Acknowledgements

First of all, I would like to express my gratitude to Prof. Willi Jäger for offering me the possibility to work on such a highly interesting research topic, as well as for his constant exemplary effort of allowing me a balance between work and family. Furthermore, I would like to thank Prof. Marek Niezgódka for always finding some time when I was in Warsaw and for pushing me to be sometimes more specific. Without the financial support of the German Research Foundation (DFG) through the International Graduiertenkolleg 710 "Complex processes: Modeling, Simulation and Optimization" this thesis would not have been possible.

Moreover, I especially thank Prof. Andrey Piatnitski and Mariya for very stimulating discussions on the mathematical part of this thesis; Dominik, Thomas, and Tom for the outstanding Gascoigne support; Christian E., Christian R., Franzi, Igor, and Mariya for proofreading; Anna M. for being my outpost in the institute; and Anna T. for her endless efforts to improve the Heidelberg-Warsaw cooperation significantly.

And last but not least, I would like to thank Frauke, Clara, and Leander for their love and constant moral support. Without them, I would probably have abandoned my idealism and be a well paid capitalist by now.